Highly-Charged Ion Collisions with Atoms: Applications to X-ray Emission in the Universe

by

Renata S Cumbee

(Under the Direction of Phillip C Stancil)

Abstract

Atomic collisions play a fundamental role in astrophysics, plasma physics, and fusion physics. In this dissertation, we focus on charge exchange (CX) between hot ions and neutral atoms relevant to a selection of astronomical environments. Even though charge exchange calculations can provide vital information including neutral and ion density distributions, ion temperatures, elemental abundances, and ion charge state distributions in the environments considered, both theoretical calculations and laboratory studies of these processes lack the necessary reliability and/or coverage. In order to better understand the spectra we observe in astrophysical environments in which both hot plasma and neutral gas are present, including comets, the heliosphere, supernova remnants, galaxy clusters, star forming galaxies, the outflows of starburst galaxies, and cooling flows of hot gas in the intracluster medium, a thorough CX X-ray model is needed. Included in this model should be a complete set of X-ray line ratios for relevant ion and neutral interactions for a range of energies.

In this work, theoretical charge exchange emission spectra are produced using cross sections calculated with widely applied approaches including the quantum mechanical molecular orbital close coupling (QMOCC), atomic orbital close coupling (AOCC), classical trajectory

Monte Carlo (CTMC), and the multichannel Landau-Zener (MCLZ) methods. When possible, theoretical data are benchmarked to experiments. Using a comprehensive, but still far from complete, CX database, new models are performed for a variety of X-ray emitting environments. In an attempt to describe the excess emission in X-rays of the starburst galaxy M82, Ne X CX line ratios are compared to line ratios observed in the region. A more complete XSPEC X-ray emission model is produced for H-like and He-like C-Al ions colliding with H and He for a range of energies; 200, 300, 500, 700, 1000, 2000, 3000, and 5000 eV/u. This model is applied to the northeast rim of the Cygnus Loop supernova remnant in an attempt to determine the contribution of CX to that region. The database is also applied to a preliminary model of the fast and slow solar wind interacting with the heliosphere.

INDEX WORDS: atomic processes, galaxies: individual: M82, galaxies: starbursts, ISM: supernova remnants, line: formation, X-rays: general, X-rays: ISM, X-rays: galaxies

Highly-Charged Ion Collisions with Atoms: Applications to X-ray Emission in the Universe

by

Renata Sade Cumbee

B.S., Francis Marion University, 2010

A Dissertation Submitted to the Graduate Faculty
of The University of Georgia in Partial Fulfillment
of the
Requirements for the Degree

Doctor of Philosophy

Athens, Georgia

2016

©2016

Renata Sade Cumbee

All Rights Reserved

Highly-Charged Ion Collisions with Atoms: Applications to X-ray Emission in the Universe

by

Renata Sade Cumbee

Approved:

Major Professor: Phillip C Stancil

Committee: Inseok Song
Robin Shelton

Electronic Version Approved:

Suzanne Barbour
Dean of the Graduate School
The University of Georgia
August 2016

Highly-Charged Ion Collisions with Atoms: Applications to X-ray Emission in the Universe

Renata Sade Cumbee

July 25, 2016

Acknowledgments

I would like to thank my many collaborators and coauthors for their support and contributions, namely: David Lyons, Patrick D. Mullen, Robin L. Shelton, David B. Henley, David R. Schultz, Phillip C. Stancil, Ling Liu, Jian-Guo Wang, Rami Ali, Jeff Nolte, and Yong Wu. I would also like to acknowledge Hajime Tanuma for introducing me to the experimental portion of this work.

Most importantly, I would like to thank my advisor, Phillip C. Stancil, for providing guidance throughout my graduate career. Additionally, I would like to gratefully acknowledge the support of my friend and mentor Loris Magnani, for helping me gain confidence in myself and my abilities. I thank Kelly Patton for his help while writing this dissertation. Finally, I would like to thank my mother, Kimberly Freeman, sister, Heather Frasier, and niece and nephew Alexis and Richard for providing love and support for my entire academic career. Without your support, I wouldn't have made it. Thank you!

Contents

Acknowledgements **v**

List of Figures **xv**

List of Tables **xvi**

1 Introduction **1**

1.1 X-rays in the Solar Wind 4

1.2 Other Sources of X-rays 5

1.3 Charge Exchange Calculations 6

2 Methods **10**

2.1 Charge Exchange Cross-Section Calculations 10

2.2 Charge Exchange X-ray Emission Spectra 38

2.3 Summary 63

3 Charge Exchange Emission Model **66**

3.1 Modelling Packages 66

3.2 Model of the Cygnus Loop SNR 68

3.3 Other Line Ratio Comparisons 89

3.4 M82 90

3.5 Summary 96

4 Summary and Outlook **100**

List of Figures

2.1 A pictorial representation of the single electron capture process of CX for C^{6+} colliding with H_2, producing C^{5+} and a photon. 11

2.2 C^{5+} spectrum following C^{6+} CX with H for a collision energy of 1 keV/u. Inset is a schematic Grotrian diagram representing the possible transitions that might result in the spectrum following capture into the $n = 4$ and $n = 5$ capture channels. Recommended cross sections from Janev et al. (1993). Theoretical line ratios are convolved with a 10 eV Gaussian FWHM to produce the spectrum shown. 12

2.3 Ne^{10+}+ He SEC is compared to DCAI and the summed total for the CTMC method at 4.5 keV/u, convolved with a 75 eV Gaussian FWHM resolution. SEC dominates the total with 79% while DCAI contributes 21% of the total (Cumbee et al., 2016a). 15

2.4 C^{6+} + H_2 SEC is compared to DCAI and TI at 10 keV/u. DCAI has a similar contribution to the total spectrum as SEC except for the Lyγ line. Cross sections are calculated using the CTMC method (M. Rakovic and D. R. Schultz 2012, Private Communications). 16

2.5 QMOCC n, ℓ, S-resolved cross sections for the collision of C^{5+}+ H for the $n = 1$ to $n = 4$ states. Singlet states (^1L) are represented with solid lines while triplet states (^3L) are represented with dotted lines. For $E > 10^4$ eV/u, the QMOCC results are merged smoothly to AOCC calculations. Data from Nolte et al. (2012). 21

2.6 n and ℓ-resolved cross sections for the collision of Ne^{10+} with H. Cross-sections are calculated using the AOCC method (Cumbee et al., 2016a). 24

2.7 n and ℓ-resolved cross sections for the collision of Ne^{10+} with H. Cross-sections are calculated using the CTMC method (Cumbee et al., 2016a). 27

2.8 Diabatic potential energy curves for an incoming polarization potential V_i and outgoing Coulomb potential V_f showing the avoided crossing at $R = R_c$ where R is the internuclear distance. The dashed lines indicate the adiabatic potential curves. 30

2.9 n and ℓ-resolved cross sections for the collision of Ne^{10+} with H. Cross-sections are calculated using the MCLZ low-energy ℓ-distribution (Cumbee et al., 2016a). 35

2.10 n and ℓ-resolved cross sections for the collision of Ne^{10+} with H. Cross-sections are calculated using the MCLZ statistical ℓ-distribution (Cumbee et al., 2016a). 36

2.11 New charge exchange cross sections for the collision of Ne^{10+} with H as a function of collisional energy for the dominant capture channel of n=6. The blue (-..) lines represent the MCLZ low energy distribution, the green dotted (...) lines represent the MCLZ statistical distribution, the cyan lines with filled circles represent the CTMC method, and the red lines with squares represent the AOCC method. The solid black line shows our suggested cross sections. . 37

2.12 X-ray emission spectrum including Lyβ and higher lines for the collision of fully ionized O with neutral H for a collisional energy of 0.5, 1, 2, 5, and 10 keV/u (309, 438, 619, 979, and 1384 km/s, respectively). The lines are convolved with a FWHM of 10 eV. For each collisional energy, the Lyβ and higher lines are normalized to the Lyα line. Cross sections are from Janev et al. (1993). 38

2.13 X-ray spectra using MCLZ cross sections with the low energy ℓ-distribution are shown for the collisions of Ne^{10+} with He for collisional energies of 0.1 to 100 keV/u. Lines are normalized to Lyα at 1020 eV. The stick plot is produced directly from the Cascade model, and the line ratios are convolved with a 10 eV FWHM Gaussian to produce the spectra shown. 40

2.14 X-ray emission spectra for the collisions of Ne^{9+} and Ne^{10+} with H. MCLZ cross-sections are used for both collision systems, and for Ne^{10+} the low-energy and statistical ℓ-distributions are both shown. The line ratios are convolved with a 10 eV FWHM Gaussian to produce the spectra shown. 41

2.15 Kα triplet for the CX collision of O^{7+} with H for a collision energy of 1 keV/u and a Gaussian FWHM of 0.07 Å. The G-ratio $\left(\frac{I_f+I_i}{I_r}\right)$ for this collision energy is 2.047. QMOCC cross-sections are used (Nolte, 2016). 44

2.16 Kβ to Kα line ratios for Fe^{25+} collisions with CO, H_2O, He, H_2, and N_2. MCLZ cross-sections are used here. 45

2.17 X-ray spectra using the MCLZ cross sections with the low energy ℓ-distribution are shown for the collisions of Ne^{10+} with H (top panel) and He (bottom panel) at collisional energies of 0.1, 0.5 and 1 keV/u. Lines are normalized to Lyα at 1020 eV with a resolution of 10 eV FWHM. 47

2.18 X-ray spectra using the MCLZ cross sections with the statistical ℓ-distribution are shown for the collisions of Ne^{10+} with H (top panel) and He (bottom panel) at collisional energies of 0.1, 0.5 and 1 keV/u. Lines are normalized to Lyα at 1020 eV with a resolution of 10 eV FWHM. 48

2.19 Ne^{10+} + H X-ray spectra calculated using the AOCC and CTMC cross sections are compared to the MCLZ method at collisional energies of 1 keV/u (black lines) and 5 keV/u (red lines). Lines are normalized to Lyα at 1020 eV with a resolution of 10 eV FWHM. 50

2.20 The CTMC method is compared to the AOCC and MCLZ statistical ℓ-distribution methods for the collision of Ne^{10+} with H at an energy of 10 keV/u (top panel) and 20 keV/u (bottom panel). Lines are normalized to Lyα at 1020 eV with a resolution of 10 eV FWHM. 51

2.21 Experimental single electron capture (SEC) data for Ne^{10+} CX with He at $\sim$ 4.5 keV/u is compared to CTMC, AOCC (Liu et al., 2014), and MCLZ low-energy and statistical distributions for SEC. A resolution of 75 eV FWHM is used for the theoretical methods compared to a resolution of 68 eV for the experimental data (Ali et al., 2010). Note that the experimental spectra includes no multi-electron capture events. 53

2.22 Experimental EBIT measurements for Fe^{25+} CX with N_2 (Wargelin et al., 2005) are compared to theoretical spectra using MCLZ cross sections. 54

2.23 Experimental EBIT measurements for Fe^{26+} CX with N_2 (Wargelin et al., 2005) are compared to theoretical spectra using MCLZ low-energy ℓ-distribution cross sections. The MCLZ methods underestimated the highest order experimental lines, so a modified "shifted" low-energy ℓ-distribution was applied (MCLZSL1). 55

2.24 Experimental EBIT measurements for Fe^{25+} and Fe^{26+} CX with N_2 (Wargelin et al., 2005) are compared to the best attempt for the theoretical spectra using MCLZ low-energy and MCLZ SL1ℓ-distribution cross sections. 56

2.25 Experimental measurements for C^{6+} CX with He for various collision energies (Defay et al., 2013). A Gaussian FWHM of 5 eV is chosen for all collision energies. 59

2.26 Experimental measurements for C^{6+} CX with He at 930 eV/u (420 km/s, Defay et al., 2013) compared to MCLZ statistical calculation at the same energy. A Gaussian FWHM of 5 eV is used. 60

2.27 Experimental measurements for C^{6+} CX with H_2 for various collision energies (Fogle et al., 2014). A Gaussian FWHM of 10 eV is chosen for all collision energies. 61

2.28 Experimental measurements for C^{6+} CX with H_2 at 1 keV/u (451 km/s, Fogle et al., 2014) compared to MCLZ low-energy calculation at the same energy. A Gaussian FWHM of 10 eV is used. 62

2.29 H-like Hardness ratios for collisions with H. Solid lines indicate MCLZ low energy ℓ-distribution calculations. C^{6+} recommended calculations are from Janev et al. (1993), N^{7+} MOCC calculations are from Harel et al. (1998), and O^{8+} recommended cross-sections are from Janev et al. (1993). 64

2.30 He-like Hardness ratios (H) for collisions with H. Solid lines indicate MCLZ calculations. C^{5+} QMOCC calculations are from Nolte et al. (2012), N^{6+} QMOCC calculations are from Wu et al. (2011), and O^{7+} QMOCC cross-sections are from Nolte (2016). 65

3.1 Smoothed 0.3–2.0 keV XIS1 image of the NE4 field of the Cygnus Loop. The image has not been background-subtracted nor flat-fielded. The green polygon shows the region from which we extracted the spectrum of the Cygnus Loop rim. 72

3.2 (a) Spectrum (crosses) from NE4's outermost rim of the Cygnus Loop as described in Figure 1 of Katsuda et al. (2011) along with the best-fit model (lines) including the Absorbed VpShock model. BI spectrum (red), FI spectrum (black). Residuals are shown in the lower panel with a reduced χ^2 of 8.9 with 592 d.o.f. 73

3.3 Same as Figure 3.2, but with the Absorbed VpShock model and CX-inspired lines whose intensities are independently varied in the fit. This figure can be compared to Figure 6 from Katsuda et al. (2011). Residuals show a reduced $\chi^2 = 1.36$ with 533 d.o.f. 74

3.4 a) Same as Figure 3.3, but with the Absorbed VpShock model and theoretical CX data. The normalizations for Kβ and higher are tied to the Kα resonant lines for each ion to more accurately depict CX emission spectra. b) Reduced $\chi^2 = 3.95$ with 555 d.o.f. primarily due to the poor fit near 0.7 keV. 75

3.5 a) Same as Figure 3.4, but with the addition of Fe L-shell lines at 0.726 and 0.822 keV. b) Reduced $\chi^2 = 1.83$ with 553 d.o.f. 76

3.6 CX X-ray emission line ratios for H-like and He-like C-Si ions colliding with H and 10 % fraction of He, with each spectrum having a normalization of 1, indicating a similar abundance for each ion. Line ratios are described in Tables A.2 and A.3. The line ratios are convolved with a 50 eV FWHM Gaussian to produce the spectra shown. 78

3.7 Same as Figure 3.4, but with additional lines including C-Si ions colliding with H and a 10 % fraction of He for a collision energy of 2 keV/u. Reduced χ^2 of 3.7 81
3.8 Same as Figure 3.7, but with the addition of Fe L-shell lines at 0.726 and 0.822 keV. Reduced χ^2 of 1.91 85
3.9 CX X-ray emission line ratios for H-like and He-like C-Si ions colliding with H and 10 % fraction of He extracted from *XSPEC* fits, as shown in Figures 3.7 and 3.8 using 10 eV Gaussian FWHM. 86
3.10 Same as Figure 3.9, but using a 50 eV Gaussian FWHM resolution. 87
3.11 Same as Figure 3.10 (using a 50 eV Gaussian FWHM resolution), but including two lines at 0.726 keV and 0.822 keV to mimic Fe L-shell CX emission. The Fe line at 0.726 is shown in black for the collision energy of 200 eV/u. . 88
3.12 Theoretical X-ray emission lines for H-like and He-like C, N, and O ions colliding with H and a fraction of 10% He for the Fast solar wind ($\sim$ 750 km/s) and slow solar wind ($\sim$ 400 km/s). A Gaussian FWHM of 10 eV is used. . . 91
3.13 Theoretical X-ray emission lines for H-like and He-like C-Si ions colliding at 1 keV/u with H and varying the fraction of He from 0 % He (100 %H) to 75 % He (25 % H). All line-ratio spectra are normalized to a value of 1, and the black line shown with a fraction of 10% He can be compared to the black line shown in Figure 3.6 with the same collision energy. A Gaussian FWHM of 10 eV is used. 92

3.14 Line ratios (Lyβ/Lyα) for the three methods shown in Figures 2.18-2.19 as a function of collisional energy for charge exchange of Ne^{10+} with H. The vertical lines represent the Disk, Wind-1, Wind-2, and Wind-3 regions of M82 as described by Konami et al. (2011). The results from the *ACX* model (Zhang et al., 2014) are also shown. Note that the results from Konami et al. (2011) and Zhang et al. (2014) have no ion kinetic energy dependence and their placement on the right side of the plot is arbitrary. 97

3.15 Same as Figure 3.14 but for the collision of Ne^{10+} with He. Also shown is the addition Ne^{10+} with 90% H and 10% He, which is the assumed ratio of the He to H charge exchange contributions. CTMC, AOCC, and experimental Ne^{10+} + He data at 4.55 keV/u (see Figure 2.21) are also compared. 98

List of Tables

1.1 Calculations and experimental benchmarking discussed in this dissertation . 9

2.1 AOCC Cross Sections for C^{6+} +He. 22

2.2 X-ray line ratios for H-like C^{6+} CX with H 42

2.3 X-ray line ratios for H-like C^{5+} CX with He 43

3.1 Model Line Normalizations for Charge Exchange with H and 10% He 82

3.2 Model Line Normalizations for Charge Exchange with H and 10% He with Fe L-Shell Lines 83

3.3 Abundance ratios (relative to O) for ions in the solar wind. 89

A.1 Model Line Normalizations 116

A.2 Charge Exchange X-ray Emission with H Targets 118

A.3 Charge Exchange X-ray Emission with He Targets 124

Chapter 1

Introduction

First documented by Wilhelm Conrad Roentgen in 1895, X-rays are a very useful tool in astronomy. X-rays have been observed from black holes, neutron stars, binary star systems, supernova remnants, the sun, and even from comets. They have rather short wavelengths (0.01 to 10 nm) and thus high energies (100 eV to 100 keV), and are produced via electron processes in two forms: Bremsstrahlung X-rays and characteristic X-rays. Bremsstrahlung X-ray radiation is produced when electrons are decelerated when deflected by an atomic nucleus. As the moving electron loses kinetic energy, X-ray photons are produced, satisfying the law of conservation of energy. While the Bremsstrahlung spectrum is continuous, the X-rays produced when electrons transition between electronic states or energy levels, called characteristic X-rays, are discrete. The X-ray energies are determined by the energies of the initial and final energy level for the transition. The characteristic X-rays vary depending on what process causes the electron to be in an excited energy level, resulting in these X-ray spectra being characteristic of the process as well.

One process that produces astrophysical X-rays is radiative recombination, which takes place when a positively charged ion captures an electron to one of its bound orbits with a simultaneous emission of a photon:

$$e^- + A^{q+} \rightarrow A^{(q-1)+} + \gamma. \tag{1.1}$$

Electron impact ionization is another interesting process in which an electron collides with an atom or molecule, exciting one of the electrons into an excited energy level:

$$e^- + A \rightarrow A^* + e^-. \tag{1.2}$$

Charge exchange (CX), which is the focus of this dissertation, is a process in which an electron is transferred from a neutral atom or molecule to an ion in an excited energy level:

$$A^{q+} + B \rightarrow A^{(q-1)+*} + B^+. \tag{1.3}$$

Each of these processes produce X-rays that are characteristic for the individual process and play an important role in various astrophysical environments. It is important to understand the X-ray spectra produced via each process so that we might have a better understanding of the astrophysical environments from which these X-rays are observed.

Within an environment in which a hot plasma interacts with a cool neutral gas, the process of charge exchange might occur and can dominate the observed ion emission spectra. During a CX collision, an ion X^{q+} captures an electron from a neutral atom creating a highly excited ion $X^{(q-1)+}(n\ell\ ^{2S+1}L)$ that then emits one or more photons in a cascade down to the ground state. Recent observations have shown that CX may make a significant contribution to the X-ray emission spectra observed in various astrophysical environments within our solar system including solar wind (SW) charge exchange (SWCX) with neutral gases in comets (Lisse et al., 1996; Cravens, 1997), the heliosphere (Robertson et al., 2001; Crowder et al., 2012), and planetary atmospheres (Cravens et al., 2003; Hui et al., 2009), and outside of our solar system such as in galaxy clusters (Lallement, 2004). Spectra from the *XMM-Newton* Reflection Grating Spectrometer (RGS) and *Suzaku* suggest that CX may have a

significant contribution in the observed soft X-ray emission spectra of supernova remnants (SNRs, Katsuda et al., 2011, 2012; Cumbee et al., 2014, etc) and star forming galaxies (Konami et al., 2011; Cumbee et al., 2016a). Sky surveys in the soft X-ray band (0.1-1.5 keV) including the Wisconsin sky survey (McCammon and Sanders, 1990), with *ROSAT* (Snowden et al., 1998), with microcalorimeters on a sounding rocket (McCammon et al., 2002), with the *Chandra X-ray Observatory* (Markevitch et al., 2003; Wargelin et al., 2004), with *XMM-Newton* (Snowden et al., 2004), and with the Japanese X-ray satellite *Suzaku* (Fujimoto et al., 2007; Smith et al., 2012) have revealed that the soft X-ray background (SXB), once thought to be dominated by thermal emission from the local hot bubble, is produced by a complex combination of X-ray sources. Cox (1998) suggested that a significant portion of the SXB may be due to CX emission from the interaction of heliospheric neutrals and solar wind ions.

Observations from *Chandra* and *XMM-Newton* have shown a spatial correlation between Hα and X-ray enhancements in a variety of astronomical environments (Lallement, 2004). X-ray emission has been shown to be prominent in observations of hot plasma environments, and Lallement (2004) and Konami et al. (2011) have suggested that X-ray emission observed from the hot outflow of starburst galaxies such as NGC 253 and M82 may partially be due to CX in which a highly ionized plasma collides with cold gas. Specifically, Konami et al. (2011) suggest that CX emission from Ne X and other highly charged ions may make a significant contribution to the spectra. Soft X-ray emission in Galactic high velocity clouds (HVCs) has been observed along regions with observed Hα emission. It is understood that the interaction between the fast cold gas of the HVCs and the hot gas from the Galactic halo are the cause of this emission, but Henley et al. (2015b) and Lallement (2004) suggest that CX may be the mechanism that produces the observed emission. CX may also contribute to the X-ray emission of cooling flows of hot gas into the intracluster medium in galaxy clusters (Lallement, 2004). A better understanding of CX emission in these environments can help

constrain ion and neutral densities as well as give some insight into what other environments CX may be prominent.

Heavy elements such as C, N, O, Si, and Fe are produced inside massive stars through nuclear fusion and then released into the interstellar medium through stellar winds and supernova explosions, enriching nearby star forming clouds. It is important to understand the dynamics and physical processes that transfer heavy ions into these star forming galaxies because they contribute significantly to the chemical enrichment of the universe. As the origins of these diffuse X-ray plasmas are unknown, we need to clearly resolve the X-ray emission lines. Using X-ray microcalorimeter detectors, unidentified emission lines will be more easily separated from known thermal emission lines, allowing identification of non-thermal lines which will help us understand the physical processes and the origin of the diffuse X-ray emission. Similarly, X-rays from SWCX which may contaminate all extrasolar observations made by microcalorimeters (Henley et al., 2015a) will be more easily identified and removed.

1.1 X-rays in the Solar Wind

The solar wind is a stream of charged particles and ions that are released from the Sun's corona, or outermost atmosphere. It is composed of approximately equal amounts of electrons and ions, with the ion composition being primarily H^+ with a small amount of He^{2+} and a smaller fraction of heaver ions. The density and velocity of the solar wind varies with the $\sim$ 11 year solar cycle, with an average velocity of $\sim$ 450 km/s. As the solar wind approaches cool bodies within the heliosphere, charge exchange collisions might occur.

While astrophysically, CX was first discovered in the atmosphere of Comet Hyakutake, it was previously suggested that the process of CX might produce the X-ray spectra observed from Jupiter (Horanyi et al., 1988), but the resolution of the *ROSAT* and *Einstein* satellites,

it was not possible to determine which process produced the observed X-rays. More recently, the CX process has been studied extensively in comets throughout our solar system (Beiersdorfer et al., 2001; Lisse et al., 2001; Krasnopolsky et al., 2004; Bodewits et al., 2007; Ewing et al., 2013; Snios et al., 2016). It was soon realized that CX collisions might contribute to the X-rays observed in the atmospheres of Mars (Holmström et al., 2001; Dennerl, 2006), and Venus (Dennerl et al., 2002). *Chandra* observations suggest that the solar wind might be the source of the ionic plasma interacting with the non-magnetic planets Mars and Venus in the same way it interacts with comets (Dennerl, 2010), but for magnetic planets such as Jupiter (Horanyi et al., 1988; Cravens et al., 2003), the presence of a strong magnetic field accelerates and deflects heavy atmospheric ions and increases the fraction of highly charged ions at low collisional energies, resulting in charge exchange collisions (Kharchenko et al., 2008).

1.2 Other Sources of X-rays

1.2.1 Cygnus Loop

After interpreting *Suzaku* observations, Katsuda et al. (2011) suggested that the outer rim of the Cygnus Loop may be a prime example of extrasolar CX X-ray emission. In their comparisons between the observed spectra and a model that included shocked gas and an X-ray background, they were unable to fully reproduce the spectra, which suggested that CX may be missing from their model. They adjusted their model by including lines with relevant energies and widths but arbitrary intensities to mimic CX emission spectra. In order to improve upon the Katsuda et al. (2011) approach, we replace their CX-inspired lines with theoretical CX data to model X-ray emission in the rim of the Cygnus Loop. A CX X-ray emission model of the Cygnus Loop using C, N, O, Ne, Mg, Al, and Si will be discussed in Chapter 3.

1.2.2 M82

Starburst galaxies are a primary source for ejecting metals and energy into the intergalactic medium. X-rays are observed from hot outflows in these galaxies, driven by supernova explosions and stellar winds. Previous studies have suggested that these X-rays are produced via atomic transitions in thermally excited hot gas, but recent studies suggest that they might also be due to charge exchange between highly ionized ions and neutral species (Lallement, 2004). The ratio of the Kα forbidden and intercombination lines to the Kα resonant line for He-like ions can be indicative of charge exchange. Liu et al. (2012) and Zhang et al. (2014) have studied the the O^{7+} Kα triplet for various starburst galaxies with results suggesting that CX may contribute to the X-ray emission. For M82, they note that for different regions of the galaxy, the ratio varies. In this galaxy, the Ne^{10+} Lyβ/Lyα line ratio has also been shown be in excess of predictions for thermal electron impact excitation (Konami et al., 2011). This line ratio is discussed in more detail in Chapter 3.

1.3 Charge Exchange Calculations

Charge exchange is a fundamental atomic collision process to which the X-ray spectra of various astrophysical environments have been attributed (see, for example, Dennerl, 2010; Krasnopolsky et al., 2004). In this process (also referred to as charge transfer or electron capture), X-ray emission is a consequence of a highly charged ion capturing an electron from another atom,

$$A^{q+} + B \rightarrow A^{(q-1)+}(nl\ ^{2S+1}L) + B^{+}, \tag{1.4}$$

to form a highly excited, high charge state ion $A^{(q-1)+}(nl\ ^{2S+1}L)$ (where n is the principal quantum number, ℓ is the orbital angular momentum quantum number and L the total orbital angular momentum number, and S is the total spin quantum number) . To accu-

rately model charge exchange emission spectra, it is essential to include the effects of many ionization stages, q, and donor (neutral target) species, B, for a given element (projectile) A.

While a variety of ingredients go into an X-ray model, an important component is the CX cross sections for capture into individual ion quantum states which are known to have sensitive dependencies on the ion velocity. Information on CX cross sections is rarely known at a detailed level, so current X-ray models have had to depend on approximate scaling laws or multi-parameter fits to laboratory measured X-ray spectra. The reliability of the existing CX data is not uniform and lacks sufficiently broad or systematic coverage of the projectile and target combinations and energy ranges important to astrophysics. Furthermore, measurements of state-selective cross sections are rare and difficult to perform. The optimal method to obtain state-selective cross sections is through direct measurement or calculation. The results of either can then be compared to measured spectra as a consistency check. The considerable uncertainties of estimated state-selective cross sections translate to significant uncertainties in the models resulting in questionable astrophysical deductions.

Four different methods of calculating CX cross-sections will be discussed in this dissertation which are relevant at different collision energies. § 2.1.1 discusses the most reliable theoretical approach, the quantum-mechanical molecular-orbital close-coupling (QMOCC) method, in which the CX system is considered as two interacting molecular electronic states. The atomic orbital close-coupling method, discussed in § 2.1.2 considers the same system as two interacting atomic orbitals. The classical trajectory Monte-Carlo method, discussed in § 2.1.3, simulates collisions between ions and neutral atoms or molecules by sampling many trajectories for initial electronic orbits with a large ensemble of configurations. Finally, the multi-channel Landau-Zener method, discussed in § 2.1.4 requires the least amount of numerical calculation, and considers the avoided crossings (R_C) of two adiabatic potential energy curves, representing the initial and final potential energies of the system. In general, the

more accurate methods can be quite difficult to produce, and thus only a limited amount of data are currently available for the QMOCC, CTMC, and AOCC methods. The MCLZ method, while it is not the most accurate, it is the easiest method to produce realistic calculations for a variety of collision energies and ion-neutral reactions, and so cross sections can be readily computed for a variety of systems.

Experimental benchmarking, discussed in Chapter 2, is useful for determining how accurately theoretical CX cross-sections produce realistic spectra. When cross-sections are available for a variety of methods, experiments can also be useful for determining which cross-sections are most accurate at different collision energies. Neutral H is the most simplistic neutral target considered in CX calculations as it only has a single electron, and it is abundant throughout the Universe. However, it is difficult to produce a neutral H gas in the laboratory. This results in most experiments being performed using other neutral targets that are often less important in most astrophysical environments, including H_2, He, and N_2 discussed in this dissertation. QMOCC, AOCC, and CTMC calculations have been performed for a limited set of astrophysically important ion collisions with H and He, and when other data were not available, MCLZ calculations were performed. Some available CX experiments were extracted from the literature and compared to spectra produced primarily with MCLZ cross-sections. Table 1.1 provides a list of ion-neutral target calculations and experiments discussed here.

Table 1.1: Calculations and experimental benchmarking discussed in this dissertation

Ion	Targets	Methods	Experiment (Target and energy)
C^{5+}	H, He, H_2	QMOCC, AOCC, CTMC, MCLZ	
C^{6+}	H, He, H_2	Recommended, CTMC, AOCC (He)	He (464 eV/u to 18 keV/u) H_2 (910 eV/u to 27 keV/u)
N^{6+}	H, He	QMOCC, AOCC, CTMC, MCLZ	
N^{7+}	H, He	MOCC, MCLZ	
O^{7+}	H, He	QMOCC, AOCC, CTMC, MCLZ	
O^{8+}	H, He	Recommended	
Ne^{9+}	H, He	MCLZ	
Ne^{10+}	H, He	AOCC, CTMC, MCLZ	He (4.5 keV/u)
Mg^{11+}	H, He	MCLZ	
Mg^{12+}	H, He	MCLZ	
Si^{12+}	H, He	MCLZ	
Si^{13+}	H, He	MCLZ	
Fe^{25+}	CO, H_2O, He, H_2, N_2	MCLZ	N_2 (10 eV/u)
Fe^{26+}	N_2	MCLZ	N_2 (10 eV/u)

Relative Line intensities are shown for all ions considered in this dissertation colliding with H. For this table, QMOCC cross sections are used when available for C^{5+} + H (Nolte et al., 2012), N^{6+} + H (Wu et al., 2011), and O^{7+} + H (Jeff Nolte, Private communication). AOCC cross-sections are then used for Ne^{10+} + H for energies above 1 keV/u, while CTMC cross-sections are used for energies below 1 keV/u(Cumbee et al., 2016a). For C^{6+} + H and O^{8+} + H, recommended cross-sections from Janev et al. (1993) are used, and for N^{7+} +H (Harel et al., 1998), MOCC cross-sections are used. In all other cases, and when energies are missing for the more "accurate" methods, below 1 keV/u, MCLZ low-energy ℓ-distribution cross sections are used, and for energies at and above 1 keV/u, MCLZ statistical ℓ-distribution cross-sections are used.

Chapter 2

Methods

2.1 Charge Exchange Cross-Section Calculations

In the process of Charge Exchange (CX), an ion (A^{q+}) with charge state q collides with a neutral target (B), transferring an electron from the neutral target into a highly excited, high charge state of the ion $A^{(q-1)+*}(n'\ell')$, releasing kinetic energy (ΔE). The electron then transitions to the lowest energy state with a probability given by the Einstein A coefficient (s^{-1}) for spontaneous emission, emitting at least one photon γ. To accurately model charge exchange emission spectra, it is essential to include the effects of many ionization stages, q, and donor (neutral target) species, B, for a given element (projectile) A. Figure 2.1 shows a pictorial representation of charge exchange as an electron is captured from the H_2 neutral to the bare C^{6+} ion, resulting in a photon emitted from the C^{5+} ion.

For a single electron-system in which a bare ion (A^{q+}) collides with a target (B) with a single electron (H, for example), the process of single electron capture (SEC) occurs. SEC follows the following steps:

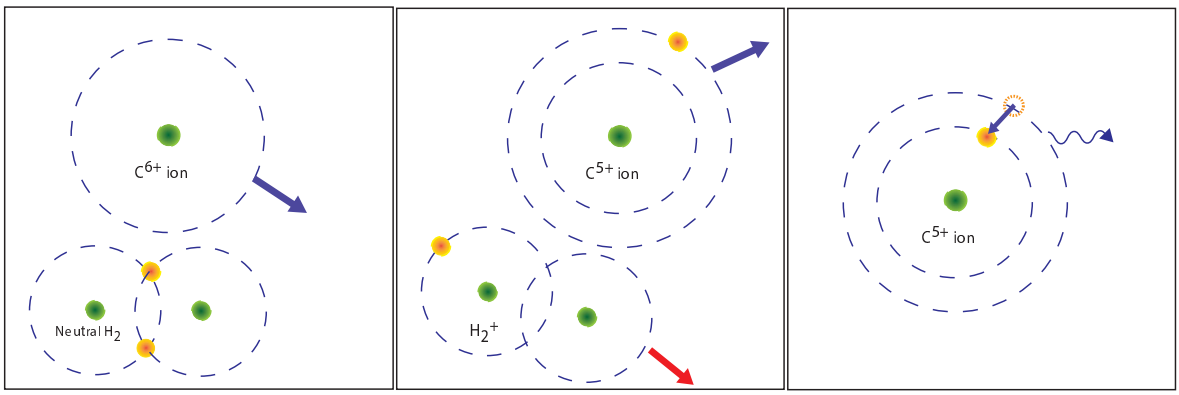

Figure 2.1: A pictorial representation of the single electron capture process of CX for C^{6+} colliding with H_2, producing C^{5+} and a photon.

$$\begin{aligned} A^{q+} + B &\rightarrow (AB)^{q+} \\ &\rightarrow A^{(q-1)+*}(n'\ell') + B^{+} + \Delta E \\ &\rightarrow A^{(q-1)+}(n\ell) + B^{+} + \Delta E + \gamma. \end{aligned} \tag{2.1}$$

During the collision, the ion and target form a quasi-molecular state $(AB)^{q+}$, and immediately after the collision the ion is in an excited state $A^{(q-1)+*}(n'\ell')$ which then relaxes down to the lowest energy state $A^{(q-1)+}(n\ell)$, stabilizing the system and emitting a photon γ. Figure 2.2 shows an example of the X-ray emission spectrum resulting from a collision of C^{6+} with H with a collision energy of 1 keV/u. Inset is a Grotrian schematic diagram representing the possible transitions that might occur to produce the C^{5+} spectrum after the electron is transferred into the $n = 4$ or $n = 5$ levels. Note that the Lyα line is dominant due to cascade to the $2p$ state from the higher n-levels.

In the case that the target atom or molecule has multiple electrons (He or H_2, for example), along with SEC, multiple electron capture (MEC) can occur in which more than one

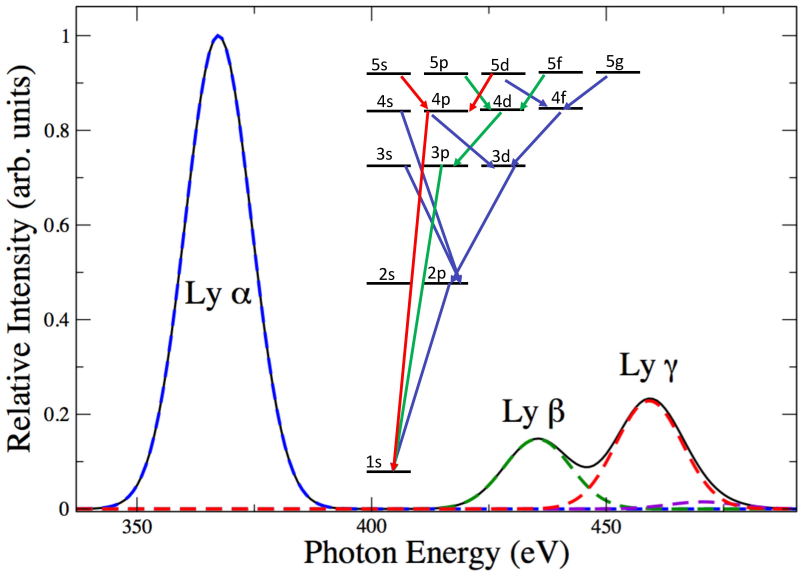

Figure 2.2: C^{5+} spectrum following C^{6+} CX with H for a collision energy of 1 keV/u. Inset is a schematic Grotrian diagram representing the possible transitions that might result in the spectrum following capture into the $n = 4$ and $n = 5$ capture channels. Recommended cross sections from Janev et al. (1993). Theoretical line ratios are convolved with a 10 eV Gaussian FWHM to produce the spectrum shown.

electron is transferred during the CX process. The simplest MEC process is double electron capture (DEC). For DEC, there are three reaction channels. In the process of true double capture (TDC),

$$\begin{aligned} A^{q+} + B &\rightarrow A^{(q-2)+*}(n''\ell'', n'''\ell''') + B^{2+} \\ &\rightarrow A^{(q-2)+}(n\ell, n'\ell') + B^{2+} + \gamma_{'} + \gamma_{''}, \end{aligned} \tag{2.2}$$

both electrons are transferred to the ion in an excited state before relaxing to the lowest energy state, emitting photons. In the case of double capture autoionization (DCAI),

$$\begin{aligned} A^{q+} + B &\rightarrow A^{(q-2)+*}(n''\ell'', n'''\ell''') + B^{2+} \\ &\rightarrow A^{(q-1)+*}(n'\ell') + B^{2+} + e^{-}, \end{aligned} \tag{2.3}$$

both electrons are transferred to the ion (double capture) in an intermediate doubly-excited state, and one electron then autoionizes, resulting in the same final state as SEC. It is important to note that the X-ray spectra produced for TDC and DCAI are distinct and thus characteristic for the double capture reaction processes (Ali et al., 2016). For transfer ionization (TI), as one electron is transferred to the ion, the second electron is ionized as

$$\begin{aligned} A^{q+} + B &\rightarrow A^{(q-1)+*}(n'\ell') + B^{2+} + e^{-} \\ &\rightarrow A^{(q-1)+}(n\ell) + B^{2+} + e^{-} + \gamma, \end{aligned} \tag{2.4}$$

which also results in the same final state as SEC. Ali et al. (2005) suggest that ignoring MEC of A^{q+} ions can lead to overestimating the relative abundance of the $A^{(q-1)+}$ ions in the solar wind because, for the example of $Ne^{9+,10+}$, each observed He-like X-ray will be attributed

to SEC of Ne^{9+}, but some may be due to MEC of Ne^{10+}. Figures. 2.3 and 2.4 show a comparison of these processes to the total CX X-ray emission spectra for Ne^{10+} with He and C^{6+} with H_2. For Ne^{10+} CX with He in Figure. 2.3, the SEC process dominates the total spectrum when compared to DCAI, but for the C^{6+} CX collision with H_2 in Figure. 2.4, the DCAI process contributes as much as the SEC process for the Lyα and Lyβ lines, but has a very small contribution to the Lyγ line. While SEC is usually the most important capture channel in slow collisions (Hasan et al., 2001), the MEC processes may make a significant contribution to the X-ray emission spectra of multi-electron systems. A technique that is capable of differentiating between various reaction channels is required to fully analyze observed spectra (Beiersdorfer et al., 2003).

The first step in producing CX X-ray emission spectra is calculating the n, ℓ, S-resolved cross sections. In general, the cross-section is an effective area that describes the likelihood of a scattering event to happen. The most simplistic cross-section for a spherical target is given by $\sigma = \pi R^2$ where R iis the effective radius of the target or the internuclear distance at which the scattering event occurs. When incorporating quantum mechanical effects, the calculations of the cross sections becomes more difficult.

In order to calculate cross-sections for the charge-exchange process, one may start with the time dependent Schrödinger equation

$$H\Psi = i\frac{\partial}{\partial t}\Psi(\vec{r}, R(t)) \tag{2.5}$$

and the Hamiltonian is given by

$$H = -\frac{1}{2}\nabla_r^2 - \frac{q}{r_A} - \frac{1}{r_B} - \frac{1}{2}\nabla_R^2 + \frac{q}{R} \tag{2.6}$$

where r_A is the distance between the electron and the ion and r_B is the distance between the electron and the target nucleus. Upon finding a solution, the transition probability for

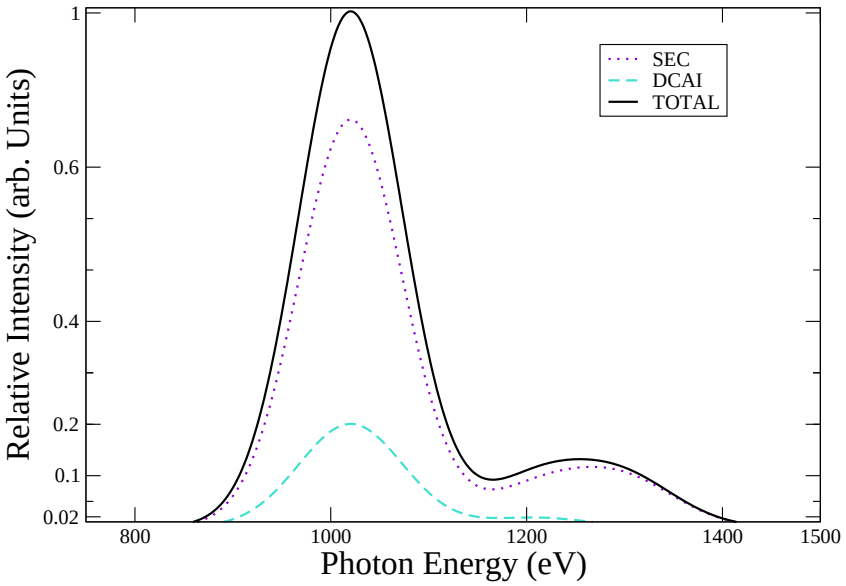

Figure 2.3: Ne^{10+}+ He SEC is compared to DCAI and the summed total for the CTMC method at 4.5 keV/u, convolved with a 75 eV Gaussian FWHM resolution. SEC dominates the total with 79% while DCAI contributes 21% of the total (Cumbee et al., 2016a).

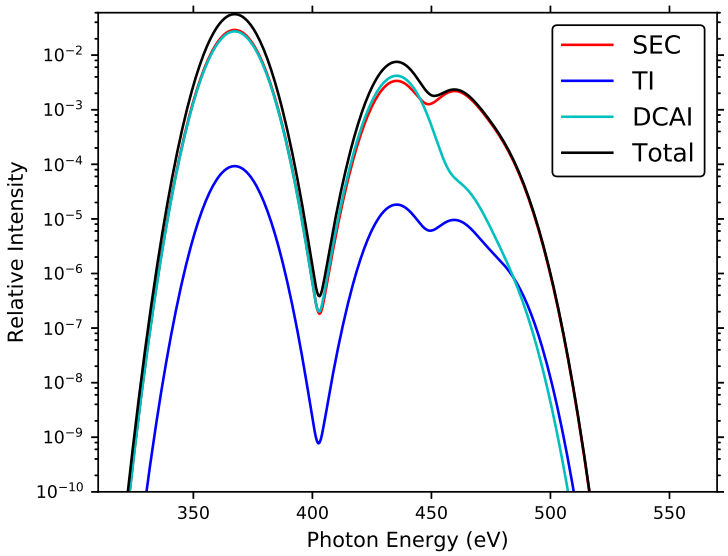

Figure 2.4: C^{6+} + H_2 SEC is compared to DCAI and TI at 10 keV/u. DCAI has a similar contribution to the total spectrum as SEC except for the Lyγ line. Cross sections are calculated using the CTMC method (M. Rakovic and D. R. Schultz 2012, Private Communications).

an electron transferred from the initial state i to the final state f is given by

$$P_{i\to f} = |c_f(t \to \infty)|^2 \tag{2.7}$$

where c_f is a transition amplitude. The total cross-section can then be calculated by integrating the transition probability over all possible impact parameters (b) as

$$\sigma_{i\to f} = 2\pi \int_0^{b_{max}} P_{i\to f} b \; db. \tag{2.8}$$

Essentially, the "problem" of charge exchange is in calculating the transition probability in Eq. (2.7) and solving Eq. (2.8). In this thesis, four methods for calculating CX cross sections will be used. They will each be discussed in the subsequent sections. The quantum me-

chanical molecular orbital close-coupling (QMOCC), Atomic-orbital close-coupling (AOCC), Classical-trajectory Monte-Carlo (CTMC), and multi-channel Landau-Zener (MCLZ) methods will be discussed.

While the basic CX process has been studied for decades, a reliable set of n, ℓ and/or S-resolved cross-sections is not available for important ion-neutral interactions and energies. Measurements of state-selective cross sections are rare and difficult to perform. The energy resolution is typically poor or the studies are restricted to the measurements of a few final states due to limited detector wavelength ranges. Improvements have been made with experiments to directly measure the X-ray spectrum (Greenwood et al., 2001), but the measurement is of the total spectrum including the photons from all routes of the cascade. Hence, to directly determine state-selective cross section data, one must turn to theoretical methods. For product ions with more than one electron, or for collisions on He, the status and reliability of calculated cross sections is generally lower than for H. Therefore, there is a need for measured cross sections for an estimation of them via empirical methods in addition to theoretically predicted results.

2.1.1 Quantum Mechanical Molecular-Orbital Close-Coupling

The quantum-mechanical molecular-orbital close coupling (QMOCC) method is the most accurate method, from the lowest energies to $\sim$ 1 keV/u, considered in this dissertation. This approach considers the charge exchange system as a multi-electron two Coulomb-center problem for incident bare ion cases. Calculations are performed in two steps. First, the molecular orbitals, energies, and coupling matrix elements are calculated, and then the coupled equations are solved as a quasi-molecular system. The one caveat with QMOCC calculations is dealing with the electronic structure calculations.

In the quantal-perturbed stationary state method (Kimura and Lane, 1989), the coupled radial Schrödinger equations are solved for the coefficients $F_i(r)$ of the molecular orbitals

$\psi_i(s,R)$ (orthogonal eigenstates of the adiabatic Hamiltonian) in the expansion of the total wavefunction (Zygelman et al., 1992)

$$\Psi = \sum_j \psi_j(s,R) F_j(R) \tag{2.9}$$

where R is the nuclear position vector and s is the position of the electron with respect to the center of mass of the quasi-molecule. The coupled radial equations are then given by

$$\left[\frac{\partial^2}{\partial R^2} - \frac{\hat{J}_i^2 - \Lambda_i^2}{R^2} + k_i^2(R)\right] RF_i(R) = \sum_j [V_{ij}^R(R) + V_{ij}^C(R)] RF_j(R) \tag{2.10}$$

where $k_i(R)^2 = -2\mu(\epsilon_i(R) - E)$, $\epsilon_i(R)$ is the adiabatic potential energy curve for the ith orbital, E is the collision energy, Λ_i is the projection of the electronic angular momentum on the internuclear axis for state i, and μ is the nuclear reduced mass. $V_{ij}^R(R)$ and $V_{ij}^C(R)$ are the radial and rotational couplings. They are of the form

$$V_{ij}^R(R) = \Big[\langle i| - \frac{\partial}{\partial R^2} + \frac{L_x^2 + L_y^2}{R^2}|j\rangle - 2\langle i|\frac{\partial}{\partial R}|j\rangle \frac{\partial}{\partial R}\Big]\delta_{\Lambda_i,\Lambda_j} \tag{2.11}$$

and

$$V_{ij}^C(R) = \frac{2}{R^2}\Big[i\langle i|L_y|j\rangle \frac{\partial}{\partial \Theta} - \langle i|L_x|j\rangle \Big(\frac{i}{\sin\Theta}\frac{\partial}{\partial \Phi} - \Lambda_J \cot\Theta\Big)\Big] \tag{2.12}$$

in terms of the body fixed angular momentum operators L_x and L_y and polar coordinates R, Θ, Φ, and $\vec{R}$ in the space-fixed frame.

They can be reduced to

$$V_{ij}^R(R) = -2\Big\langle i\Big|\frac{\partial}{\partial R}\Big|j\Big\rangle \frac{\partial}{\partial R}\delta_{\Lambda_i\Lambda_j} \tag{2.13}$$

for the nonadiabatic radial coupling, while nonadiabatic rotational coupling (Nolte et al.,

2012) is given by

$$V_{ij}^{C}(R) = \frac{2i}{R^2}\langle i|L_y|j\rangle\frac{\partial}{\partial\Theta}. \tag{2.14}$$

Eqation (2.10) can be solved for $F_i(R)$, but it is more convenient to introduce a new amplitude. Transitions between states of the same symmetry ($^{2S+1}\Lambda$, where S is the total electronic spin quantum number), are driven by the term $\langle i|\frac{\partial}{\partial R}|j\rangle$. In order to prevent the radial coupling equation (2.13) from becoming singular near an avoided crossing due to this term, a unitary transformation of the molecular orbitals is made to a diabatic basis set so that the term vanishes. The molecular orbitals are now expanded in terms of diabatic molecular orbitals as

$$\psi_i^d(\vec{s},R) = \sum_i C_{ij}(R)\psi_j(\vec{s},R), \tag{2.15}$$

such that the symmetry is preserved. The adiabatic channel functions $F_i(R)$ transform as

$$F_i(\vec{R}) = \sum_j C_{ij}(R)G_j(\vec{R}) \tag{2.16}$$

where C_{ij} are chosen so that $\langle i|\frac{\partial}{\partial R}|j\rangle$ vanishes. $G_j(\vec{R})$ is the partial wave decomposition amplitude,

$$G_j(\vec{R}) = \frac{1}{R}\sum_{J,M} g_j^J(R)H_{M,\Lambda_J}^J(\Theta,\Phi), \tag{2.17}$$

where H_{M,Λ_J}^J is a function of the polar angles and reduces to a spherical harmonic function when $M = 0$. Inserting Eqs. (2.13), (2.14) , and (2.16) into Eq. (2.10) results in the coupled channels for a given channel i

$$\begin{aligned}\left[\frac{\partial^2}{\partial R^2}Z\frac{\Lambda_i^2 - J(J+1)}{R^2} + 2\mu E\right] g_i^J(R) \\ = \sum_j [{}^d V_{ij}^C(R) + {}^d\, V_{ij}^R(R) + 2\mu U_{ij}(R)] g_j^J(R)\end{aligned} \tag{2.18}$$

where $U_{ij}(R) = \sum_k C_{ik}^\dagger(R)\epsilon_k(R)C_{kj}(R)$. The coupled equations can now be written in matrix form such that

$$\Big[\frac{\partial}{\partial R^2}\underline{I} + \underline{\mathcal{V}}^J(R)\Big] G^J(R) = 0 \tag{2.19}$$

where $G^J(R)$ is a solution to Eq. (2.18) and the matrix elements of $\underline{\mathcal{V}}^J(R)$ are given by

$$\mathcal{V}_{ij}^R(R) = \frac{\Lambda_i^2 - J(J+1)}{R^2}\delta_{ij} + 2\mu(E\delta_{ij} - U_{ij}(R)) - {}^d\, V_{ij}^C(R) - {}^d\, V_{ij}^R(R). \tag{2.20}$$

The boundary conditions of the solutions $\underline{G}^J(R) = \underline{\mathcal{T}}^J(R) + \underline{\mathcal{N}}^J(R)\underline{\mathcal{K}}^J$ where $\underline{\mathcal{K}}^J$ is the reaction matrix, a real symmetric matrix, and $\underline{\mathcal{T}}^J(R)$ and $\underline{\mathcal{N}}^J(R)$ are spherical Bessel and Coulomb functions for the ion-neutral channels (Nolte, 2011). Solving this set of coupling equations results in the K^J matrix, which we can then find the scattering matrix S^J from

$$S^J = [I + iK^J][I - iK^J]^{-1}, \tag{2.21}$$

and the charge exchange cross section from the initial channel i to the final channel j is given by

$$\sigma_{ij} = \frac{\pi p_0}{2\mu(\epsilon_i(R) - E)}\sum_J (2J+1)|S_{ij}^J|^2 \tag{2.22}$$

where the probability of approach factor p_0 depends on the molecular symmetry of the initial channel for a given collision system. A sample of $n, \ell,$ and S-resolved cross-sections calculated using the QMOCC method are shown in Figure 2.5 for the collision of C^{5+} with

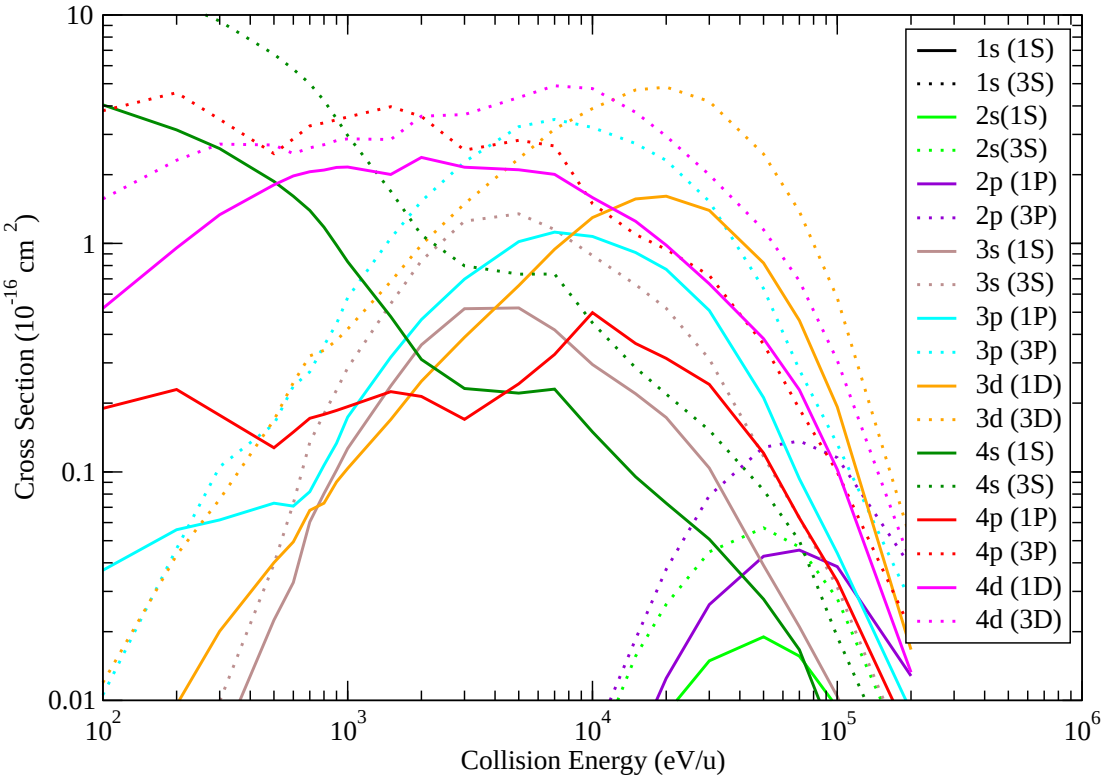

Figure 2.5: QMOCC n, ℓ, S-resolved cross sections for the collision of C^{5+}+ H for the $n = 1$ to $n = 4$ states. Singlet states (^1L) are represented with solid lines while triplet states (^3L) are represented with dotted lines. For $E > 10^4$ eV/u, the QMOCC results are merged smoothly to AOCC calculations. Data from Nolte et al. (2012).

.

Table 2.1: AOCC Cross Sections for C^{6+} +He.

Collision Energy	Cross sections (10^{-16} cm^2)										
(eV/u)	4f	4d	4p	4s	3d	3p	3s	2p	2s	1s	Total
500	0.06	0.07	0.02	0.17	1.35	1.87	0.80	0.0	0.0	0.0	4.2
1000	0.06	0.20	0.19	0.07	3.61	3.59	1.81	0.0	0.0	0.0	9.3
2000	0.18	0.38	0.23	0.13	3.97	4.40	3.07	0.0	0.0	0.0	12.4
4000	0.56	0.52	0.22	0.08	4.43	5.10	3.09	0.0	0.0	0.0	14.0
8000	1.05	0.58	0.28	0.05	5.12	6.01	2.74	0.0	0.0	0.0	15.8
15000	2.61	1.28	0.38	0.13	5.93	5.35	1.58	0.0	0.0	0.0	17.3
25000	3.59	1.10	0.50	0.09	6.04	3.61	0.91	0.0	0.0	0.0	15.8
50000	3.21	0.96	0.44	0.09	5.79	2.55	0.51	0.0	0.0	0.0	13.6

Data from Fritsch and Lin (1991).

H.

2.1.2 Atomic-Orbital Close-Coupling

The Atomic Orbital Close-Coupling (AOCC) method for the description of ion-atom collision processes is discussed in detail in Fritsch and Lin (1991), but shall be outlined briefly here. This method is relevant from intermediate ($\sim$ 100 eV/u) to high ($\sim$ 500 keV/u) energies. For a one-electron two-center collision system, the total electron scattering wave function is expanded over the traveling atomic orbitals which are centered on the projectile nuclei and the target nuclei. Here, the determination of electronic states centered on the target and on the projectile is performed by using the variational method with even-tempered trial functions (Kuang and Lin, 1997; Reeves, 1963). They are given by

$$\chi_{klm}(\vec{r}) = N_l(\zeta_k) e^{\zeta_k r} \mathcal{Y}_{lm}(\vec{r}) \tag{2.23}$$

where $\mathcal{Y}_{lm}$ consists of a spherical harmonic multiplied by r^l

$$\mathcal{Y}_{lm}(\vec{r}) = r^l Y_{lm}(\vec{r}), \tag{2.24}$$

and $N_l(\zeta_k)$ is a normalization constant, $\zeta_k = \alpha\beta^k$, where k=1, 2, ... N, and is determined so that the atomic Hamiltonian of the target and projectile are diagonalized (Kuang and Lin, 1996). The parameters α and β are determined via energy minimization. The atomic states $\phi_{nlm}(\vec{r})$ are then obtained via

$$\phi_{nlm}(\vec{r}) = \sum_k c_{nk}\chi_{klm}(\vec{r}) \tag{2.25}$$

where the coefficients c_{nk} and the energies $E_{nl}(\vec{r})$ of the bound states are determined by diagonalizing the Hamiltonian. The time-dependent two-center electronic wave function is now expanded as

$$\Psi(\vec{r},t) = \sum_i a_i(t)\phi_i^A(\vec{r},t) + \sum_j b_j(t)\phi_j^B(\vec{r},t) \tag{2.26}$$

where $\phi_i^A(\vec{r},t)$ and $\phi_j^B(\vec{r},t)$ are the neutral and ion orbitals with the translational factors $a_i(t)$ and $b_j(t)$ obtained through solving the first order coupled ordinary differential equations. Inserting $\Psi(\vec{r},t)$ into the time-dependent Schrödinger equation of the collision system,

$$\Big[-\frac{1}{2}\nabla_r^2 + V_A(r_A) + V_B(r_B) - i\frac{\partial}{\partial t}\Big]\Psi(\vec{r},t) = 0 \tag{2.27}$$

where $V_A(r_A)$ and $V_B(r_B)$ are potentials representing the electron's interactions with the target and ion, the first-order coupled equations for the amplitudes centered on each of the nuclei can be solved. The transition probabilities are then found by calculating the squared moduli of the transition amplitudes at infinitely large times. The state-selective charge exchange cross-sections are then calculated by integrating the transition probabilities over

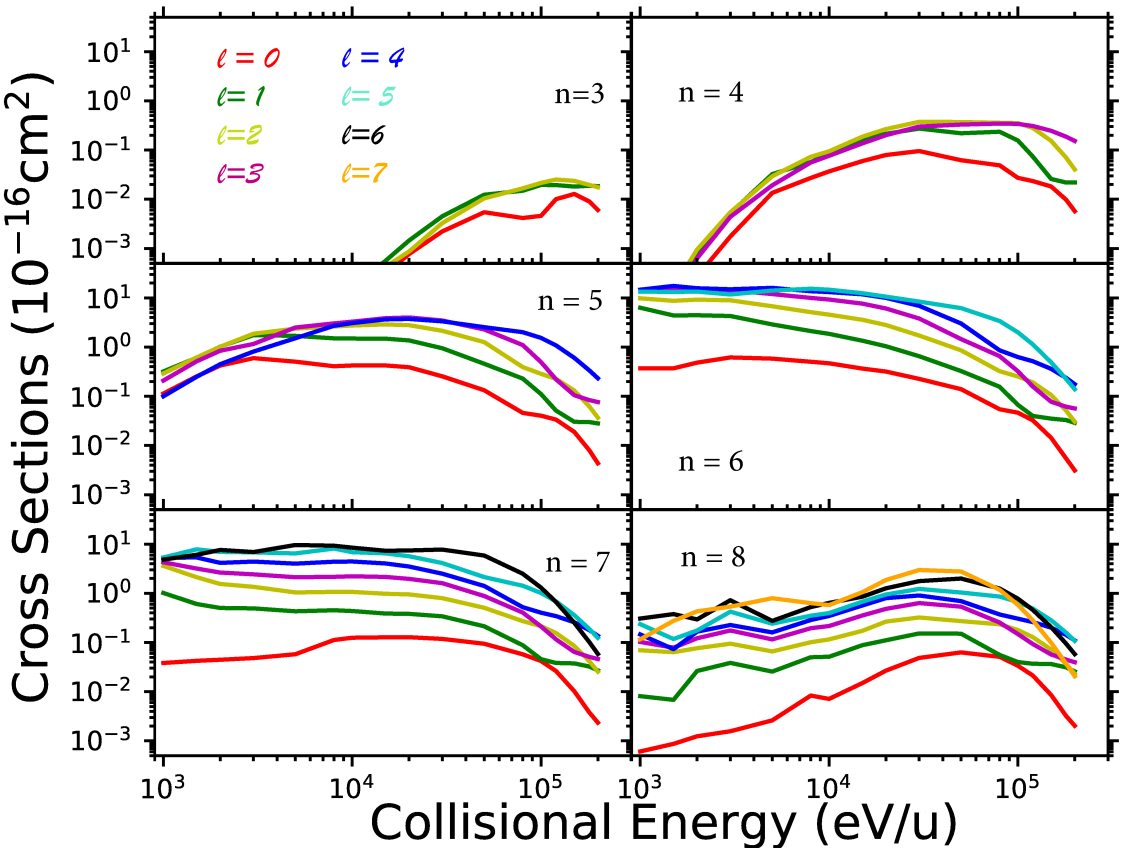

Figure 2.6: n and ℓ-resolved cross sections for the collision of Ne^{10+} with H. Cross-sections are calculated using the AOCC method (Cumbee et al., 2016a).

all impact parameters as given in Equation 2.8. We note that the AOCC method adopted here uses a one-electron effective, or independent particle model. Therefore, as it neglects two-electron interactions, it can only treat SEC processes.

A sample of CX cross-sections calculated with the AOCC method for the collision of C^{6+} with He is shown in Table 2.1. It is interesting to note that, particularly for the $4f$ and $3d$ states of this system, the cross-sections can vary greatly with increasing collision energy for this method. This is also highlighted in Figure 2.6 which shows n, ℓ-resolved cross sections for Ne^{10+} collisions with H for $n = 3$ to $n = 8$ (Cumbee et al., 2016a).

2.1.3 Classical Trajectory Monte-Carlo

For higher velocities ($\sim$ 5 keV/u to $\sim$ 10 MeV/u), we can consider the classical approach, the Classical Trajectory Monte-Carlo (CTMC) method. This method simulates collisions between ions and atoms by sampling the trajectories of initial electronic orbits with a large ensemble of configurations (microcanonical). The motion of the particles is followed by an iterative solution to Hamilton's equations. For bare ion collisions with H, Coulomb potentials are considered, but for other collisions, a model potential (Green et al., 1969) is used. After the heavy particles have interacted and moved far apart, the classical binding energies are calculated to determine if a charge exchange reaction has occurred. The final state can be determined based on the binding energy and angular momentum of the electron. Essentially, the CTMC method solves an N-body problem consisting of a projectile ion (a), target nucleus (b) and inactive target electrons, and active target electrons (c) by solving the classical Hamilton's equations,

$$\frac{\partial H}{\partial p_i} = \frac{dq_i}{dt}, \tag{2.28}$$

and

$$\frac{\partial H}{\partial q_i} = -\frac{dp_i}{dt} \tag{2.29}$$

for a large ensemble of projectile-target configurations ("trajectories") to simulate ion-atom collisions (Abrines and Percival, 1966; Olson and Salop, 1977). The classical Hamiltonian for a three-body system is given by

$$H = \frac{p_a^2}{2m_a} + \frac{p_b^2}{2m_b} + \frac{p_c^2}{2m_c} + \frac{Z_a Z_b}{r_{ab}} + \frac{Z_a Z_c}{r_{ac}} + \frac{Z_b Z_c}{r_{bc}} \tag{2.30}$$

where p_i are the momenta and $\frac{Z_i Z_f}{r_{if}}$ are the Coulomb potentials between each particle.

The trajectories sample initial electronic orbitals prepared to emulate the quantum mechanical electronic momentum distribution. At the end of the trajectory, at some asymptotic distance, relative classical binding energies between particles are computed and used to ascertain whether a reaction (charge exchange, excitation, or ionization) occurred. In the case of charge exchange to produce a hydrogen-like ion, the final $n\ell$ quantum state is determined based on the binding energy and classical angular momentum of the electron, if bound to the projectile ion, following classical-quantum binning rules (Becker and MacKellar, 1984).

Total cross sections are determined via

$$\sigma_R = \Big(\frac{N_R}{N}\Big)\pi b_{max}^2 \tag{2.31}$$

where N is the total number of trajectories run for a given maximum impact parameter b_{max}, and N_R is the number of positive tests for charge exchange reactions (Olson, 2006). The cross section has a standard deviation of

$$\Delta\sigma_r = \sigma\Big[\frac{N - N_R}{N N_R}\Big]^{\frac{1}{2}} \sim \frac{1}{N_R^{\frac{1}{2}}} \tag{2.32}$$

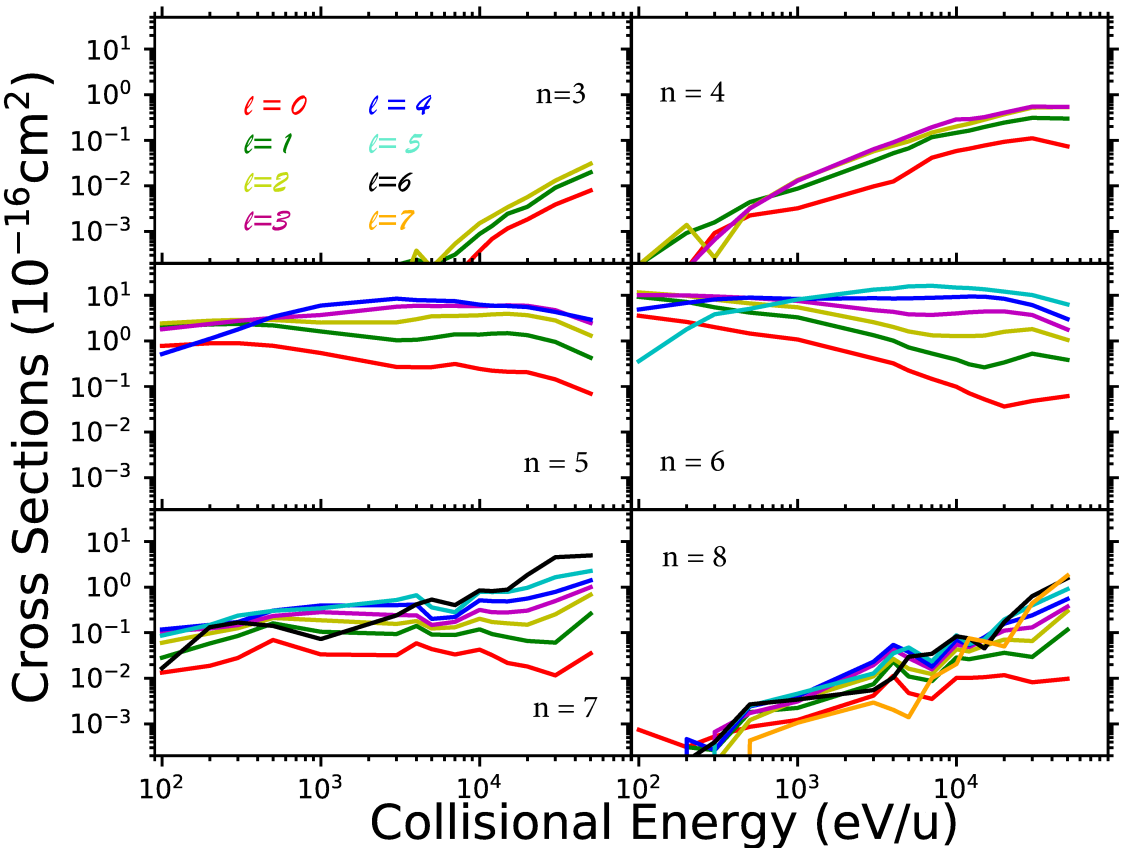

Figure 2.7: n and ℓ-resolved cross sections for the collision of Ne^{10+} with H. Cross-sections are calculated using the CTMC method (Cumbee et al., 2016a).

which means it takes considerable computation time to determine cross sections of small magnitude to a given uncertainty. To decrease the statistical error of a cross-section by a factor of two, four times as many trajectories must be evaluated.

While it might be simpler to treat each system as a one-electron model, it is necessary to use an interaction potential for more accurate calculations. Potentials derived from quantum mechanical calculations are now typically used. Garvey et al. (1975) have performed a large set of Hartree-Fock calculations, resulting in publications fitting them to the form

$$V(R) = -\frac{[Z - NS(R)]}{R} \tag{2.33}$$

where

$$S(R) = 1 - \left[\left(\frac{\eta}{\xi}\right)[\exp(\xi R) - 1] + 1\right]^{-\frac{1}{2}}. \tag{2.34}$$

where η and ξ are two fitting parameters, described in Green et al. (1969), and $\frac{\eta}{\xi}$ describes the neutral while Z is the nuclear charge. Cross-sections calculated using the CTMC method are shown in Figure 2.7 for the $n = 3$ to $n = 8$ states for Ne^{10+} CX with H. While the dominant capture channel for this collision is $n \sim 6$, the $n = 6$ and $n = 5$ states are both well populated compared to the other states for this method. In comparison, cross-sections calculated for the same collision with the AOCC method, shown in Figure 2.6, are largest for the $n = 6$ dominant capture channel as well as the $n = 7$ channel while the $n = 5$ state is relatively unpopulated.

2.1.4 Multi-Channel Landau-Zener

The Multi-Channel Landau Zener (MCLZ) method requires the least amount of numerical analysis of the four methods considered for calculating cross-sections. As a first approximation, the MCLZ method can be calculated from the lowest energies to intermediate energies

($\sim$ 5 keV/u). This method is based on a solution of the Schrödinger equation in which the electronic wave function (Ψ_{el}) can be described as a superposition of two states, giving the following diabatic first order differential equations

$$\begin{aligned} i\frac{\delta C_i}{\delta t} &= V_{if} e^{-i\int(V_i - V_f)dt} C_f \\ i\frac{\delta C_f}{\delta t} &= V_{if} e^{-i\int(V_i - V_f)dt} C_i \end{aligned} \tag{2.35}$$

where V_f is the diabatic potential energy curve corresponding to the final state f and V_{if} is the coupling element. At low energies, CX can be described by a molecular collision process involving more than one potential energy curve as shown in Fig. 2.8. In this case, the target and projectile move relative to each other along an adiabatic potential energy curve. Assuming the molecular states of the potential energy curves have the same symmetry, due to the Wigner-von Neumann non-crossing rule (Von Neumann and Wigner, 1929), the adiabatic states will never cross for any value of R. For CX to occur, a transition from one potential energy curve to another must occur. As the two curves approach closely, an avoided crossing occurs at R_c, where a rapid change occurs in the nature of the adiabatic eigenfunctions. The corresponding diabatic potential energy curves cross near R_c and are coupled by the off-diagonal elements V_{if} of a potential matrix. The reaction transition probability describes the probability that a transition occurs during a pass through R_c.

The critical parameters of the MCLZ calculation are the locations of any avoided crossings of the potential energy curves of the initial state and final states, the magnitudes of the energy separations of the avoided crossings, and the slope of the two potential energy curves at R_c.

The initial or ingoing channel is described by the interaction between the ion q_1 and neutral target species before the collision. It is characterized by two potentials. At large distances, the interaction between an atom and a charged particle is given by the polarization potential

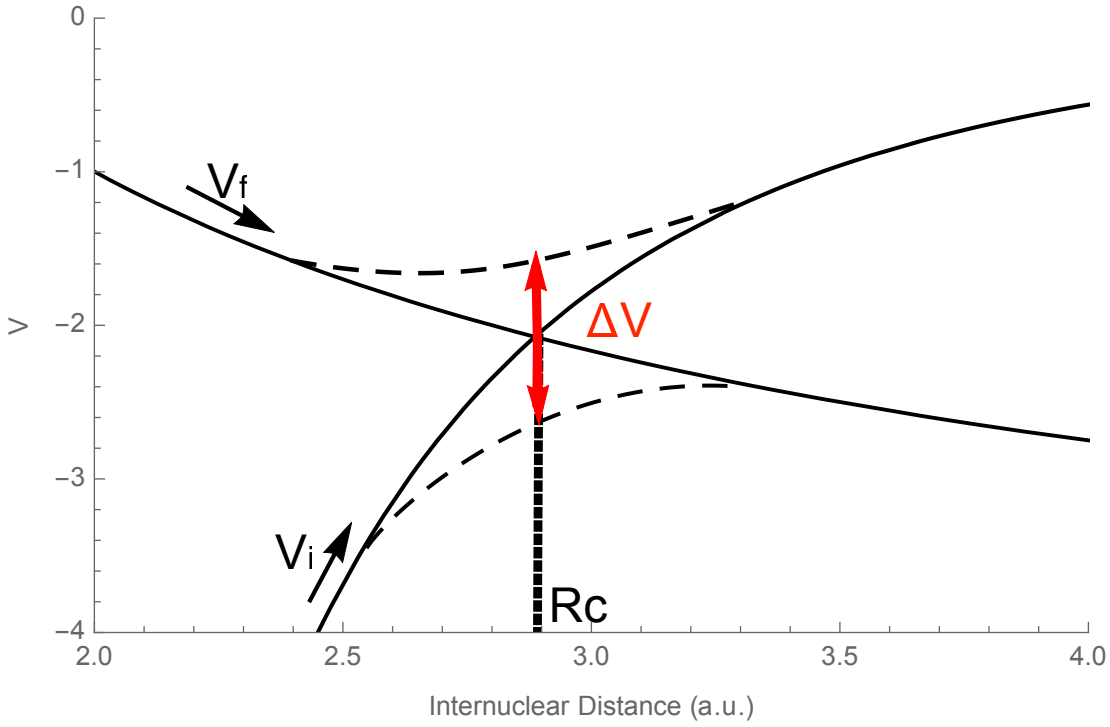

Figure 2.8: Diabatic potential energy curves for an incoming polarization potential V_i and outgoing Coulomb potential V_f showing the avoided crossing at $R = R_c$ where R is the internuclear distance. The dashed lines indicate the adiabatic potential curves.

$$V_{pol} = -\frac{\alpha q^2}{2R^4}, \tag{2.36}$$

where α is the static dipole polarizability of the neutral (= 4.5 for H). At small distance, the interaction potential is given by the repulsive Born-Mayer Potential,

$$V_{BM} = A\exp(-BR), \tag{2.37}$$

where A and B are fitting coefficients. Butler and Dalgarno (1980) determined that $A = 25q$ and $B = -0.8+\zeta_i$, where q is the initial charge state and ζ_i is the exponent for a single orbital wavefunction, with $\zeta_i = 1$ for H or $\zeta_i = 1.7$ for He. After the collision, both the projectile and the target are positively charged, so the final or outgoing channel of the interaction can be described by coulomb repulsion,

$$V_{coul} = \frac{(q_1 - 1)(q_2)}{R} - \Delta E. \tag{2.38}$$

where $q_1 = q$ (the charge of the ion) and $q_2 = 1$ for single electron capture, and V_{if}, the potential energy difference at the avoided crossing, calculated using the Olson- Salop-Taulbjerg formula (Olson and Salop, 1976; Taulbjerg, 1986), is based on an analytic fit by Olson and Salop (1976):

$$V_{if} = \left(\frac{9.13 * f_{nl}}{\sqrt{q}}\right) \exp\left(\frac{-1.324 * R_c\ a}{\sqrt{q}}\right). \tag{2.39}$$

The adiabatic curve avoided-crossing distance for a bare-ion collision (Janev et al., 1983) can be calculated via

$$R_c = \frac{n^2(Z-1)}{Z^2-n^2}\left[1 + \left[1 - \frac{3n(n-1)(Z^2-n^2)}{n^2Z(Z-1)^2}\right]^{\frac{1}{2}}\right] \simeq \frac{2n^2(Z-1)}{Z^2-n^2}, n < Z, \tag{2.40}$$

but a more generalized solution can be obtained by setting eq. (2.38) to the sum of eqs. (2.37) and (2.36) and solving for R. This form works for all ionization stages and is used in our MCLZ code, Stueckelberg (Lyons et al., 2016).

As described in Taulbjerg (1986), f_{nl}, represents a correction factor for electron capture to non-degenerate ℓ states of multi-electron ions and is given by

$$f_{nl} = (-1)^{n+\ell-1} \cdot \frac{\sqrt{2\ell+1}\Gamma(n)}{\sqrt{\Gamma(n+\ell+1)\cdot\Gamma(n-\ell)}}, \tag{2.41}$$

and $f_{nl} \to 1$ for single electron systems due to degeneracies. Thus, for bare-ion collisions, only n-resolved cross-sections can be calculated via the MCLZ method, and ℓ-distributions must be applied to n-resolved cross-sections. In order to include collisions with non-H targets, the multiplicative factor $a = \sqrt{2 \times I_t}$ is included, where I_t is the ionization potential of non-H neutral targets. After two crossings of R_c, on the way in (V_i) and out (V_f), the probability of a transition occurring is given by $2p(1-p)$. After N crossings of R_c, the probability of a transition occurring into the ionic state f is given by:

$$\begin{aligned} P_f = p_1 p_2 \cdots p_f (1-p_f)[1 + (p_{f+1}p_{f+2}\cdots p_N)^2 + \\ (p_{f+1}p_{f+2}\cdots p_{N-1})^2(1-p_N)^2 + \\ (p_{f+1}p_{f+2}\cdots p_{N-2})^2(1-p_{N-1})^2 + \\ \cdots p_{f+1}^2(1-p_{f+2})^2 + (1-p_{f+1})^2]. \end{aligned} \tag{2.42}$$

The basis of the model is formed by finding a solution to the transition probability to transfer an electron from the initial state i to the final state f. The total cross section for this transition can be found by integrating the probability over all possible impact parameters. Assuming an electron is transferred from the initial state i to the final state f at the crossing, the

MCLZ cross sections for 2-channels are calculated via

$$\sigma = 2\pi \int_0^{R_c} b\ db\ 2p\ (1-p) \tag{2.43}$$

where b is the impact parameter and p is the Landau-Zener transition probability of a single curve-crossing region given by

$$p = \exp\Big(\frac{-2\pi V_{if}^2}{\Delta F * v_{\rm rad}}\Big). \tag{2.44}$$

For more than two channels, the partial (σ_f) and total (σ) cross sections are given by

$$\sigma_f = 2\pi \int_0^{R_c} b\ db\ P_f \tag{2.45}$$

$$\sigma = \sum_{n=1}^{N} \sigma_f, \tag{2.46}$$

where P_f is given in (2.42) The radial velocity v_{rad} is a function of the impact parameter b and collision velocity ν;

$$v_{rad} = \nu\sqrt{1 - \frac{b^2}{R_c^2} - \frac{V}{E}} \tag{2.47}$$

and ΔF is the difference in the slopes of the diabatic potential energy curves at the avoided crossing distance R_c as shown in Fig 2.8.

For bare ions, only the n-distribution is calculated, but it is also necessary to know the ℓ-distribution for each n-level. Janev et al. (1983) suggested that the ℓ-distribution can be determined by multiplying an n-resolved MCLZ cross-section by a distribution function W_{nl}. For energies greater than $\sim$1 keV/u the ℓ-levels are found to be populated statistically,

$$W_{nl}^{stat} = \frac{(2\ell+1)}{n^2} \tag{2.48}$$

via the statistical ℓ-distribution with a maximum given by $\ell = n-1$. For energies lower than $\sim$1 keV/u, Abramov et al. (1978) derived a low-energy distribution function,

$$W_{nl}^{lowe} = (2\ell+1)\frac{[(n-1)!]^2}{(n+\ell)!(n-1-\ell)!}, \tag{2.49}$$

which has a maximum at $\ell = 1$ for n < 8, but it shifts to larger ℓ for n> 8.

As the MCLZ method is only capable of producing n-resolved cross sections for bare ions such as Ne^{10+}, an ℓ-distribution must be applied. n,ℓ-resolved cross sections for Ne^{10+} collisions with H are shown in Figure 2.9 using the low-energy ℓ-distribution and Figure 2.10 for the statistical ℓ-distribution for the $n = 3$ to $n = 7$ states. The ℓ-resolved cross-sections are shown in various colors. For the two ℓ-distributions, the shape of the cross-section curves stays constant while the the contribution from the various ℓ-levels varies. For the $n = 6$ channel, the $\ell = 1$ (p-state) is dominant for the low-energy ℓ-distribution, while the $\ell = 4$ and 5 states dominate for the statistical distribution.

As the four methods considered are relevant at different collision energies, it can be useful to compare available methods to produce recommended cross sections for various energies. Figure 2.11 compares cross-sections for Ne^{10+} CX with H for the dominant capture channel of $n = 6$ for the AOCC, CTMC, and MCLZ methods to provide a set of recommended cross-sections. To illustrate the importance of the kinetic energy variation, a set of X-ray emission spectra are calculated with the recommended cross sections for O^{8+} with H (Janev et al., 1993) as shown in Figure 2.12. The intensity of the Ly β and higher lines decrease with energy for this collision system. Similar results will be shown for Ne^{10+} in the next section.

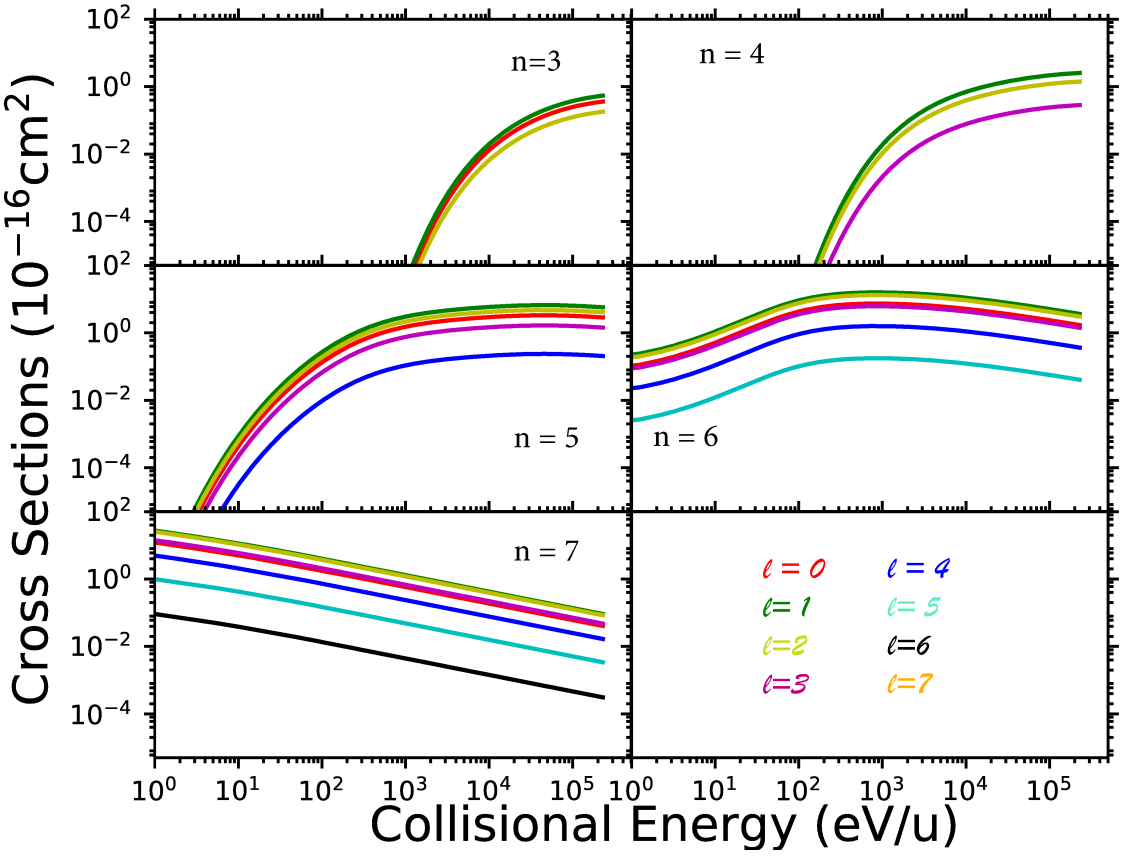

Figure 2.9: n and ℓ-resolved cross sections for the collision of Ne^{10+} with H. Cross-sections are calculated using the MCLZ low-energy ℓ-distribution (Cumbee et al., 2016a).

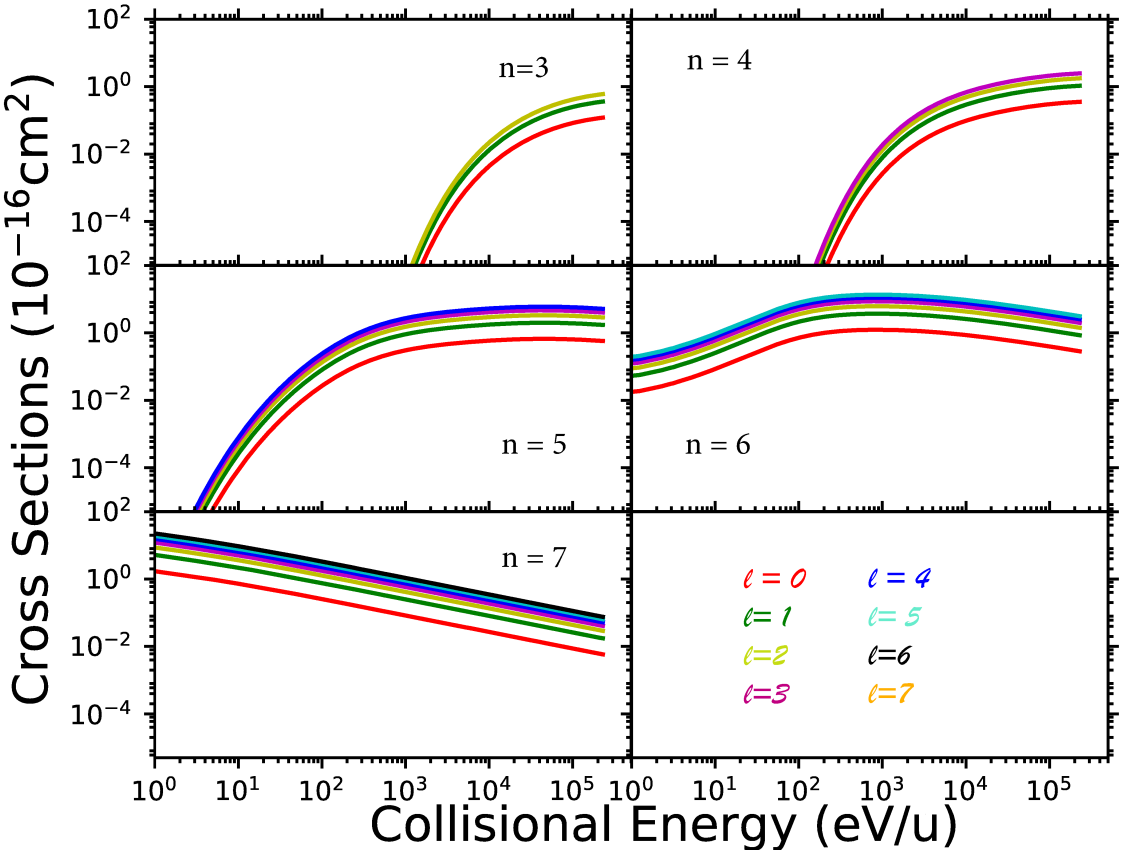

Figure 2.10: n and ℓ-resolved cross sections for the collision of Ne^{10+} with H. Cross-sections are calculated using the MCLZ statistical ℓ-distribution (Cumbee et al., 2016a).

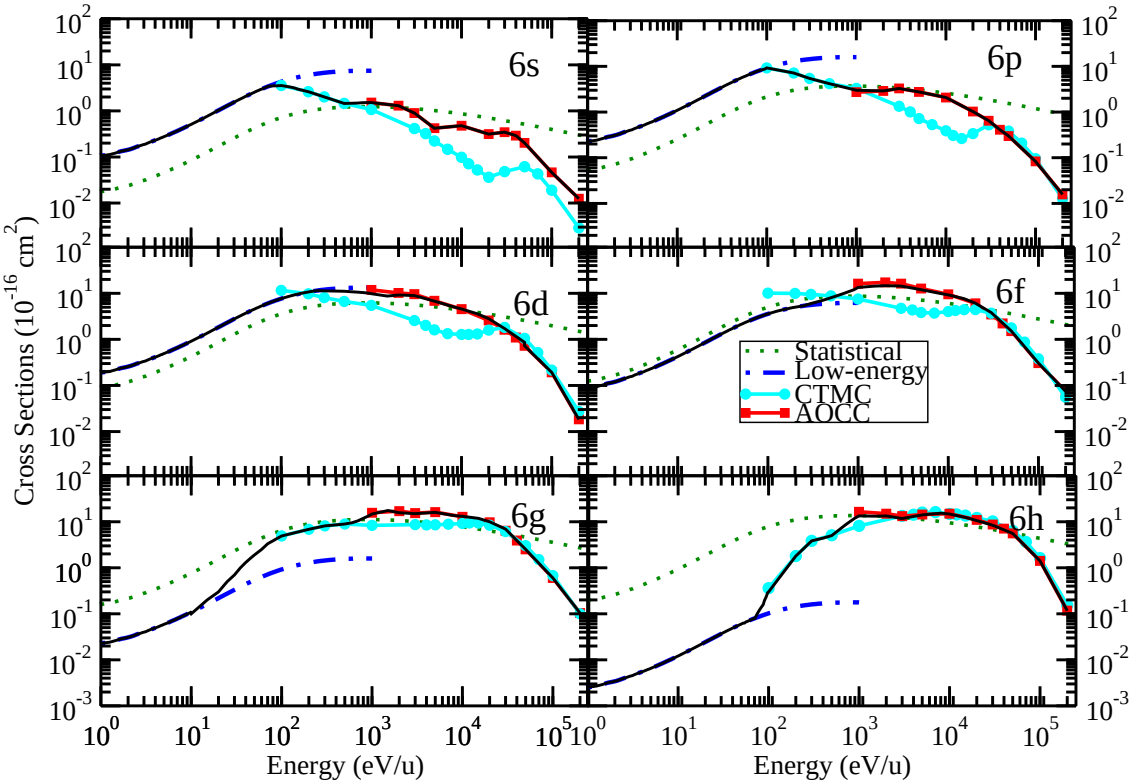

Figure 2.11: New charge exchange cross sections for the collision of Ne^{10+} with H as a function of collisional energy for the dominant capture channel of n=6. The blue (-..) lines represent the MCLZ low energy distribution, the green dotted (...) lines represent the MCLZ statistical distribution, the cyan lines with filled circles represent the CTMC method, and the red lines with squares represent the AOCC method. The solid black line shows our suggested cross sections.

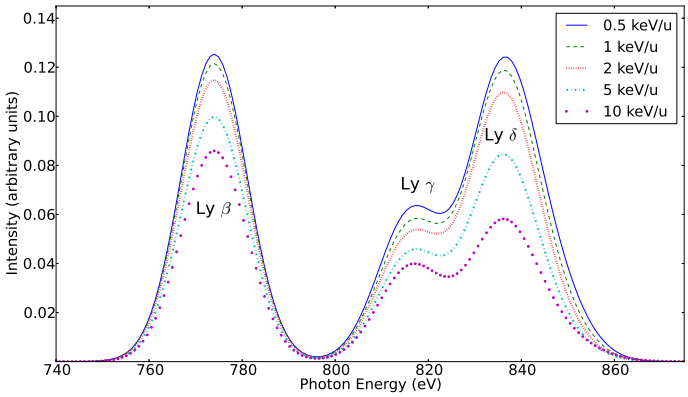

Figure 2.12: X-ray emission spectrum including Lyβ and higher lines for the collision of fully ionized O with neutral H for a collisional energy of 0.5, 1, 2, 5, and 10 keV/u (309, 438, 619, 979, and 1384 km/s, respectively). The lines are convolved with a FWHM of 10 eV. For each collisional energy, the Lyβ and higher lines are normalized to the Lyα line. Cross sections are from Janev et al. (1993).
.

2.2 Charge Exchange X-ray Emission Spectra

In order to predict CX-induced spectra, a low density, steady-state radiative cascade model was applied as described by Rigazio et al. (2002). In this model, the initial state populations are proportional to the quantum-state-resolved CX cross sections. As the electron cascades down to the lowest energy level, obeying quantum mechanical selection rules, photons are emitted, including X-rays.

A spectrum and schematic Grotrian diagram are shown in Figure 2.2 following the collision of C^{6+} with H. In this case, the electrons are captured into the n=2, 3, and 4 capture channels of the C^{5+} ion. The schematic Grotrian Diagram represents the transitions that occur after an electron is captured into various n, ℓ states. The colored lines represent the transitions that result in the Lyα, Lyβ, and Lyγ lines in the C^{5+} spectrum. Given an initial n, ℓ-distribution, it is possible to calculate an exact representation of the resulting spec-

trum (Kharchenko and Dalgarno, 2000). The number of photons that are emitted by an ion that makes the transition from $n\ell \rightarrow n'\ell'$ are calculated by taking into account all possible transitions that might occur. Equations (2.50)-(2.52) show the emission cross sections (proportional to the relative line intensities) for producing the Lyα, Lyβ, and Lyγ X-ray emission lines (Fogle et al., 2014).

$$P(Ly\alpha) = \sigma_{2,1} + \sigma_{3,0} + \sigma_{3,2} + \sigma_{4,0}\frac{A_{4,0\rightarrow 2,1}}{\sum A_{4,0}} + \sigma_{4,1}\frac{A_{4,1\rightarrow 3,0} + A_{4,1\rightarrow 3,2}}{\sum A_{4,1}} + \sigma_{4,2}\frac{A_{4,2\rightarrow 2,1}}{\sum A_{4,2}} + \sigma_{4,3} \tag{2.50}$$

$$P(Ly\beta) = \sigma_{3,1}\frac{A_{3,1\rightarrow 1,0}}{\sum A_{3,1}} + \sigma_{4,0}\frac{A_{4,0\rightarrow 3,1}}{\sum A_{4,0}}\frac{A_{3,1\rightarrow 1,0}}{\sum A_{3,1}} + \sigma_{4,2}\frac{A_{4,2\rightarrow 3,1}}{\sum A_{4,2}}\frac{A_{3,1\rightarrow 1,0}}{\sum A_{3,1}} \tag{2.51}$$

$$P(Ly\gamma) = \sigma_{4,1}\frac{A_{4,1\rightarrow 1,0}}{\sum A_{4,1}} \tag{2.52}$$

Here, $\sigma_{n,l}$ is the cross section that results from an electron captured in the n- and ℓ- state, assuming that capture only to the $n = 2 - 4$ states is possible. The transition probabilities (or Einstein A-coefficients) from state n, ℓ to n', ℓ' are given by $A_{n\ell\rightarrow n'\ell'}$, and the transition probabilities for all paths from a given n, ℓ state are given by $\sum A_{n\ell}$. In equation (2.50), the $2p$ state always transitions into the $1s$ state resulting in the Lyα line while other states such as the $4s$ state only sometimes transition into the $2p$ state, the contribution of which is determined by the $\frac{A_{n,l\rightarrow 2,1}}{\sum A_{n,\ell}}$ term. The same is true for Equations (2.51) and (2.52). These emission cross sections are proportional to the relative line ratios, shown in Figure 2.13 for the collision of Ne^{10+} with He. These line ratios can then be compared to observational line ratios or convolved with a gaussian function in order to mimic observational and experimental spectra.

When the initial charge q of the ion X^{q+} is greater than $\sim$3, the electron will be primarily captured into an excited state that decays to a lower state, such as the ground state, and

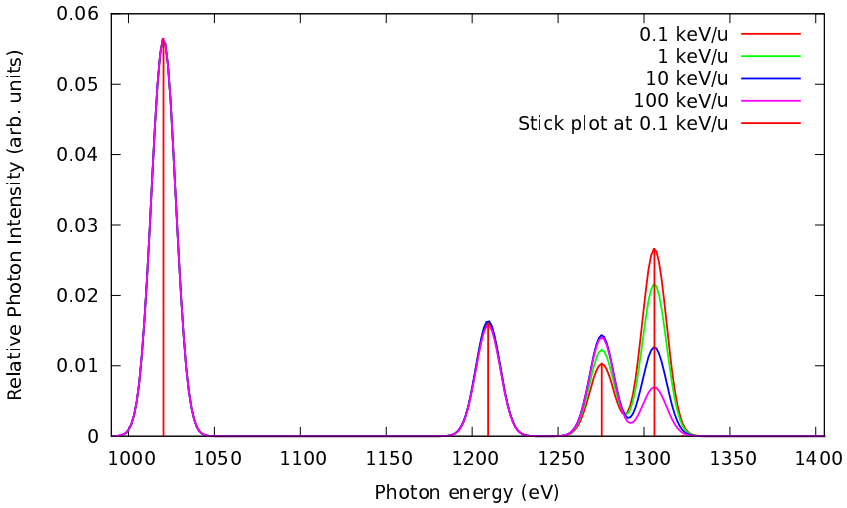

Figure 2.13: X-ray spectra using MCLZ cross sections with the low energy ℓ-distribution are shown for the collisions of Ne^{10+} with He for collisional energies of 0.1 to 100 keV/u. Lines are normalized to Lyα at 1020 eV. The stick plot is produced directly from the Cascade model, and the line ratios are convolved with a 10 eV FWHM Gaussian to produce the spectra shown.

emits at least one photon. In the case of Ne^{10+}+H, shown in Figure 2.14, that produces the hydrogen-like ion Ne^{9+} primarily in the principal quantum level $n = 6$ (see, for example, Krasnopolsky et al., 2004; Smith et al., 2014), the electron can be captured to any orbital angular momentum state from $\ell = 0$ ($6s$) to $\ell = 5$ ($6h$) with a range of probabilities. In the case that the electron is captured to the $6p$ state of Ne^{9+}, it will primarily decay to the $1s$ ground state emitting a 1322 eV X-ray photon, the Lyϵ line. In another case in which the electron is captured to the $6h$ state, it can only decay by a series of $\Delta\ell = \Delta n = -1$ Yrast transitions that result in infrared and visible photons. When the electron arrives at the $2p$ level, it will decay to the ground state emitting the 1020 eV Lyα line. Lyβ, Lyγ, and Lyδ lines will also be produced from the cascade resulting from capture to other 6ℓ states. While $n = 6$ is the dominant manifold for electron capture with H, there are also

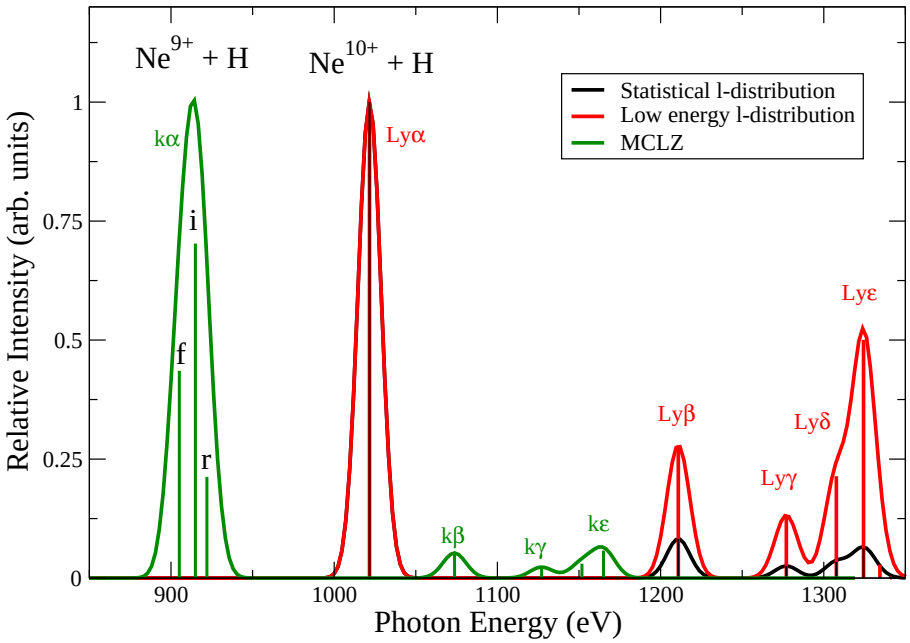

Figure 2.14: X-ray emission spectra for the collisions of Ne^{9+} and Ne^{10+} with H. MCLZ cross-sections are used for both collision systems, and for Ne^{10+} the low-energy and statistical ℓ-distributions are both shown. The line ratios are convolved with a 10 eV FWHM Gaussian to produce the spectra shown.

Table 2.2: X-ray line ratios for H-like C^{6+} CX with H

Photon Energy (eV)	Line	Normalization
367.49	Ly α	1.0000
435.55	Ly β	0.1478
459.37	Ly γ	0.2286
470.39	Ly δ	0.0140
476.38	Ly ϵ	0.0012
H -Ratio		0. 3916

Collision Energy = 1000.0 eV/u (437.5 km/s). Cross sections are from Janev et al. (1993).

significant probabilities for capture to $n = 7$ and $n = 5$ followed by cascade and X-ray emission. Therefore, to fully predict the X-ray spectrum of Ne^{9+} following CX collisions with H, or similarly with He, requires knowledge of many $n\ell$-resolved cross sections.

2.2.1 Line Ratios

A sample of line ratios calculated with the Cascade model for a H-like case is shown in Table 2.2. For the CX collision of C^{6+} with H, the Lyman series transitions are shown, from the Lyα line to the Lyϵ line. The spectrum, convolved with a Gaussian FWHM of 10 eV is shown in Figure 2.2. The Ly $\delta+$ lines are very small compared to the Lyα line for this collision, and are thus not visible in this spectrum. Throughout this dissertation, all lines will be normalized to the Lyα line . The relative intensities of the Lyβ and higher lines vary with the choice of collision energy, method for calculating cross-sections, and the neutral target. Table 2.3 provides an example of the X-ray line ratios resulting from a He-like ion collision. In this case, both singlet (^1L) and triplet (^3L) states are populated. All lines are then tied to the Kα resonant ($2p\ ^1P \rightarrow 1s\ ^1S$) line. The ratio of the Kα intercombination

Table 2.3: X-ray line ratios for H-like C^{5+} CX with He

Photon Energy (eV)	Line	Normalization
298.96	K α f	2.5890
304.41	K α i	0.2100
307.90	K α r	1.0000
354.52	K β	0.6122
	H$'$ -Ratio	0.6122
	H-Ratio	0.1611
	G -Ratio	2.799

Collision Energy = 200 eV/u (195.7 km/s). Cross-sections calculated with MCLZ method.

($2p\ ^3P \rightarrow 1s\ ^1S$) and K$\alpha$ forbidden ($2s\ ^3S \rightarrow 1s\ ^1S$) lines to the K$\alpha$ resonant line, or G-ratio, is important for identifying the source of the X-ray emisison (Liu et al., 2011). For electron collisional excitation, the ratio is dominated by the resonant line, while for CX the forbidden line dominates (Liu et al., 2012). Figure 2.14 compares the spectra resulting from CX collisions of H-like Ne^{10+} and He-like Ne^{9+} with H, with the Kα triplet labeled. In this case, the forbidden and intercombination lines are much larger than the resonant line. With these high resolution theoretical spectra (10 eV Gaussian FWHM), none of the H-like and He-like lines overlap, which is often not the case in astrophysical observations. Figure 2.15 shows an example of a He-like triplet for the collision of O^{7+} with H. In this case, the G-ratio is 2.047. For CX collisions, as shown in these spectra, the forbidden and intercombination lines are strong when compared to the resonant line.

The ratio of the intensity of the Lyβ and higher lines to the Lyα line is quite interesting as it will also vary for different processes and for different collision energies. These ratios can give insight into what processes may be occurring within astrophysical environments, including, but not limited to, extracting the collisional energies and ion abundance ratios.

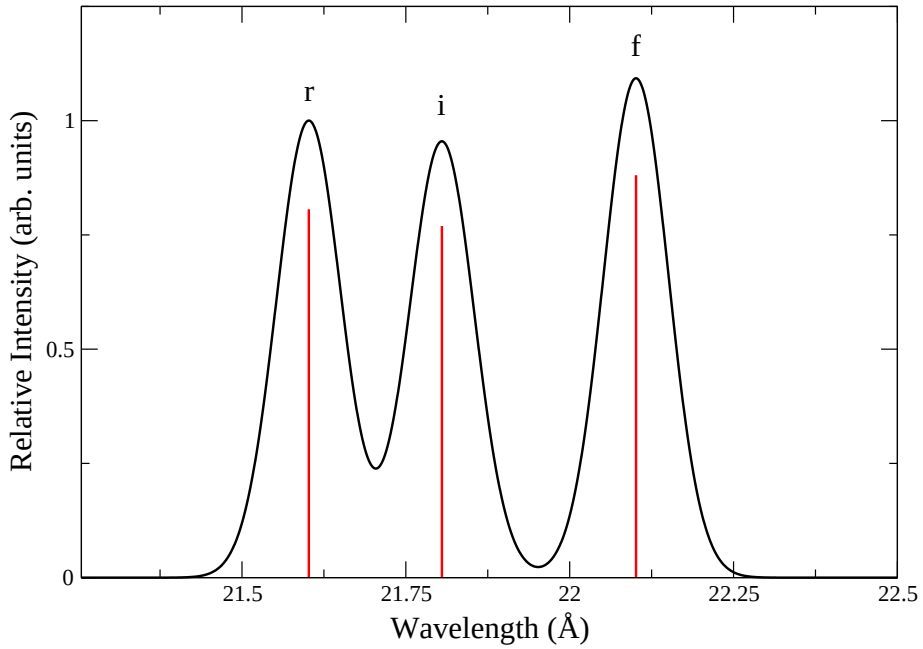

Figure 2.15: Kα triplet for the CX collision of O^{7+} with H for a collision energy of 1 keV/u and a Gaussian FWHM of 0.07 Å. The G-ratio $\left(\frac{I_f+I_i}{I_r}\right)$ for this collision energy is 2.047. QMOCC cross-sections are used (Nolte, 2016).

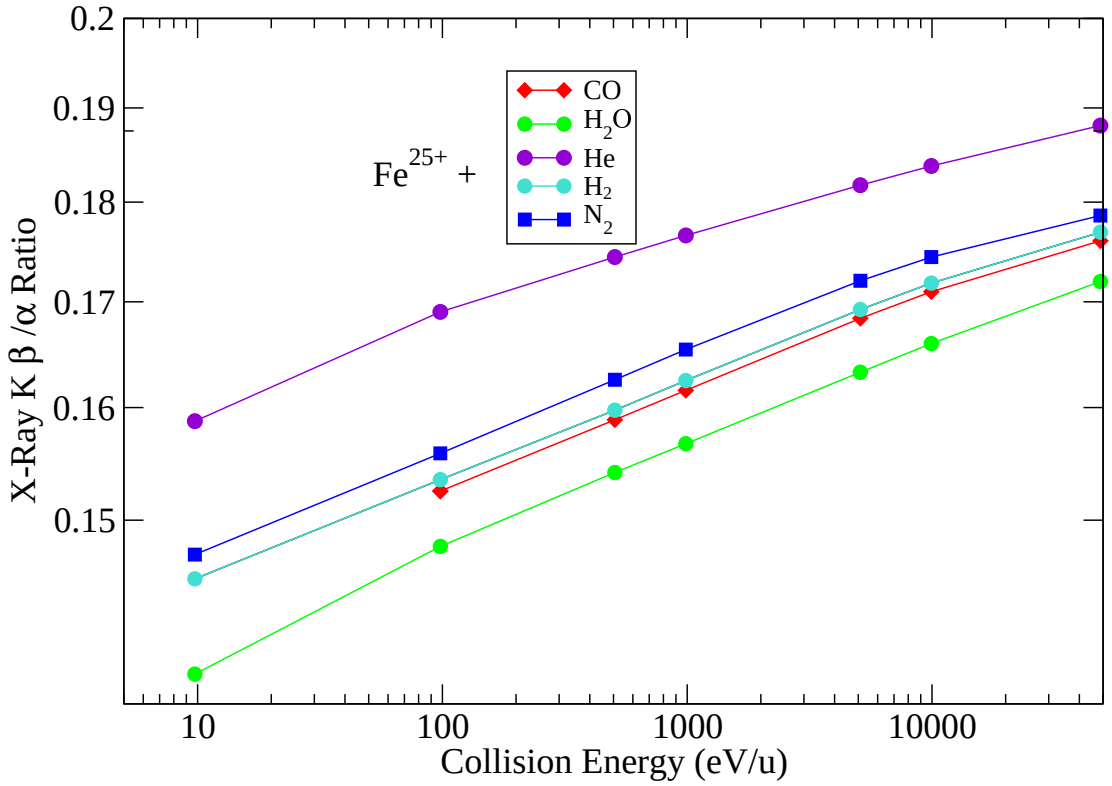

Figure 2.16: Kβ to Kα line ratios for Fe^{25+} collisions with CO, H_2O, He, H_2, and N_2. MCLZ cross-sections are used here.

Figure 2.16 shows the collisional energy dependence of the Kβ/Kα ratio for Fe^{25+} for various neutral targets. The ratio varies for each target, but generally increases with collision energy. The starburst galaxy M82 will be discussed in detail in §3.4, but Figures 3.14-3.15 show the ratios of Lyβ/Lyα calculated over different collisional energies using the four different methods described in §2.1. By comparing the theoretical line ratios to the observed line ratios, it is possible to determine the contribution of CX in the observed spectrum.

2.2.2 Results and Comparisons: Ne^{10+}

Here we compare CX X-ray emission due to Ne^{10+} collisions with H and He using three theoretical methods. In the case of He, X-ray spectra are compared to a previous experiment that used a coincident X-ray - ion charge state and momentum detection approach that allowed determination of the charge exchange product state. Computed Lyman series line ratios are compared to the Ne X Lyβ/Lyα ratio in the disk of M82 and are found to be consistent with a CX interpretation.

Cross sections for Ne^{10+} with H and He for capture to state-resolved $Ne^{9+}(n\ell\ ^2L)$ levels have been calculated using the CTMC, AOCC, and MCLZ methods. While both collision systems have been studied for many decades (e.g., Schultz and Krstic, 1995; Liu et al., 2014), none of the previous studies have presented a comprehensive set of state-resolved cross sections over a range of energies relevant to astrophysics. The Ne^{10+}+ H CX cross sections discussed here are shown in Figure 2.11 for the dominant capture channel of $n = 6$. Details of the MCLZ cross section calculations used here are summarized in §2.1.4 and Lyons et al. (2016).

Spectra were obtained for Ne^{10+} CX collisions with H and He for a range of kinetic energies. For Ne^{10+}+H CX, cross sections from the AOCC, CTMC, and MCLZ methods are adopted. For the MCLZ method, calculations were performed using the low energy and statistical ℓ-distributions described in equations (2.48) and (2.49) (see also Janev et al., 1983; Krasnopolsky et al., 2004; Smith et al., 2014). Calculations for Ne^{10+} + He CX were performed using only the MCLZ method here, with both the low energy and statistical ℓ-distributions as with H. Nevertheless, the present (and previously published) AOCC and CTMC data for Ne^{10+}+ H CX, applicable primarily at higher impact energies than of astrophysical relevance in nebular environments, are instructive for comparison with MCLZ calculations in order to assess their reasonableness in the range of energies where they have overlapping applicability with CTMC and AOCC. We note below the existence of CTMC

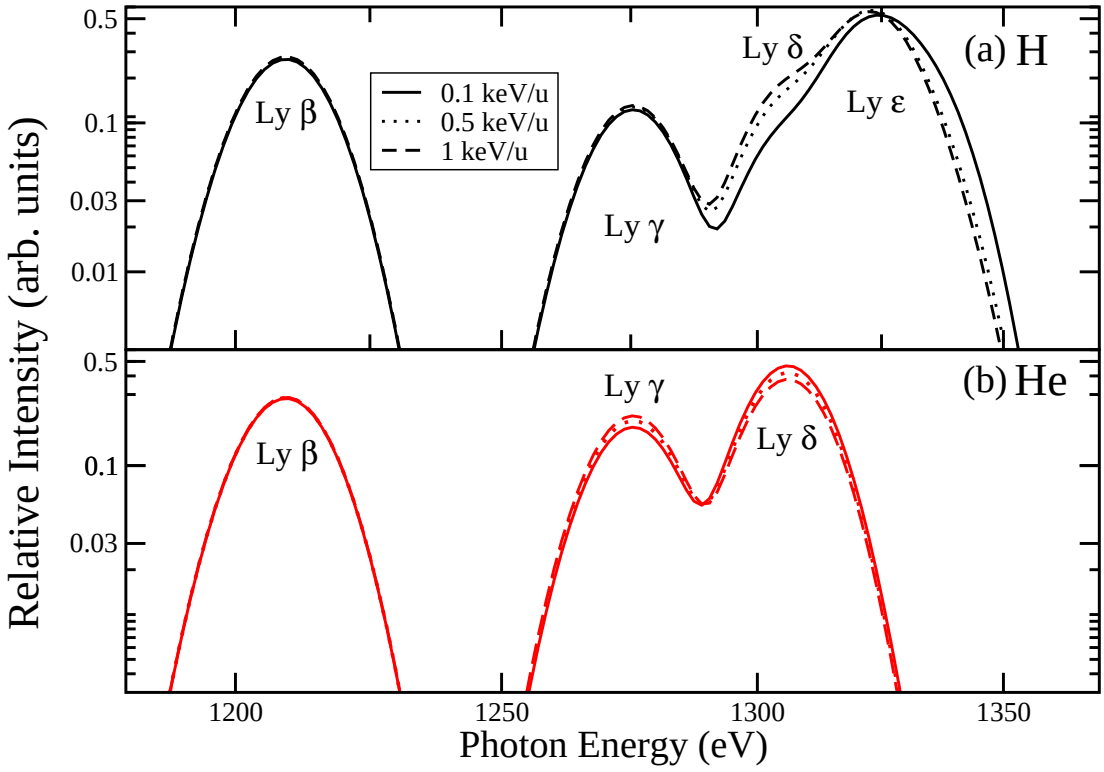

Figure 2.17: X-ray spectra using the MCLZ cross sections with the low energy ℓ-distribution are shown for the collisions of Ne^{10+} with H (top panel) and He (bottom panel) at collisional energies of 0.1, 0.5 and 1 keV/u. Lines are normalized to Lyα at 1020 eV with a resolution of 10 eV FWHM.

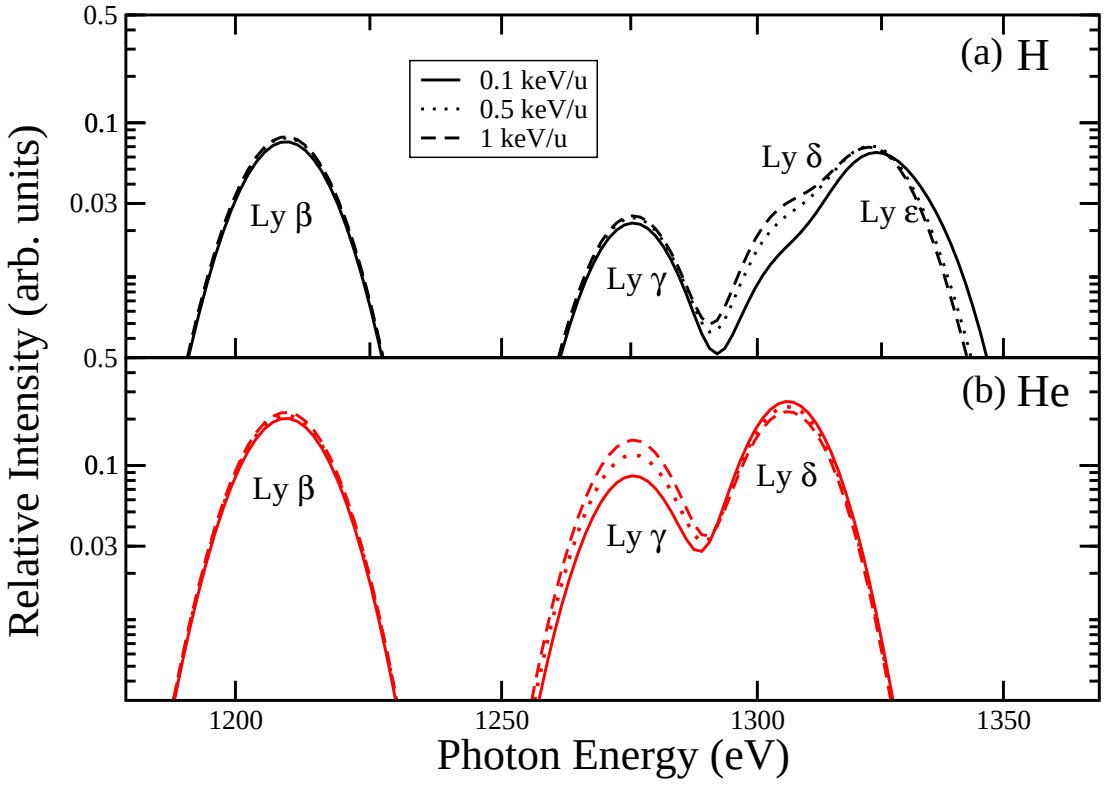

Figure 2.18: X-ray spectra using the MCLZ cross sections with the statistical ℓ-distribution are shown for the collisions of Ne^{10+} with H (top panel) and He (bottom panel) at collisional energies of 0.1, 0.5 and 1 keV/u. Lines are normalized to Lyα at 1020 eV with a resolution of 10 eV FWHM.

data for Ne^{10+}+ He CX presented previously in Ali et al. (2010).

Among the theoretical methods for the energy range and ion-atom systems considered here, at lower energies, the MCLZ low energy ℓ-distribution is expected to describe the CX mechanism most accurately. Spectra are shown in Figure 2.17 for Ne^{10+} CX with H and He at collisional energies of 0.1, 0.5, and 1 keV/u using this method. For Ne^{10+} CX with H, as the collisional energy increases, the relative intensities of the Lyβ and higher lines show a slight increase. For Ne^{10+} CX with He, the trend is similar for the Lyγ line, but reverses for the Lyδ line. The variation, however, is small. Further, the Lyϵ line is practically missing for Ne^{10+}+ He as the dominant n capture channel for CX with He is typically one smaller than for CX with H. Figure 2.18 shows a similar spectra using the MCLZ statistical distribution. The trends are the same for CX with both H and He, however, for He, the higher Lyman lines have significantly smaller intensities giving a softer total X-ray spectrum. The statistical distribution is likely not valid at this low collision energy. Figures 2.19-2.20 show the CTMC, AOCC, and MCLZ low energy and statistical ℓ-distribution spectra for 1-20 keV/u. The most notable difference in comparison to the MCLZ results using the low-energy ℓ-distribution is the decrease in the Lyϵ line for all methods.

At higher energies (above ∼1-10 keV/u,) the statistical ℓ-distribution is expected to be more realistic in describing CX emission than the low energy ℓ-distribution. Figure 2.21 shows the CX emission for Ne^{10+}CX with He measured using simultaneous cold-target recoil ion momentum spectroscopy and X-ray spectroscopy as described in Ali et al. (2010) at 4.55 keV/u. The experimental single electron capture (SEC) CX emission is compared to spectra obtained with the CTMC (Ali et al., 2005) and AOCC (Liu et al., 2014) methods at the same energy, and the MCLZ low energy and statistical ℓ-distributions at 4.8 keV/u. Both MCLZ methods provide a better fit to the experimental data than the CTMC or AOCC methods at this energy. The MCLZ statistical ℓ-distribution results in slightly smaller Lyβ and higher lines, while the MCLZ low-energy ℓ-distribution results in slightly larger Lyβ

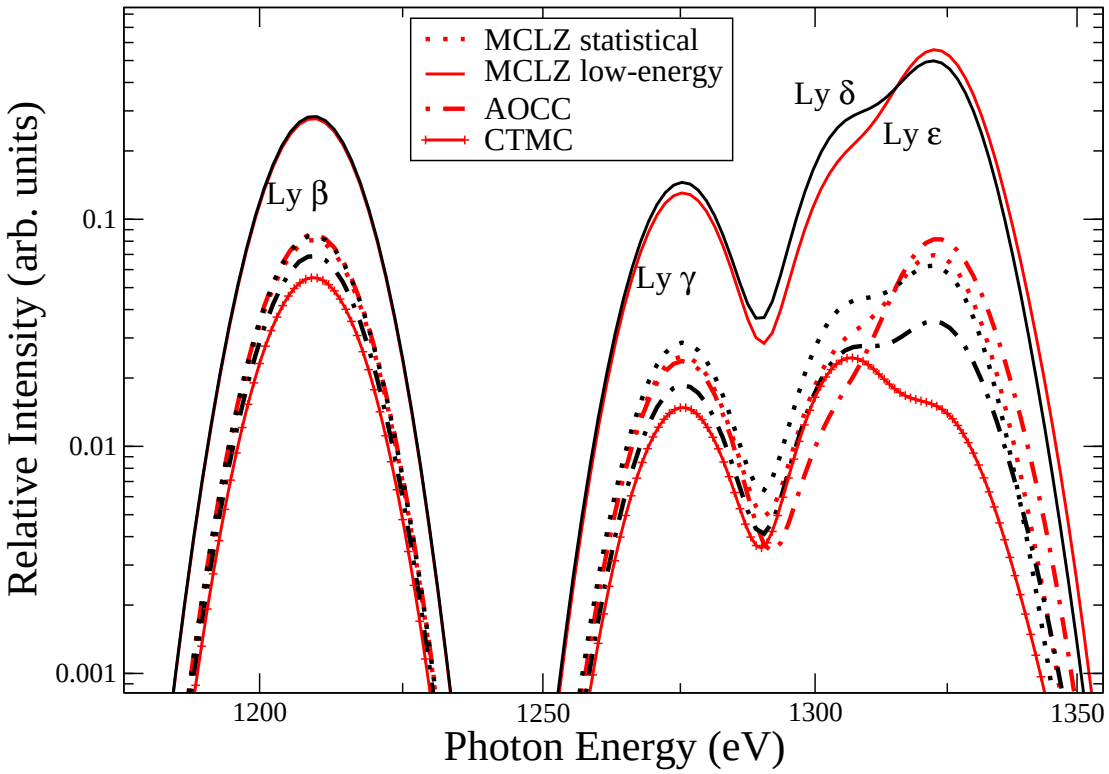

Figure 2.19: Ne^{10+} + H X-ray spectra calculated using the AOCC and CTMC cross sections are compared to the MCLZ method at collisional energies of 1 keV/u (black lines) and 5 keV/u (red lines). Lines are normalized to Lyα at 1020 eV with a resolution of 10 eV FWHM.

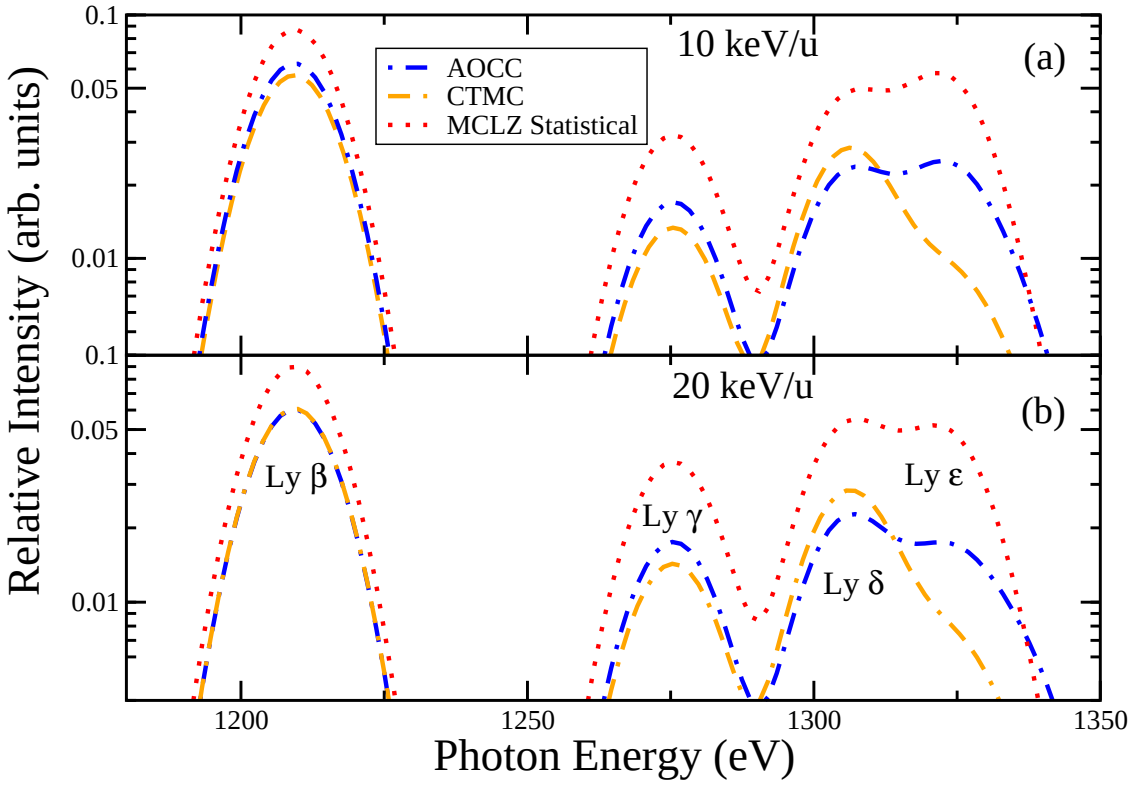

Figure 2.20: The CTMC method is compared to the AOCC and MCLZ statistical ℓ-distribution methods for the collision of Ne^{10+} with H at an energy of 10 keV/u (top panel) and 20 keV/u (bottom panel). Lines are normalized to Lyα at 1020 eV with a resolution of 10 eV FWHM.

and higher lines. At this resolution, the Lyβ and Lyγ lines are not clearly resolved in the theoretical spectra.

In addition to SEC, observed and experimental X-ray emission spectra often contain contributions from multiple electron capture (MEC), including double capture with subsequent autoionization (DCAI) and transfer ionization (TI). Emission from states populated by a combination of these reaction channels may be present in astrophysical spectra. Figure 2.3 shows a comparison of DCAI to SEC for Ne^{10+} CX with He using the CTMC method (Ali et al., 2005). While TI has an insignificant contribution in the present ion-atom systems at low collision energy, DCAI is shown to give a contribution of 21% of the total spectrum for the CTMC method. However, Table 1 in Ali et al. (2005) shows that the experiment suggests a smaller 12% fraction of MEC, which agrees with the MCLZ method from that work. This small fraction of MEC to the total CX emission suggests that ignoring MEC in Ne^{10+} CX in an observed spectrum and assuming that SEC is dominant is justifiable when considering He as the CX target, though exceptions for other ions are possible.

2.2.3 Results and Comparisons: Fe^{25+} and Fe^{26+}

MCLZ calculations were performed for the collisions of Fe^{25+} and Fe^{26+} with N_2 at $\sim$ 1 eV/u to 100 eV/u to compare to laboratory EBIT measurements performed by Wargelin et al. (2005). In their paper, Wargelin et al. (2005) were able to obtain two sets of experimental spectra; for Fe^{25+} colliding with N_2, and for Fe^{25+} and Fe^{26+} both colliding with N_2. The two measurements were performed using different electron beam energies. The first measurement was at 9.2 keV, in which most of the ions were Fe^{25+}, and the second was at 17.2 keV, which had a roughly 2:1 fraction of Fe^{25+} to Fe^{26+} ions. For both experiments, the estimated average ion energy, or the collision energy, is $\sim$10 eV/u.

Figures 2.22-2.24 compare the laboratory EBIT measurements to theoretical spectra produced using MCLZ cross-sections. For the collision of Fe^{25+} with N_2 (Figure 2.22), MCLZ

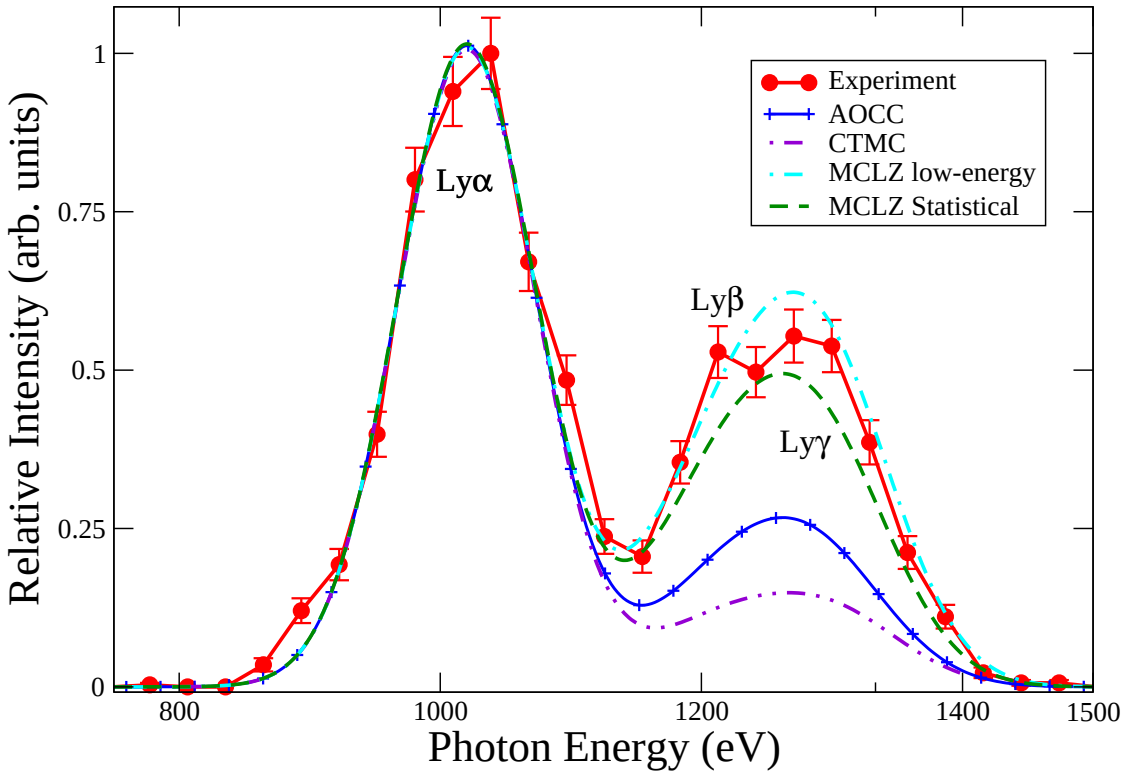

Figure 2.21: Experimental single electron capture (SEC) data for Ne^{10+} CX with He at $\sim$ 4.5 keV/u is compared to CTMC, AOCC (Liu et al., 2014), and MCLZ low-energy and statistical distributions for SEC. A resolution of 75 eV FWHM is used for the theoretical methods compared to a resolution of 68 eV for the experimental data (Ali et al., 2010). Note that the experimental spectra includes no multi-electron capture events.

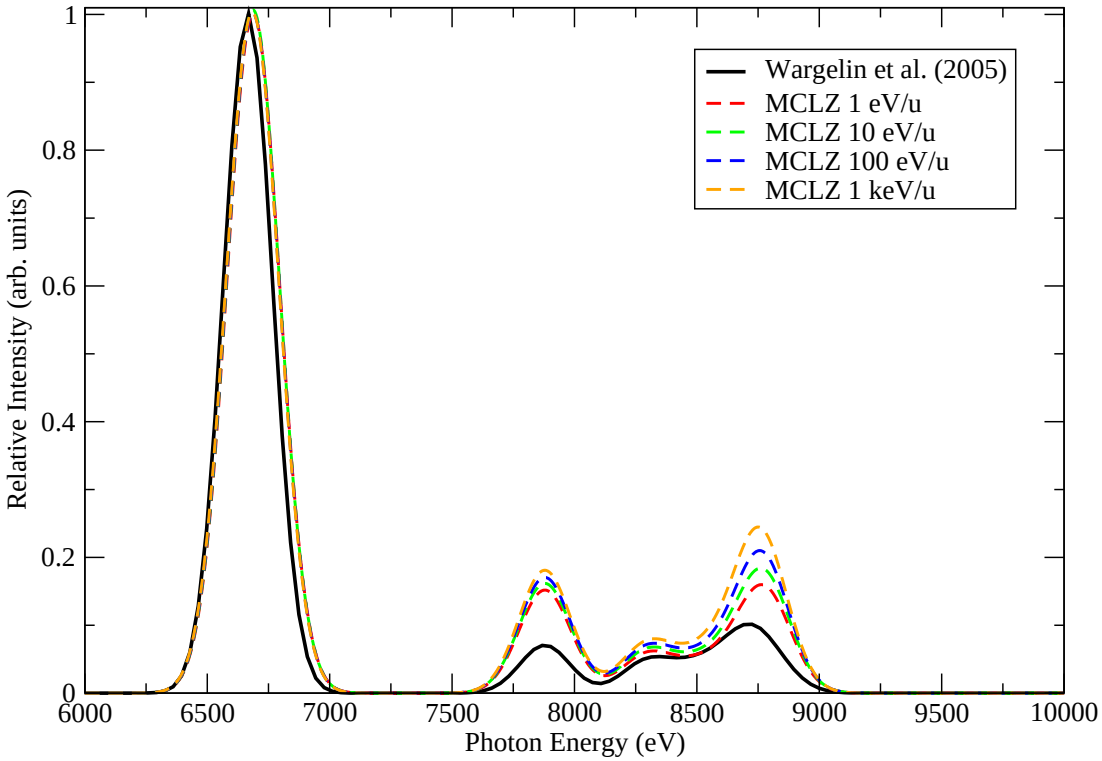

Figure 2.22: Experimental EBIT measurements for Fe^{25+} CX with N_2 (Wargelin et al., 2005) are compared to theoretical spectra using MCLZ cross sections.

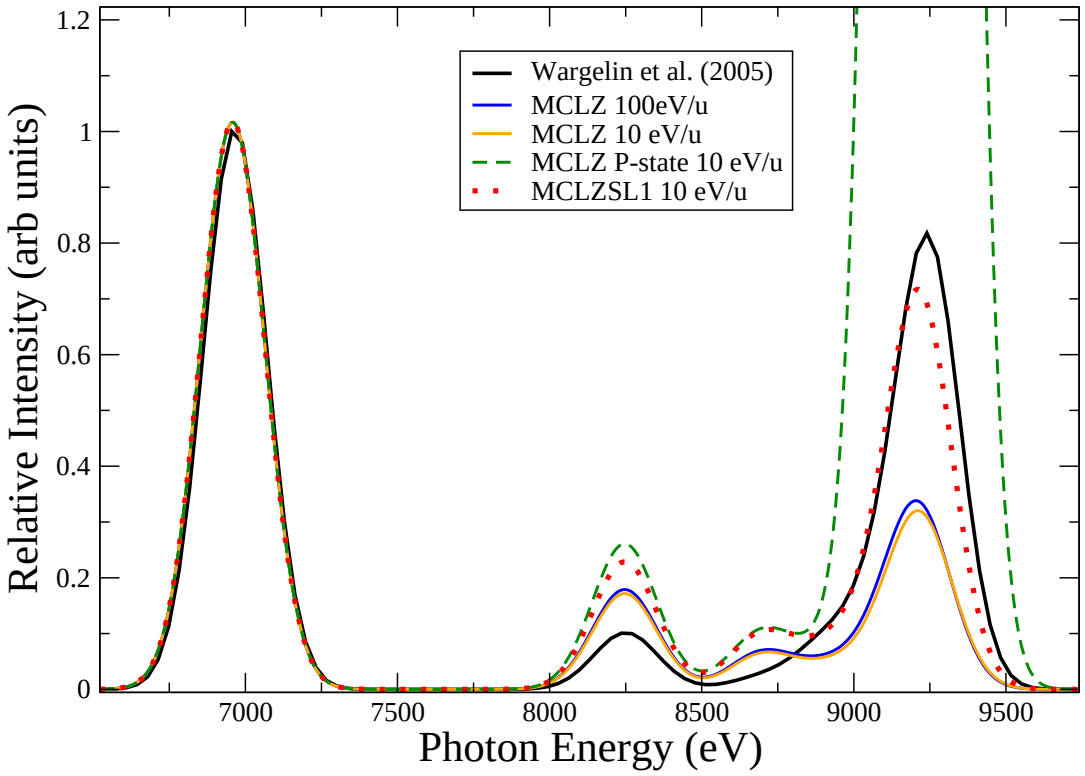

Figure 2.23: Experimental EBIT measurements for Fe^{26+} CX with N_2 (Wargelin et al., 2005) are compared to theoretical spectra using MCLZ low-energy ℓ-distribution cross sections. The MCLZ methods underestimated the highest order experimental lines, so a modified "shifted" low-energy ℓ-distribution was applied (MCLZSL1).

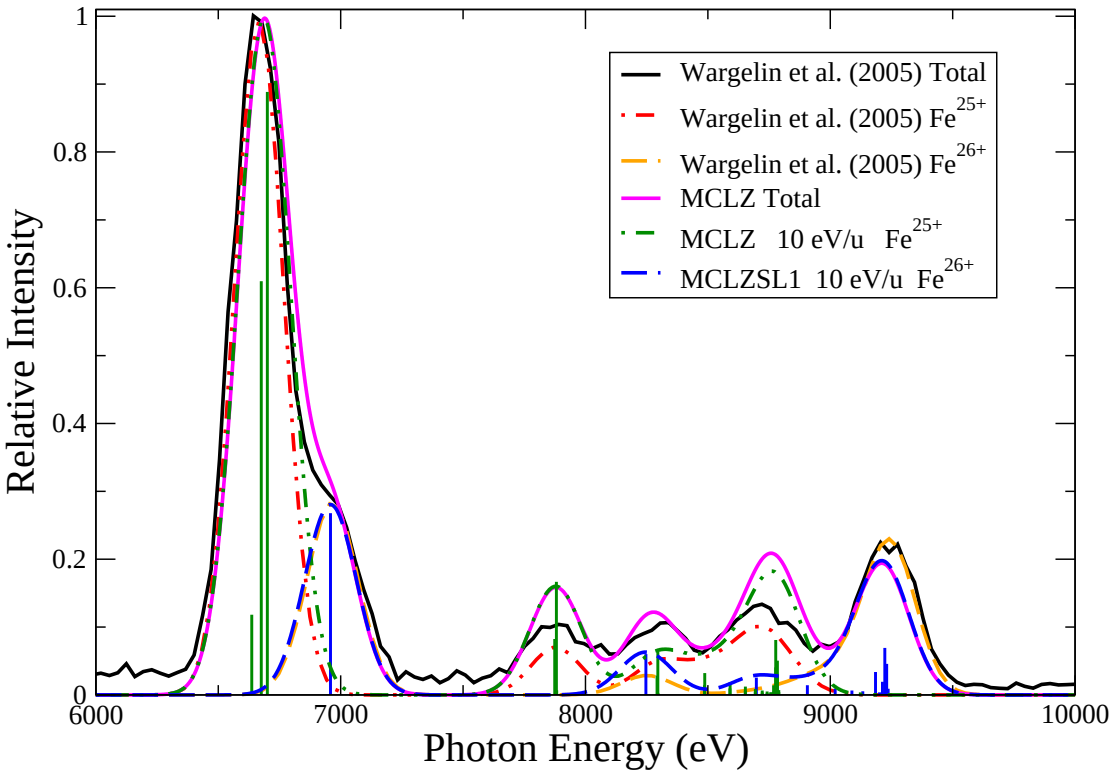

Figure 2.24: Experimental EBIT measurements for Fe^{25+} and Fe^{26+} CX with N_2 (Wargelin et al., 2005) are compared to the best attempt for the theoretical spectra using MCLZ low-energy and MCLZ SL1ℓ-distribution cross sections.

spectra were produced for 1eV/u to 1 keV/u in an attempt to fit the spectrum most closely. In all cases, as Figure 2.22 shows, the MCLZ Kβ and Kδ lines overestimate the experimental lines. It is interesting to note that the lowest collision energy MCLZ spectrum (1 eV/u) most closely matches the experimental spectrum for all lines, but the variation is small for all but the highest order lines. Given the uncertainties in the experimental data, we assume that the 10 eV/u MCLZ lines are in reasonable agreement with the EBIT spectrum.

As Wargelin et al. (2005) were unable to isolate the Fe^{26+} spectrum, the experimental spectrum shown in Figure 2.23 is the result of the spectrum of Fe^{25+} CX with N_2 in Figure 2.22 subtracted from the total spectrum of Fe^{25+} and Fe^{26+} CX with N_2 shown in Fig 2.24. In this case, MCLZ calculations were unable to sufficiently fit the experimental Lyν (14p $\rightarrow$ 1s) peak for the range of energies shown in Figure 2.23; the 10 eV/u and 100 eV/u spectra grossly underestimate the Lyν line. This line is quite strong in the experimental spectrum at $\sim$80% the intensity of the Lyα peak. In a first attempt to fit this peak using the MCLZ cross section data, all cross-sections were shifted to ℓ=1 (p) state which resulted in an extremely large Lyν peak, suggesting that the MCLZ low-energy ℓ-distribution is insufficient in the ℓ=1 state, but should not be completely populated by this state. The ℓ=2 (d) states were larger than the p-states, so for the next modified ℓ-distribution, all ℓ states were shifted by ℓ=ℓ-1, so that the original ℓ=2 states now populate the ℓ=1 states, and the original ℓ=3 states populate the ℓ=2 states, and so on. The original ℓ=0 (s) state was also summed with the new p state. This shifted low-energy distribution, or MCLZ SL1, resulted in a closer fit for the entire spectrum. Further details are discussed in Mullen et al. (2016b).

The 10 eV/u MCLZ spectrum from Figure 2.22 and the 10 eV/u MCLZSL1 spectrum produced in Figure 2.23 were summed to compare to the combined spectrum from Wargelin et al. (2005), as shown in Figure 2.24. Assuming a concentration of $\sim$ 30% Fe^{26+}, compared to the 1:2 fraction determined in Wargelin et al. (2005), using the MCLZ method for Fe^{25+} and the MCLZSL1 distribution for Fe^{26+} spectra, a reasonable match to the experimental

measurements at 10 eV/u was obtained, as shown in Figure 2.24.

2.2.4 Results and Comparisons: C^{6+}

Experiments were performed for single electron capture for C^{6+} with He (Defay et al., 2013) and H_2 (Fogle et al., 2014) for varying collision energies using a high-resolution microcalorimeter detector. Figure 2.25 shows the experimental spectra for C^{6+} CX with He for collision energies from 464 eV/u to 18.364 keV/u. For this collisional system, as the energy increases, the relative intensity of the Lyβ line changes in intensity, with the peak intensity for the Lyβ line occuring at 2689 eV/u. A theoretical spectrum using MCLZ calculations was then compared to the Experiment in Figure 2.26. In this case, the theoretical Lyβ line ratio underestimates the experimental line ratios, and the Lyγ line is $\sim$0. For the experimental collisions of C^{6+} with H_2 shown in Figure 2.27, while the Lyβ line is significantly smaller than for the collision with He, the Lyγ line also contributes significantly to the spectrum for all collision energies. For this collision, the Lyβ and Lyγ peaks are largest for the collision energy of 3351 eV/u. The theoretical spectrum calculated with the MCLZ low-energy ℓ-distribution for the collision energy of 930 keV/u, shown in Figure 2.28, is very similar to the experimental spectrum for all lines.

2.2.5 Results and Comparisons: Hardness Ratios

Throughout this chapter, it has been shown that the ratios of the Lyβ and higher lines to the Lyα lines vary with collisional energy. This variation is shown as the β and higher peaks increase and decrease in relative intensities as the collision energy changes. This energy dependence can be significant for some ions, and can be a velocity indicator in environments in which it is known that CX is a dominant process, such as in comets (Beiersdorfer et al., 2001). The Hardness ratio, H, is the sum of all line intensities for Lyβ and higher divided by

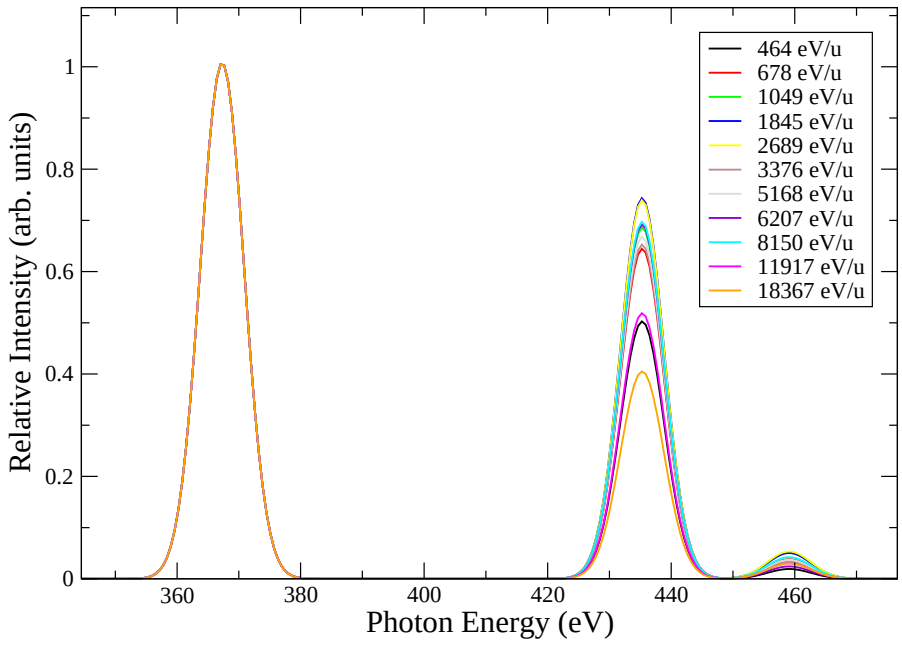

Figure 2.25: Experimental measurements for C^{6+} CX with He for various collision energies (Defay et al., 2013). A Gaussian FWHM of 5 eV is chosen for all collision energies.

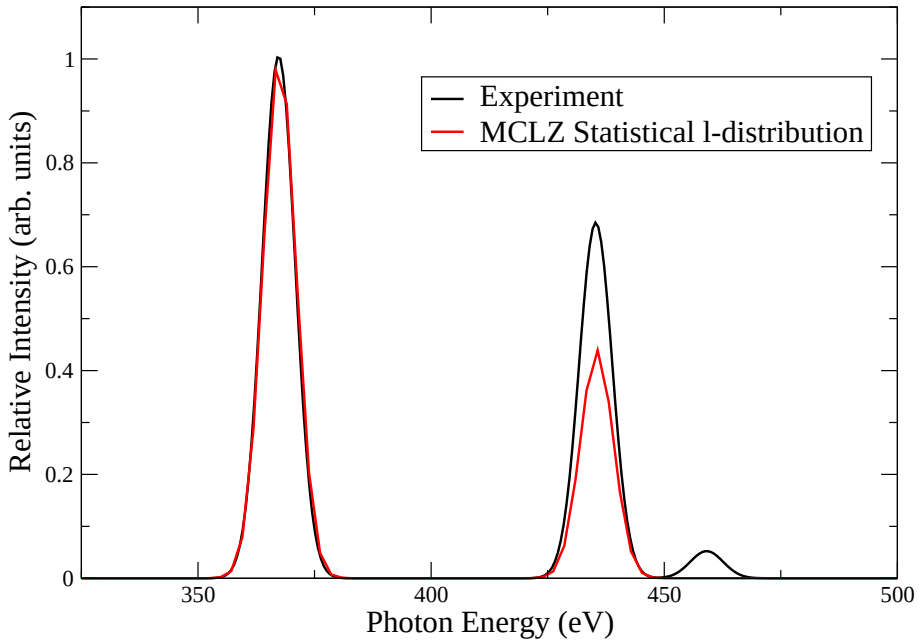

Figure 2.26: Experimental measurements for C^{6+} CX with He at 930 eV/u (420 km/s, Defay et al., 2013) compared to MCLZ statistical calculation at the same energy. A Gaussian FWHM of 5 eV is used.

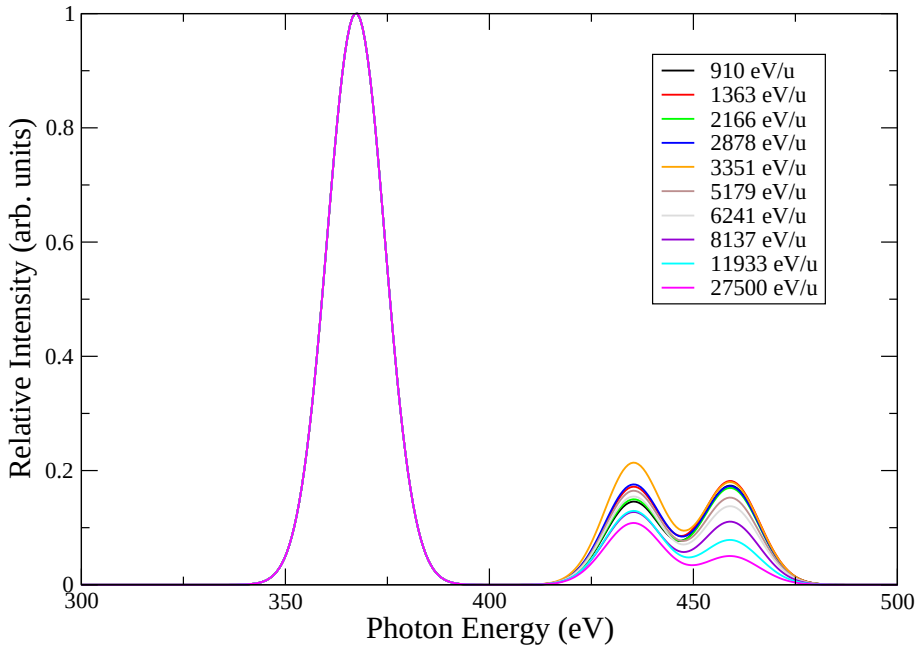

Figure 2.27: Experimental measurements for C^{6+} CX with H_2 for various collision energies (Fogle et al., 2014). A Gaussian FWHM of 10 eV is chosen for all collision energies.

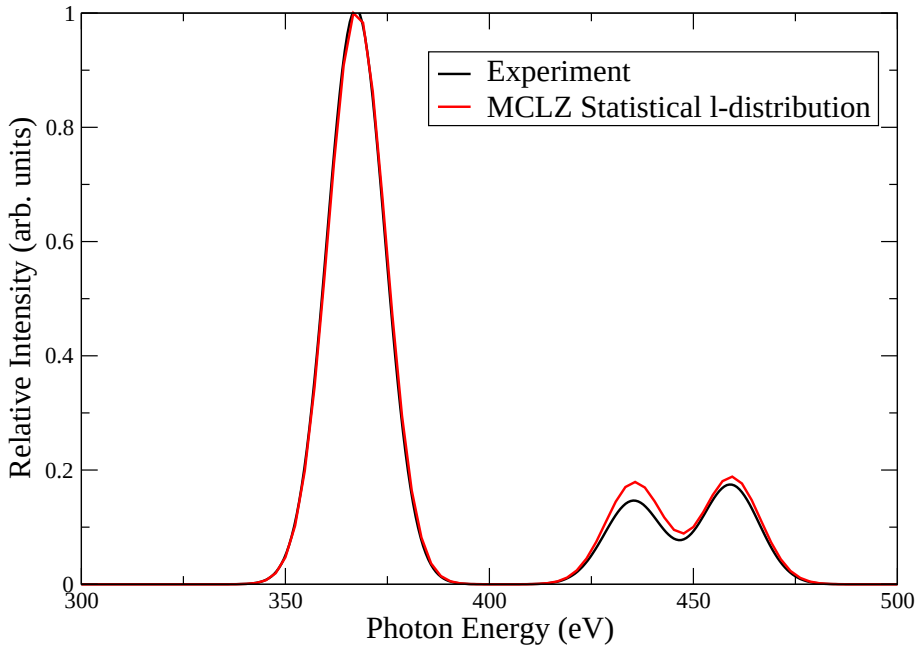

Figure 2.28: Experimental measurements for C^{6+} CX with H_2 at 1 keV/u (451 km/s, Fogle et al., 2014) compared to MCLZ low-energy calculation at the same energy. A Gaussian FWHM of 10 eV is used.

the Lyα line intensity. Figures 2.29 and 2.30 show the hardness ratios for He-like ions and H-like ions colliding with H. The He-like hardness ratios are significantly smaller than the H-like hardness ratios in general. The more accurate methods of cross section calculations (QMOCC, AOCC, CTMC) show a stronger dependence on energy than the MCLZ methods for both cases.

2.3 Summary

Charge exchange cross-sections are calculated using the QMOCC, AOCC, CTMC, and MCLZ approaches. Spectra are produced for Ne^{10+} and Ne^{9+} collisions with H and He for AOCC, CTMC, and MCLZ calculations. Cross-sections are compared for the dominant capture channel $n = 6$ before comparisons are made to measurements for Ne^{10+} with He. For Fe^{25+} and Fe^{26+} collisions with N_2, comparisons are also made to measurements. For Fe^{26+} spectra, the MCLZ low-energy ℓ distribution is not able to adequately fit the spectrum, so a modified distribution, the MCLZSL1 distribution, is applied which results in a decent fit. Charge exchange hardness ratios are shown for H-like and He-like C, N, O, Ne, Mg, and Si collisions with H, and Lyα and Kα to β ratios are discussed for Fe^{25+} and Ne^{10+}.

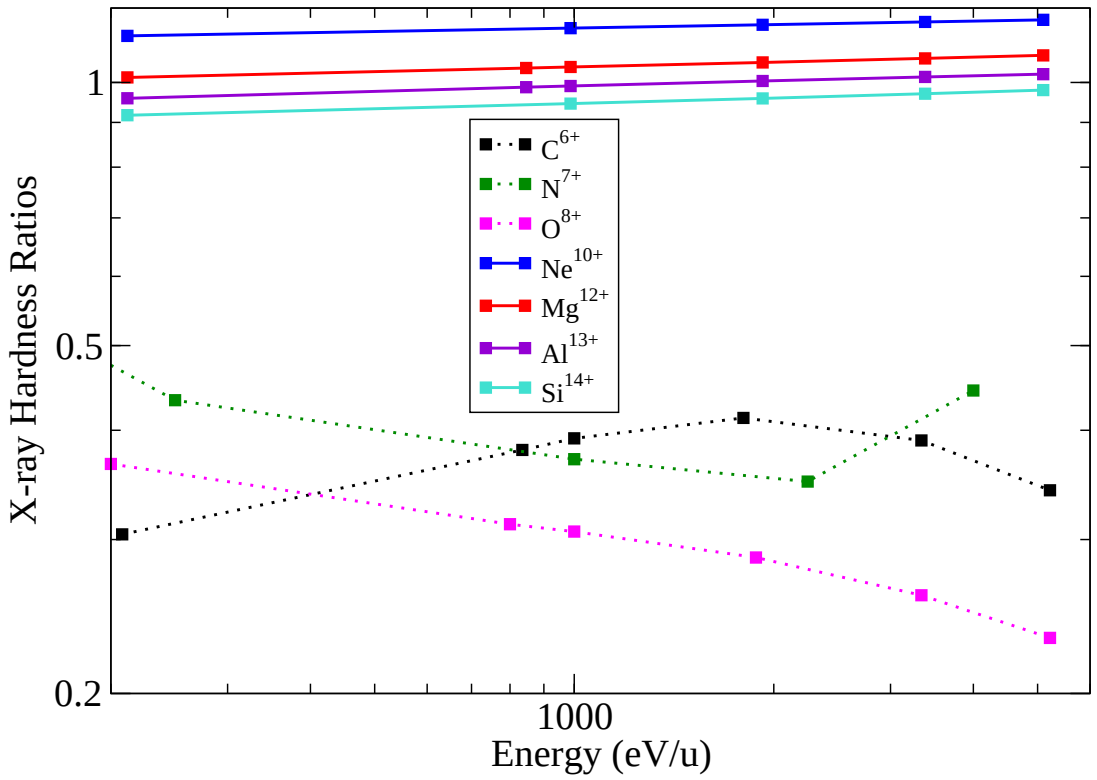

Figure 2.29: H-like Hardness ratios for collisions with H. Solid lines indicate MCLZ low energy ℓ-distribution calculations. C^{6+} recommended calculations are from Janev et al. (1993), N^{7+} MOCC calculations are from Harel et al. (1998), and O^{8+} recommended cross-sections are from Janev et al. (1993).

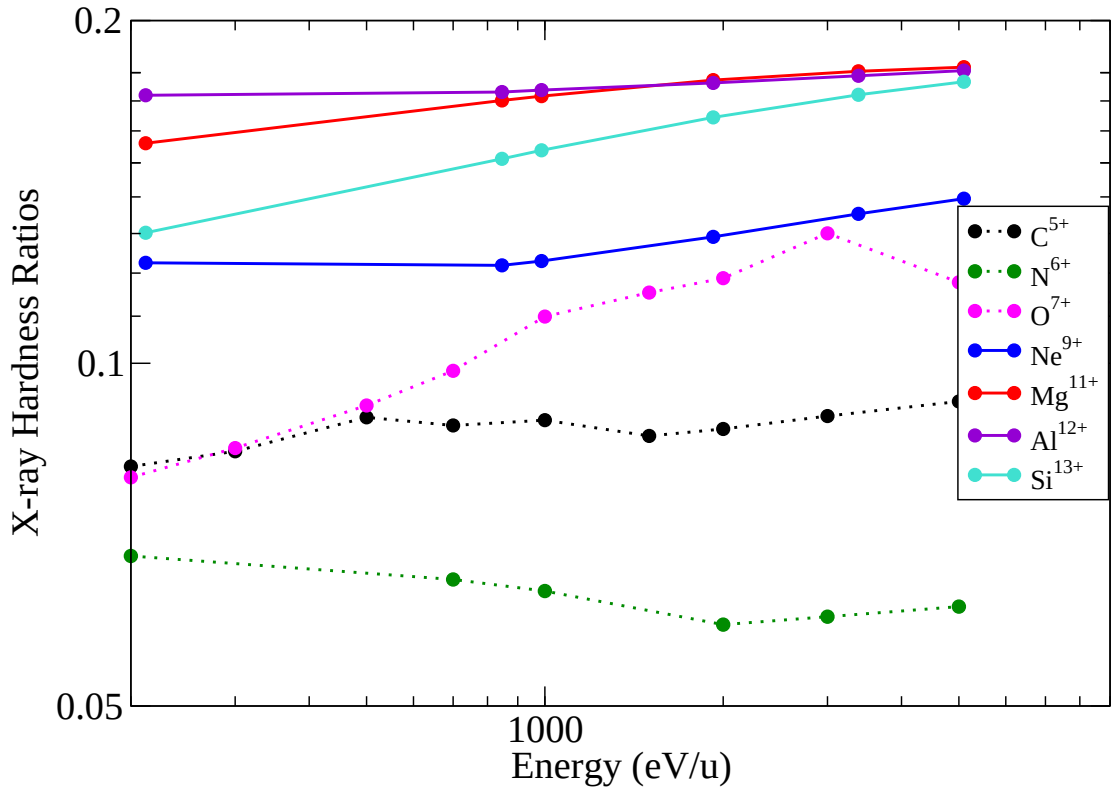

Figure 2.30: He-like Hardness ratios (H) for collisions with H. Solid lines indicate MCLZ calculations. C^{5+} QMOCC calculations are from Nolte et al. (2012), N^{6+} QMOCC calculations are from Wu et al. (2011), and O^{7+} QMOCC cross-sections are from Nolte (2016).

Chapter 3

Charge Exchange Emission Model

3.1 Modelling Packages

It is essential to produce realistic theoretical charge exchange spectra for comparing to astrophysical observations. Since the first observations of comet Hyakutake (Lisse et al., 1996; Cravens, 1997), the X-ray emission spectra of over 30 comets have been studied. It has been shown that the X-ray emission spectra of these comets are primarily due to solar wind charge exchange (SWCX) with cometary neutrals (Snios et al., 2016; Ewing et al., 2013; Dennerl, 2010; Bodewits et al., 2007; Krasnopolsky et al., 2004). In these cases, a pure charge exchange X-ray model can provide a reasonable fit to cometary spectra. The *SPEX* package (Gu et al., 2016) is a useful tool for determining the contribution of CX in an observed spectrum. This package uses cross-sections available in the literature and determines missing n- and ℓ-resolved cross sections through scaling relations. Gu et al. (2016) were able to fit the spectrum of comet C/2000 WM1 (LINEAR), shown in their Figure 5, reasonably well using the *SPEX* package, but an improved fit was made when this package was supplemented with MCLZ data from the *Kronos* database incorporating various cometary neutrals (Mullen et al., 2016b). For cometary spectra, Snios et al. (2016) consider many velocities for

each ion-atom collision in their models while most other studies consider a single velocity or ignore the affect of velocity on CX emission spectra.

Outside of our solar system, such as in starburst galaxies and supernova remnants, a variety of processes might contribute to the observed X-ray emission spectra, and must be considered in models. In these cases, modeling packages can be useful for considering the contribution of each process. *XSPEC* (Arnaud, 1996) is an interactive X-ray spectral fitting program that is used to fit models to observed X-ray spectra. It is command driven and is detector-independent such that it can be used for any spectrometer. The AtomDB CX model, or *ACX* package (Smith et al., 2014) is available for use in *XSPEC*. While it does not include real CX cross-sections, it is very useful for determining if CX has a contribution to an observed spectrum. This model simulates CX by calculating the dominant or peak excited level which depends on the charge of the ion and the ionization potential of the neutral. It then considers a variety of ℓ-distributions, including the statistical ℓ-distribution we consider for the MCLZ method. Using the *ACX* package along with a thermal plasma model available in XSPEC, Zhang et al. (2014) fit the *XMM-Newton RGS* X-ray spectrum of the star forming galaxy M82. They determined that about $\frac{1}{4}$ of the X-ray flux from the 6-30 Å band for the RGS is due to charge exchange.

There are various other approaches for determining the contribution of CX in an observed spectrum. In the following models that I will discuss for the Cygnus Loop supernova remnant, line ratios are directly applied in *XSPEC* for each ion-neutral collision for a single velocity, along with the appropriate contributions from other processes. The initial model in §3.2.2 only considers H-like and He-like C, N, and O ions colliding with H at 1 keV/u (435 km/s). This model is then enhanced in §3.2.3 to include collisions of Ne, Mg, Al, and Si and considers a fraction of 10% He for various collision energies. In an analysis of the Lyβ to Lyα ratios of M82, the theoretical line ratios are then compared to the observed line ratios for M82 for different portions of the galaxy in order to determine if CX can explain the observed ratio

between these lines.

3.2 Model of the Cygnus Loop SNR

3.2.1 Observational Analysis

Here, a *Suzaku* observation is analyzed of one of the fields studied along the rim of the Cygnus Loop by Katsuda et al. (2011), labeled NE4 in their Figure 1. NE4 includes part of the northeastern rim of the Cygnus Loop and is a region believed to have a significant neutral H fraction. The pointing direction was $(\alpha, \delta) = (20^{\rm h}54^{\rm m}00\overset{\rm s}{.}12, +32^\circ22'08\overset{''}{.}4)$ (see Figure 3.1). The observation was carried out on 2005 Nov 30 and given *Suzaku* observation ID 500023010.

We reduced the *Suzaku* X-ray Imaging Spectrometer (XIS) data and extracted X-ray spectra using version 6.12 of HEASoft,[1] using the calibration data that was current as of 2013 Mar 23. We first ran the `aepipeline` script, to reprocess the events list using the most recent calibration data. This script also screens the data – we applied the standard screening recommended in the *Suzaku* ABC Guide.[2] Then, for each XIS camera, we combined the data taken in the 3×3 and 5×5 modes. Figure 3.1 shows the resulting 0.3–2.0 keV X-ray image from the XIS1 camera.

From each of the four XIS cameras we extracted an X-ray spectrum of the bright rim of the Cygnus Loop. We extracted these spectra from a $\sim 2'$ wide strip positioned by eye along the rim (the green polygon in Figure 3.1). We grouped each spectrum such that there were at least 25 counts per spectral bin. For each of these spectra we generated a corresponding non-X-ray background (NXB) spectrum, to be subtracted from the source spectrum in the subsequent spectral analysis. For this purpose we used the `xisnxbgen` tool (Tawa et al., 2008), which constructs NXB spectra using a database of *Suzaku* observations of the night-

[1] http://heasarc.gsfc.nasa.gov/lheasoft/
[2] http://heasarc.gsfc.nasa.gov/docs/suzaku/analysis/abc/abc.html

side of Earth. We also generated the response files for each spectrum, using `xisrmfgen` to calculate the redistribution matrix files (RMFs) and `xissimarfgen` (Ishisaki et al., 2007) to calculate ancillary response files (ARFs), assuming a uniform extended source. Note that the latter tool takes into account the temporally and spatially varying contamination on the XIS cameras' optical blocking filters.

The spectra from the three front-illuminated (FI) cameras (XIS0, XIS2, and XIS3) were combined into a single spectrum (with corresponding NXB spectrum and response files) using `addascaspec`. In the following spectral analysis, CX models were fitted to this combined FI spectrum and to the spectrum from the back-illuminated (BI) XIS1 camera simultaneously.

3.2.2 Simple Analysis of CX in the Cygnus Loop: 1 keV/u

Recent X-ray studies have shown that supernova shock models are unable to satisfactorily explain X-ray emission in the rim of the Cygnus Loop. In an attempt to account for this "anomalously" enhanced X-ray flux, the region was fit with a model including theoretical charge exchange (CX) data along with shock and background X-ray models. The model includes the CX collisions of O^{8+}, O^{7+}, N^{7+}, N^{6+}, C^{6+}, and C^{5+} with H with an energy of 1 keV/u (438 km/s). The observations reveal a strong emission feature near 0.7 keV that cannot fully be accounted for by a shock model, nor the current CX data. Inclusion of CX, specifically O^{7+} + H, does provide for a statistically significant improvement over a pure shock model.

In order to produce the CX-induced portion of the spectra to be used in our model of the Cygnus Loop, we applied a low density, steady-state radiative cascade model as described in Rigazio et al. (2002) (see § 2.2). In this model, the initial state populations are proportional to the quantum-state-resolved CX cross sections. As the electron cascades down to the lowest energy level obeying quantum mechanical selection rules, photons are emitted, including X-rays. Our model includes X-ray emission spectra produced using cross sections from the best

available sources for the ions O^{8+} (Janev et al., 1993), O^{7+} (Nolte, 2016), N^{7+} (Harel et al., 1998), N^{6+} (Wu et al., 2011), C^{6+} (Janev et al., 1993), and C^{5+} (Nolte et al., 2012) colliding with atomic H with a collision energy of 1 keV/u (438 km/s).

We considered only ion interactions with neutral H as CX cross section data for He are generally sparse. However, as the H/He elemental abundance ratio is ∼10, neglecting CX reactions involving He should not adversely affect our results. Varying the energy and including He as a target atom along with explicit CX data for Ne, Mg, Fe, and other ions are improvements that are discussed in §3.2.3. In Figure 2.12, example X-ray emission spectra for O^{8+} colliding with H for five collisional energies are given. While Ghavamian et al. (2001) derived a shock speed of 270-350 km/s from the shock's Hα profile, as Figure 2.12 shows, there is little variation in the intensities of the Kβ and higher lines between the collisional energies of 0.5 and 2 keV/u. As data from Janev et al. (1993) are most reliable above 1 keV/u, we chose to use that energy in the current model.

Our first step in analyzing the rim spectra was to determine how well a model spectrum without CX fit the observations. Our model spectra without CX was patterned on that used by Katsuda et al. (2011). We used *XSPEC* version 12.8.1 (Arnaud, 1996) and applied an absorbed VpShock model with a hydrogen column density for the intervening material of the Cygnus Loop of $3\times10^{20}\mathrm{cm}^{-2}$ (Kosugi et al., 2010). In addition, two APEC thermal plasma models and two broken power laws for the X-ray background with the parameters described by Katsuda et al. (2011) and Yoshino et al. (2009) were used with a total Galactic hydrogen column density of $1.7\times10^{21}\mathrm{cm}^{-2}$ for the direction of the Cygnus Loop as described in the Leiden/Argentine/Bonn Survey of Galactic HI (Kalberla et al., 2005). As Figure 3.2 shows, we were not able to adequately fit the spectrum, particularly below 1 keV. Our model resulted in a reduced χ^2 of 8.9 with 592 degrees of freedom (d.o.f.), compared to a reduced χ^2 of 2.21 obtained by Katsuda et al. (2011), even though we followed similar steps in extracting the data (see § 3.2.1) and applied the same model.

Finding their version of this model unsatisfactory, Katsuda et al. (2011) went on to construct a thermal plus CX-inspired model in which the thermal components were drawn from fits to a nearby part of the rim that was not thought to experience CX (their NE2 field) and the CX contribution was modeled as 22 independent emission lines. To compare directly to Figure 6 of Katsuda et al. (2011), we introduced 35 lines to the previous model, in a similar manner in which they introduced 22 lines. Following their steps, we adopted the VpShock parameters for NE2 given in their Table 2. This included an electron temperature of 0.21 keV, and C, N, O, Ne, Mg, Si, and Fe elemental abundances of 0.17, 0.07, 0.08, 0.15, 0.10, 0.10, and 0.14 times the respective solar value. However, unlike Katsuda et al., we resolve all multiplets, hence the additional 13 lines. We assumed that the lines' intrinsic widths are much smaller than the instrumental line width. At this stage, the normalization of each line was allowed to vary independently as shown in Figure 3.3. While this resulted in a much improved reduced χ^2 of 1.36 with 533 d.o.f., the relative line intensities of a given ion are unconstrained by laboratory data and can lead to unphysical line ratios. As column 3 in Table A.1 shows, for cases such as C VI where Lyα is essentially zero, the Lyβ/Lyα line ratio is much greater than 1. The higher-order CX emission lines have intensities which are usually smaller than the Kα feature. An example is shown in the case of O^{8+} colliding with H in Figure 2.12 in which the Lyβ/Lyα line ratio is $\sim$0.1.

In order to incorporate realistic CX spectra, we then tied the normalizations of the Kβ and higher lines to their respective Kα resonant line, as shown in Figure 3.4, based on the CX cascade spectra described above. The normalizations are given in column 4 in Table A.1. This resulted in a reduced χ^2 of 3.95 with 555 d.o.f. While the fit quality is reduced relative to the unconstrained spectra, the CX line ratios are physically reasonable, being obtained from theoretical CX cross sections.

Katsuda et al. (2011) found that their shock + background model was not as bright around 0.7 keV as the observed spectrum. Hence they suggested that the 0.7 keV band

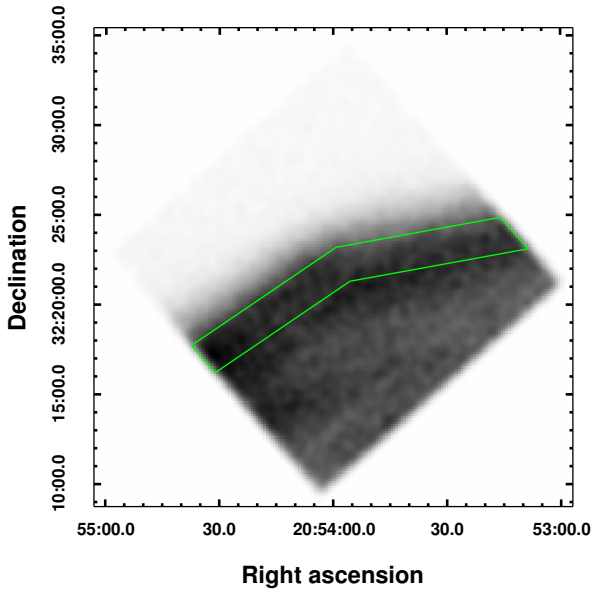

Figure 3.1: Smoothed 0.3–2.0 keV XIS1 image of the NE4 field of the Cygnus Loop. The image has not been background-subtracted nor flat-fielded. The green polygon shows the region from which we extracted the spectrum of the Cygnus Loop rim.
.

might be due to Fe XVII/Fe XVI L-shell emission and/or O K-shell CX. They ultimately discarded the Fe contribution in their final models. Our CX + shock + background model is also unable to fully account for the observed 0.7 keV emission. However, as we included realistic oxygen CX, we note that oxygen CX emission does contribute to the spectrum, but it alone cannot fully explain the feature. Since Fe^{16+} and Fe^{17+} + H CX line ratios are not available, we modeled these spectral features with two unconstrained lines at 0.726 keV and 0.822 keV, following the original suggestion of Katsuda et al. (2011). As Figure 3.5 shows, the spectrum fit is improved, resulting in a reduced χ^2 of 1.83 with 553 d.o.f. Our model, as described in Column 5 of Table A.1, found zero intensity for the second line at 0.822 keV in contrast with expectations based on Fe L-shell line ratios found in thermal models and observations in other X-ray emitting regions (see Katsuda et al. and references therein).

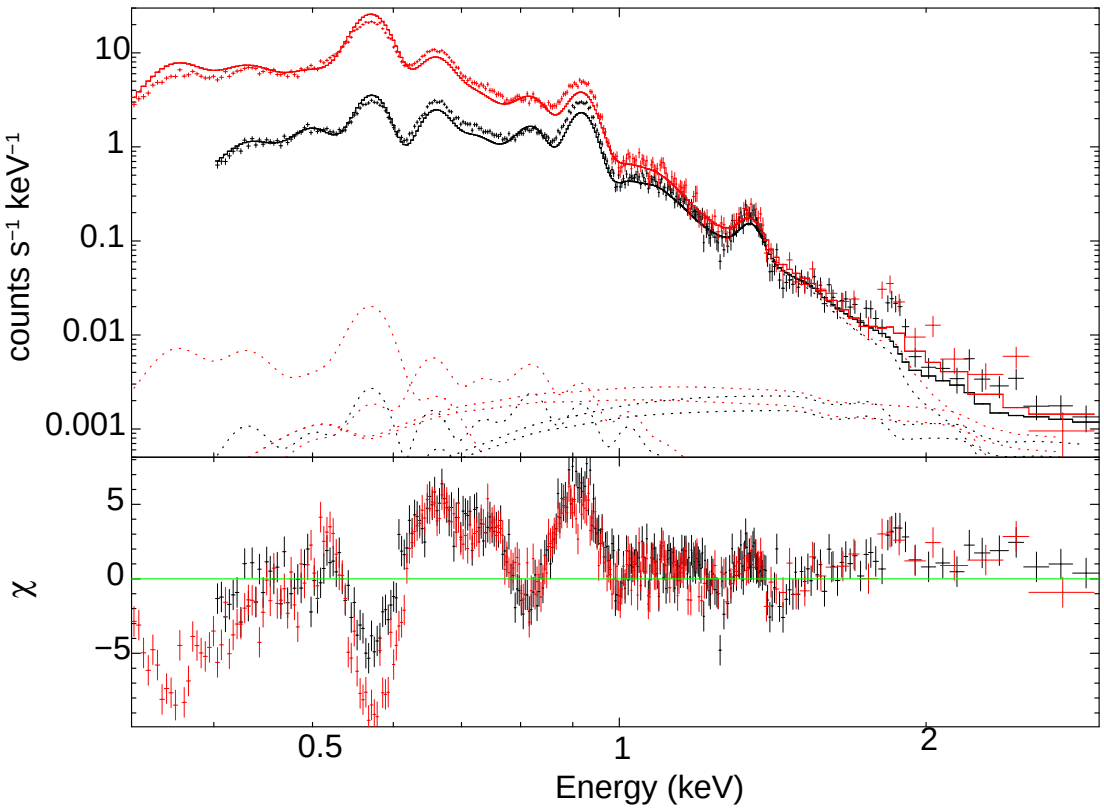

Figure 3.2: (a) Spectrum (crosses) from NE4's outermost rim of the Cygnus Loop as described in Figure 1 of Katsuda et al. (2011) along with the best-fit model (lines) including the Absorbed VpShock model. BI spectrum (red), FI spectrum (black). Residuals are shown in the lower panel with a reduced χ^2 of 8.9 with 592 d.o.f.

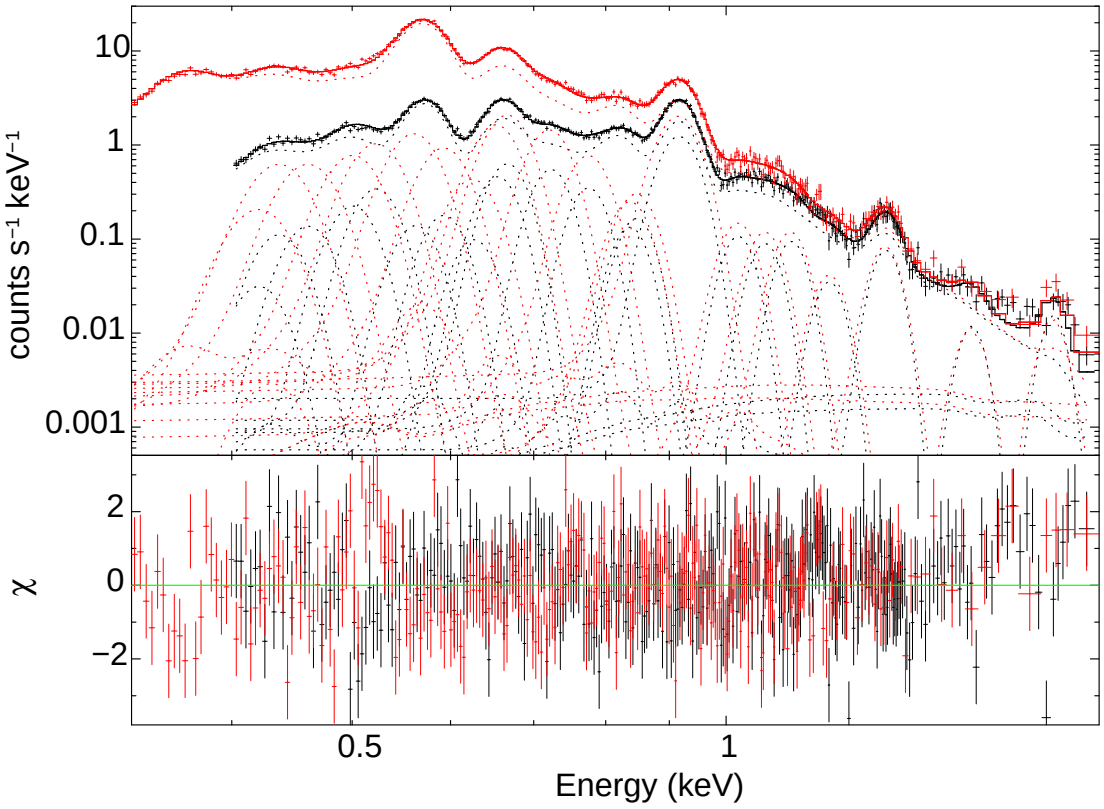

Figure 3.3: Same as Figure 3.2, but with the Absorbed VpShock model and CX-inspired lines whose intensities are independently varied in the fit. This figure can be compared to Figure 6 from Katsuda et al. (2011). Residuals show a reduced $\chi^2 = 1.36$ with 533 d.o.f.

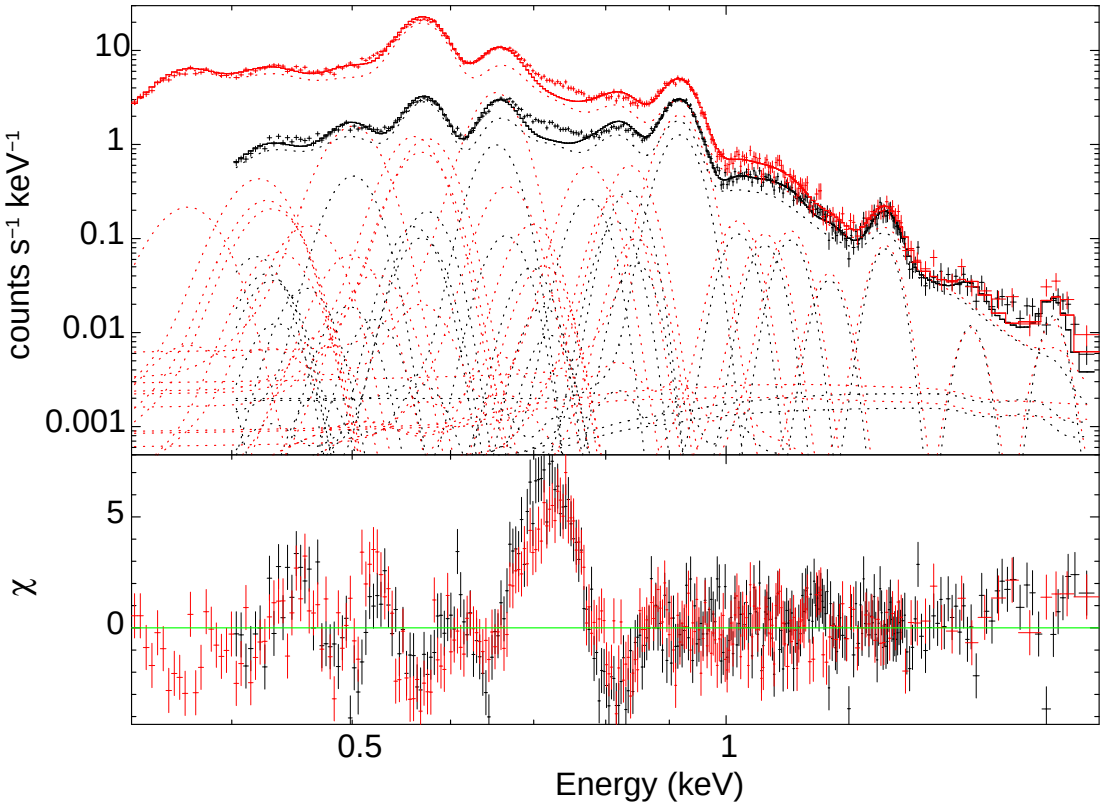

Figure 3.4: a) Same as Figure 3.3, but with the Absorbed VpShock model and theoretical CX data. The normalizations for Kβ and higher are tied to the Kα resonant lines for each ion to more accurately depict CX emission spectra. b) Reduced $\chi^2 = 3.95$ with 555 d.o.f. primarily due to the poor fit near 0.7 keV.

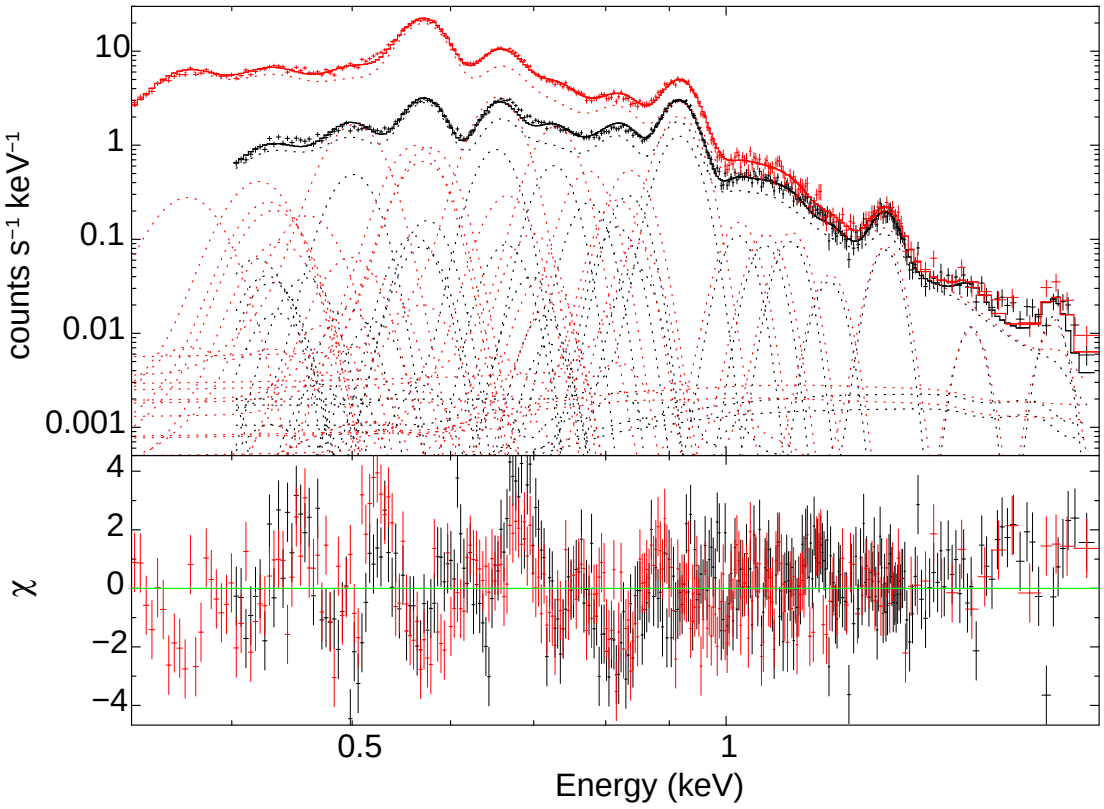

Figure 3.5: a) Same as Figure 3.4, but with the addition of Fe L-shell lines at 0.726 and 0.822 keV. b) Reduced $\chi^2 = 1.83$ with 553 d.o.f.

3.2.3 Improved Analysis of CX in the Cygnus Loop: Velocity Dependence

Updated *XSPEC* charge exchange models of the Cygnus Loop were performed including more ions, targets, and collision energies. H- and He-like C, N, O, Ne, Mg, Al, and Si collisions with H and a 10% fraction of He were considered for collision energies from 200 eV/u ($\sim$ 200 km/s) to 5 keV/u ($\sim$ 1000 km/s). The best available cross-sections were chosen for each collision energy. The line ratios for each ion-H collision are shown in Table A.2 while all line ratios for ion-He collisions are shown in Table A.3

In each of these tables, QMOCC cross sections are used, when available, for the collisions of C^{5+} + H (Nolte et al., 2012), N^{6+} + H (Wu et al., 2011), and O^{7+} + H (Nolte, 2016). AOCC cross-sections are then used for Ne^{10+} + H for energies above 1 keV/u, while CTMC cross-sections are used for energies below 1 keV/u (Cumbee et al., 2016a). AOCC cross-sections are also used for C^{6+} + He (Fritsch and Lin, 1991) for most energies. For C^{6+} + H and O^{8+} + H, recommended cross-sections from Janev et al. (1993) are used, and for N^{7+} +H (Harel et al., 1998), MOCC cross-sections are used. In all other cases, and when energies are missing for other methods, MCLZ cross sections are adopted. For bare-ion collisions, below 1 keV/u, MCLZ low-energy ℓ-distribution cross sections are used, and for energies at and above 1 keV/u, MCLZ statistical ℓ-distribution cross-sections are used. All of these cross-sections can be found in the *Kronos* Database (Mullen et al., 2016a,b; Cumbee et al., 2016b).

Pure charge exchange spectra are shown for each collision energy in Figure 3.6, with the assumption that all ions have the same abundance. In this case, all spectra are normalized by the sum of the total X-ray spectrum so that the sum of all Lyα+ lines and all Kα+ lines are equal to 1. The 1 keV/u spectrum is highlighted in black for comparison to the model discussed in §3.2.2. A line-ratio spectrum for the lowest collision velocity of 200 eV/u is

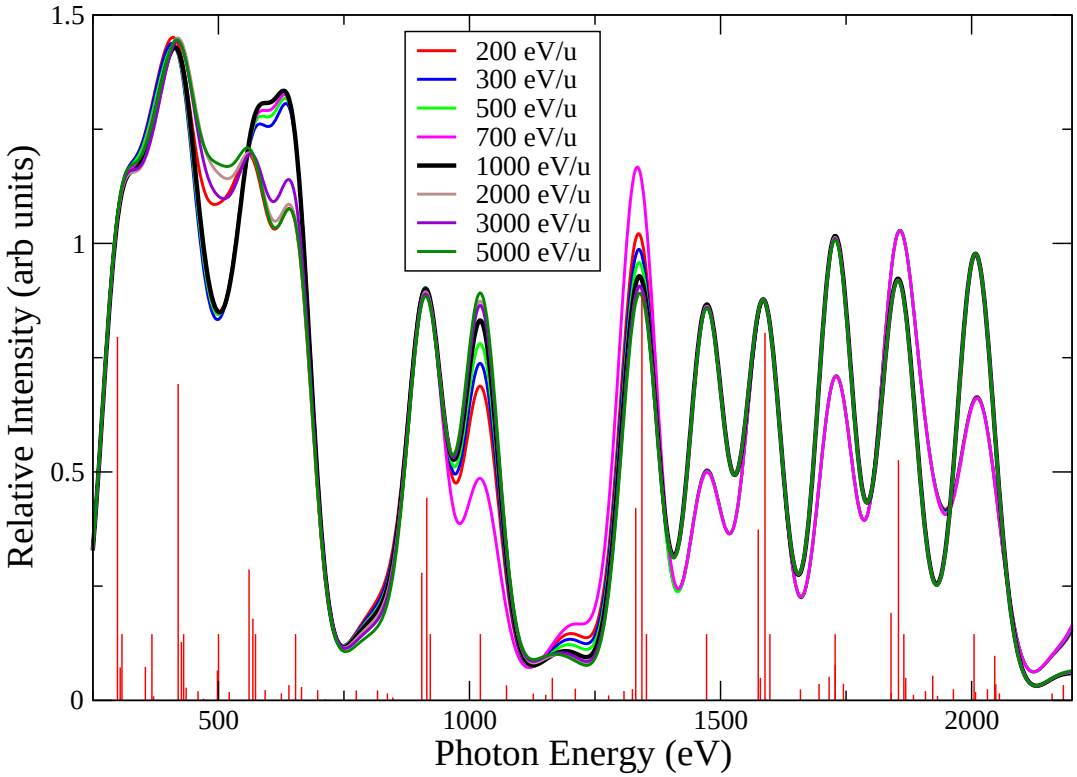

Figure 3.6: CX X-ray emission line ratios for H-like and He-like C-Si ions colliding with H and 10 % fraction of He, with each spectrum having a normalization of 1, indicating a similar abundance for each ion. Line ratios are described in Tables A.2 and A.3. The line ratios are convolved with a 50 eV FWHM Gaussian to produce the spectra shown.

shown. A poor resolution with a Gaussian FWHM of 50 eV was chosen in order to more clearly highlight the variation in velocity. At the lowest photon energies (below $\sim$ 600 eV), the velocity plays a very important role in the intensity of the spectra. In this region, only C, N, and O ions contribute to the spectra, and a dramatic increase in the intensity from the lowest collision energy (200 eV/u) to the highest collision energy (5000 eV/u) is clear. It is important to note that for these ions, QMOCC and recommended cross-sections are used, indicating that this velocity variation is not dominated by uncertainties in the atomic data or having to choose an ℓ-distribution for the MCLZ cross-sections. The Ne^{10+} Lyα line also produces a very strong fluctuation in intensity over the various velocities at $\sim$ 1000 eV using primarily AOCC and CTMC cross-section data, while the strong velocity variation at $\sim$ 1300 eV is primarily due to Mg^{11+} collisions, calculated with MCLZ cross-sections. At $\sim$1500 eV, however, the velocity variation shifts into two forms: the low energy form in which only the 700 eV/u spectrum is visible, and the statistical form in which only the 5000 eV/u spectrum is visible. For the ions that contribute to the spectra at these energies (Mg, Al, and Si), only MCLZ CX calculations are available. Tables A.2 and A.3 show that for the H-like ions, the relative intensity of each line only varies by a small amount both below 700 eV/u in which the low-energy ℓ-distribution cross sections are used, and above 1000 eV/u in which only the statistical ℓ-distribution cross-sections are used. There is, however, a significant variation between the line ratios produced with these two ℓ-distributions. For the He-like collisions such as Al^{12+} in which no ℓ-distribution is necessary, each line only varies slightly for the entire collision energy range, which is highlighted in Figure 3.6 at $\sim$1550 eV in which all spectra have the same intensity. The velocity dependence shown here can make a significant difference in modeling of X-ray observations.

In order to determine what contribution CX with these ions and neutrals has to the X-ray emission spectrum of the Cygnus Loop, these lines were then put into the *XSPEC* CX model, enhancing the model discussed in § 3.2.2 which only includes C, N, and O ions

colliding with H. Figure 3.7 shows the best fit of this model in *XSPEC* for the collision energy of 2 keV/u. The best attempted fit for this model, similar to Figure 3.4, was still unable to account for the X-ray enhanced region at 0.7 keV. This fit has a reduced χ^2 of 3.7, which is a slight improvement over the reduced χ^2 of 3.95 obtained in Figure 3.4. Two lines, mimicking CX from Fe^{16+} were then added, as done in Figure 3.5, which resulted in a much better fit with a reduced χ^2 of 1.91 as shown in Figure 3.8. The quality of the fit is similar to that obtained in Figure 3.5 indicating that the addition of the Ne, Mg, Al, and Si lines due to CX does not improve the model for the Cygnus Loop, or that the velocity is not appropriate for this supernova remnant.

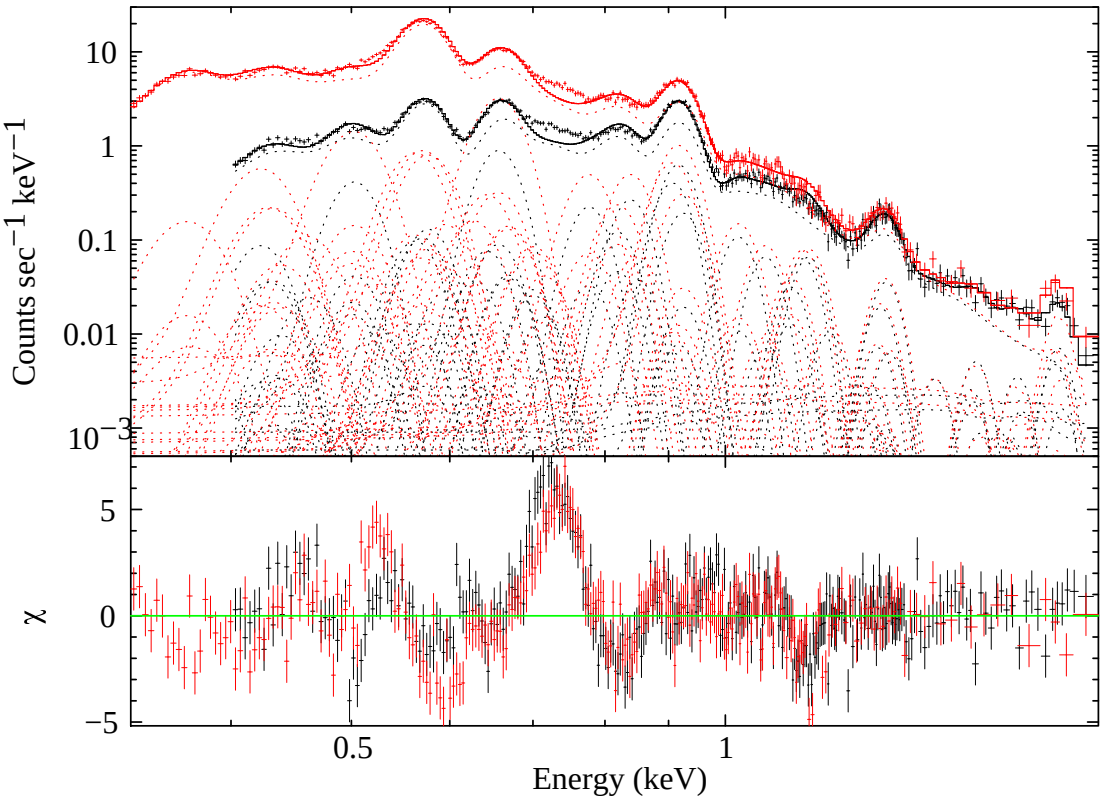

Figure 3.7: Same as Figure 3.4, but with additional lines including C-Si ions colliding with H and a 10 % fraction of He for a collision energy of 2 keV/u. Reduced χ^2 of 3.7

Table 3.1: Model Line Normalizations for Charge Exchange with H and 10% He

Line	Energy (eV)	200 eV/u (195.7 km/s)	300 eV/u (239.7 km/s)	500 eV/u (309.4 km/s)	700 eV/u (366.1 km/s)	1000 eV/u (437.5 km/s)	2000 eV/u (618.8 km/s)	3000 eV/u (757.8 km/s)	5000 eV/u (978.4 km/s)
C V K α r	307.9	$0.000^{+30.65}_{-0.000}$	$0.000^{+8.000}_{-0.000}$	$0.000^{+8.000}_{-0.000}$	$0.000^{+8.000}_{-0.000}$	$0.000^{+8.000}_{-0.000}$	$0.000^{+16.00}_{-0.00}$	$0.022^{+48.42}_{-0.000}$	$0.000^{+50.47}_{-0.000}$
C VI Ly α	367.49	$189.0^{+36.81}_{-84.52}$	$220.7^{+42.56}_{-54.64}$	$233.9^{+57.27}_{-38.07}$	$262.5^{+23.52}_{-83.31}$	$304.9^{+39.81}_{-49.75}$	$171.9^{+43.66}_{-43.47}$	$238.5^{+134.2}_{-85.75}$	$168.1\ ^{+34.69}_{-67.04}$
N VI K α r	430.7	$66.99^{+4.684}_{-4.965}$	$77.38^{+3.968}_{-6.531}$	$83.76^{+7.652}_{-4.066}$	$87.85^{+6.135}_{-5.850}$	$97.55^{+4.636}_{-8.549}$	$87.57^{+12.75}_{-4.591}$	$100.3^{+7.547}_{-6.821}$	$106.9\ ^{+7.610}_{-7.179}$
N VII Ly α	500.28	$388.9^{+13.21}_{-13.35}$	$258.8^{+10.77}_{-8.734}$	$240.6^{+10.48}_{-9.131}$	$233.4^{+10.02}_{-9.668}$	$206.9^{+11.81}_{-8.813}$	$350.3^{+14.02}_{-13.48}$	$347.0^{+7.778}_{-20.22}$	$373.4\ ^{+12.94}_{-14.94}$
O VII K α r	573.95	$181.6^{+6.894}_{-7.157}$	$182.3^{+6.583}_{-8.398}$	$203.9^{+6.401}_{-10.39}$	$219.7^{+6.855}_{-11.22}$	$231.8^{+12.35}_{-7.200}$	$220.8^{+8.043}_{-9.758}$	$201.7^{+8.15}_{-8.038}$	$170.9\ ^{+7.903}_{-7.215}$
O VIII Ly α	653.56	$436.8^{+7.955}_{-7.825}$	$421.1^{+8.067}_{-8.61}$	$438.3^{+10.19}_{-6.659}$	$446.2^{+13.28}_{-4.682}$	$535.4^{+8.22}_{-11.16}$	$589.9^{+9.868}_{-9.571}$	$591.6^{+12.75}_{-7.991}$	$637.0\ ^{+10.86}_{-9.891}$
Ne IX K α r	922.02	$34.36^{+0.573}_{-0.546}$	$35.55^{+0.652}_{-0.501}$	$36.44^{+0.277}_{-0.936}$	$36.74^{+0.253}_{-0.987}$	$35.44^{+0.604}_{-0.596}$	$34.18^{+0.518}_{-0.574}$	$32.82^{+0.537}_{-0.519}$	$31.91\ ^{+0.484}_{-0.5400}$
Ne X Ly α	1021.65	$10.86^{+0.869}_{-0.869}$	$12.12^{+0.978}_{-0.913}$	$13.05^{+1.105}_{-0.908}$	$5.865^{+0.597}_{-0.461}$	$15.28^{+1.154}_{-1.136}$	$15.80^{+1.166}_{-1.195}$	$15.42^{+1.211}_{-1.154}$	$15.59\ ^{+1.234}_{-1.153}$
Mg XI K α r	1352.25	$0.406^{+0.052}_{-0.051}$	$0.437^{+0.051}_{-0.050}$	$0.468^{+0.058}_{-0.045}$	$0.329^{+0.055}_{-0.049}$	$0.592^{+0.053}_{-0.052}$	$0.671^{+0.053}_{-0.057}$	$0.665^{+0.056}_{-0.055}$	$0.717\ ^{+0.057}_{-0.057}$
Mg XII Ly α	1472	$0.257^{+0.184}_{-0.183}$	$0.262^{+0.186}_{-0.182}$	$0.256^{+0.191}_{-0.177}$	$0.293^{+0.192}_{-0.175}$	$0.352^{+0.253}_{-0.247}$	$0.353^{+0.249}_{-0.251}$	$0.333^{+0.281}_{-0.271}$	$0.336\ ^{+0.250}_{-0.249}$
Al XII K α r	1598.3	$0.112^{+0.027}_{-0.027}$	$0.113^{+0.028}_{-0.027}$	$0.111^{+0.029}_{-0.027}$	$0.118^{+0.029}_{-0.027}$	$0.106^{+0.028}_{-0.027}$	$0.104^{+0.028}_{-0.028}$	$0.103^{+0.028}_{-0.028}$	$0.102\ ^{+0.029}_{-0.028}$
Al XIII Ly α	1728.1	$0.314^{+0.148}_{-0.147}$	$0.282\ ^{+0.160}_{-0.137}$	$0.251^{+0.155}_{-0.139}$	$0.348^{+0.202}_{-0.188}$	$0.014^{+0.204}_{-0.000}$	$0.000^{+0.149}_{-0.000}$	$0.002\ ^{+0.169}_{-0.000}$	$0.0\ ^{+0.154218}_{-0.0}$
Si XIII K α r	1864.99	$0.487^{+0.055}_{-0.054}$	$0.478^{+0.054}_{-0.053}$	$0.459^{+0.056}_{-0.047}$	$0.444^{+0.052}_{-0.049}$	$0.471^{+0.049}_{-0.048}$	$0.431^{+0.044}_{-0.045}$	$0.430^{+0.045}_{-0.044}$	$0.409\ ^{+0.037}_{-0.047}$
Si XIV Ly α	2004.88	$0.214^{+0.125}_{-0.124}$	$0.218^{+0.124}_{-0.123}$	$0.220^{+0.125}_{-0.121}$	$0.196^{+0.124}_{-0.122}$	$0.302^{+0.151}_{-0.151}$	$0.308^{+0.150}_{-0.152}$	$0.302^{+0.154}_{-0.149}$	$0.306\ ^{+0.153}_{-0.150}$
reduced χ^2		4.42216	4.48461	4.37430	4.47987	3.75379	3.75379	3.84641	3.81405

All Kα resonant and Lyα normalizations are shown for the process of CX in the Cygnus loop. Any normalizations for collisions with He are multiplied by 0.10 to simulate a $\sim$ 10% abundance of He relative to H. All β and higher lines are provided in other tables. For this table, QMOCC cross sections are used when available for C^{5+} + H (Nolte et al., 2012), N^{6+} + H (Wu et al., 2011), and O^{7+} + H (Jeff Nolte, Private communication). AOCC cross-sections are then used for Ne^{10+} + H for energies above 1 keV/u, while CTMC cross-sections are used for energies below 1 keV/u(Cumbee et al., 2016a). AOCC cross-sections are also used for C^{6+} + He Fritsch and Lin (1991) for most energies. For C^{6+} + H and O^{8+} + H, recommended cross-sections from Janev et al. (1993) are used, and for N^{7+} +H (Harel et al., 1998), MOCC cross-sections are used. In all other cases, and when energies are missing for the more "accurate" methods, below 1 keV/u, MCLZ low-energy ℓ-distribution cross sections are used, and for energies at and above 1 keV/u, MCLZ statistical ℓ-distribution cross-sections are used.

Table 3.2: Model Line Normalizations for Charge Exchange with H and 10% He with Fe L-Shell Lines

Line	Energy (eV)	200 eV/u (195.7 km/s)	300 eV/u (239.7 km/s)	500 eV/u (309.4 km/s)	700 eV/u (366.1 km/s)	1000 eV/u (437.5 km/s)	2000 eV/u (618.8 km/s)	3000 eV/u (757.8 km/s)	5000 eV/u (978.4 km/s)
C VI Ly α	367.49	$212.9^{+81.93}_{-29.71}$	$143.2^{+52.25}_{-44.38}$	$154.6^{+44.75}_{-50.21}$	$162.9^{+41.02}_{-48.9}$	$141.1^{+32.28}_{-61.29}$	$225.4^{+39.68}_{-48.85}$	$148.6^{+48.03}_{-59.24}$	$112.1^{+48.59}_{-47.48}$
N VI K α r	430.7	$66.88^{+6.941}_{-3.393}$	$78.87^{+6.457}_{-3.996}$	$90.86^{+5.628}_{-5.594}$	$92.74^{+6.119}_{-5.842}$	$95.08^{+9.983}_{-7.323}$	$88.03^{+5.435}_{-7.972}$	$103.5^{+6.144}_{-8.274}$	$108.2^{+9.47}_{-8.757}$
N VII Ly α	500.28	$414.1^{+12.22}_{-14.09}$	$299.9^{+12.53}_{-7.283}$	$290.2^{+12.35}_{-7.408}$	$278.2^{+7.138}_{-12.96}$	$259^{+15.94}_{-12.45}$	$383^{+11.31}_{-16.58}$	$366.9^{+13.46}_{-16.04}$	$385^{+11.34}_{-16.91}$
O VII K α r	573.95	$142.9^{+7.306}_{-6.832}$	$137.9^{+10.27}_{-5.498}$	$147.4^{+11.9}_{-5.712}$	$163.9^{+13.3}_{-5.918}$	$168.3^{+8.683}_{-10.85}$	$170.5^{+8.621}_{-9.221}$	$156.7^{+8.711}_{-7.617}$	$145.7^{+7.58}_{-7.581}$
O VIII Ly α	653.56	$387^{+6.962}_{-9.193}$	$354.4^{+7.354}_{-9.482}$	$373.3^{+7.426}_{-9.825}$	$381^{+6.094}_{-12.58}$	$447.2^{+11.62}_{-10.72}$	$534.6^{+13.91}_{-7.174}$	$532.7^{+11.58}_{-8.962}$	$582.8^{+15.6}_{-7.168}$
Ne IX K α r	922.02	$34.76^{+0.631}_{-0.498}$	$35.89^{+0.5545}_{-0.5843}$	$36.22^{+0.453}_{-0.748}$	$36.76^{+0.765}_{-0.445}$	$36.11^{+0.543}_{-0.598}$	$34.07^{+0.515}_{-0.577}$	$33.390^{+0.515}_{-0.551}$	$32.260^{+0.506}_{-0.517}$
Ne X Ly α	1021.65	$10.84^{+0.941}_{-0.8}$	$12.04^{+0.8069}_{-1.106}$	$13.05^{+0.975}_{-1.038}$	$5.901^{+0.489}_{-0.568}$	$15.38^{+1.125}_{-1.172}$	$15.47^{+1.184}_{-1.177}$	$15.66^{+1.288}_{-1.088}$	$15.7^{+1.171}_{-1.21}$
Mg XI K α r	1352.25	$0.403^{+0.051}_{-0.052}$	$0.434^{+0.05142}_{-0.050}$	$0.466^{+0.048}_{-0.054}$	$0.327^{+0.056}_{-0.048}$	$0.601^{+0.052}_{-0.055}$	$0.666^{+0.054}_{-0.055}$	$0.670^{+0.055}_{-0.058}$	$0.713^{+0.055}_{-0.060}$
Mg XII Ly α	1472	$0.318^{+0.187}_{-0.18}$	$0.321^{+0.1812}_{-0.187}$	$0.321^{+0.182}_{-0.186}$	$0.343^{+0.181}_{-0.186}$	$0.289^{+0.189}_{-0.330}$	$0.351^{+0.251}_{-0.249}$	$0.364^{+0.248}_{-0.271}$	$0.356^{+0.247}_{-0.252}$
Al XII K α r	1598.3	$0.118^{+0.027}_{-0.027}$	$0.119^{+0.02754}_{-0.028}$	$0.119^{+0.027}_{-0.028}$	$0.125^{+0.029}_{-0.027}$	$0.124^{+0.032}_{-0.025}$	$0.114^{+0.028}_{-0.028}$	$0.116^{+0.029}_{-0.028}$	$0.114^{+0.028}_{-0.029}$
Al XIII Ly α	1728.1	$0.354^{+0.158}_{-0.15}$	$0.324^{+0.1604}_{-0.168}$	$0.298^{+0.146}_{-0.148}$	$0.388^{+0.152}_{-0.158}$	$0.048^{+0.048}_{-0.181}$	$0.000^{+0.000}_{-0.176}$	$0.009^{+0.009}_{-0.190}$	$0.000^{+0.000}_{-0.168}$
Si XIII K α r	1864.99	$0.488^{+0.056}_{-0.054}$	$0.479^{+0.05451}_{-0.053}$	$0.460^{+0.049}_{-0.054}$	$0.447^{+0.052}_{-0.049}$	$0.457^{+0.048}_{-0.046}$	$0.435^{+0.045}_{-0.044}$	$0.442^{+0.044}_{-0.045}$	$0.429^{+0.043}_{-0.044}$
Fe L($3d \rightarrow 2p$)	0.726	$236^{+5.315}_{-8.57}$	$242.7^{+8.964}_{-5.066}$	$240.7^{+8.715}_{-5.2}$	$236.3^{+6.194}_{-7.286}$	$242.3^{+5.899}_{-7.766}$	$225.7^{+5.936}_{-7.547}$	$227.4^{+6.498}_{-6.962}$	$227.1^{+6.772}_{-6.667}$
Fe L($3s \rightarrow 2p$)	0.822	$0.000^{+0.500}_{-0.000}$	$0.000^{+0.500}_{-0.000}$	$0.000^{+0.500}_{-0.000}$	$0.000^{+0.500}_{-0.000}$	$0.000^{+0.000}_{-0.686}$	$0.000^{+0.500}_{-0.000}$	$0.000^{+0.500}_{-0.000}$	$0.000^{+0.500}_{-0.000}$
reduced χ^2		2.47466	2.38022	2.34961	2.45434	2.27481	1.92810	1.92810	1.93168

Same as Table 3.1, but new XSPEC fits including two additional lines to mimic CX for Fe^{16+} collisions at 0.726 keV and 0.822 keV.

A similar model was then performed for 200 eV/u, 300 eV/u, 500 eV/u, 700 eV/u, 1 keV/u, 3 keV/u and 5 keV/u. The *XSPEC* line normalizations for the Lyα and Kα resonant lines were then extracted for all models, and are shown in Table 3.1. These Lyα and Kα resonant line normalizations, along with the line ratios that form the rest of the spectra in Tables A.2 and A.3, are then used to produce synthetic spectra that include only the contribution of CX in the Cygnus Loop. Figure 3.9 shows these synthetic spectra using a Gaussian FWHM of 10 eV, and Figure 3.10 shows these synthetic spectra using a Gaussian FWHM of 50 eV in order to more clearly highlight the intensity variation of the spectra for the different velocities. Table 3.1 also indicates the reduced χ^2 for each collision energy, and for these models, the best fits occurred with a reduced χ^2 of 3.75 at 1 keV/u and 2 keV/u, with the collisions of 3 keV/u and 5 keV/u being close with a reduced χ^2 of 3.8. The fits below 1 keV/u were relatively poor, with the best fit having a reduced χ^2 of 4.37 at 500 eV/u. Figure 3.10 shows that the CX spectra greatly vary around 500 eV and 650 eV, once again highlighting that it is important to consider the velocity of CX collisions when considering observations.

Two lines mimicking Fe L-shell emission at 0.726 and 0.822 keV were then added to the CX models for each energy. The Lyα and Kα resonant line intensities, as determined by *XSPEC* are shown in Table 3.2, and the synthetic spectra with the addition of the Fe L-shell lines are shown in Figure 3.11. While the line at 0.726 keV makes a significant contribution to the spectrum (highlighted in black in the figure), the line at 0.822 has no contribution to the fitted spectrum. Katsuda et al. (2011) note, however, that these two lines usually have similar intensities. Thus, realistic CX line-ratios must be included in the CX model in the future in order to determine how Fe^{16+} CX will affect the spectra.

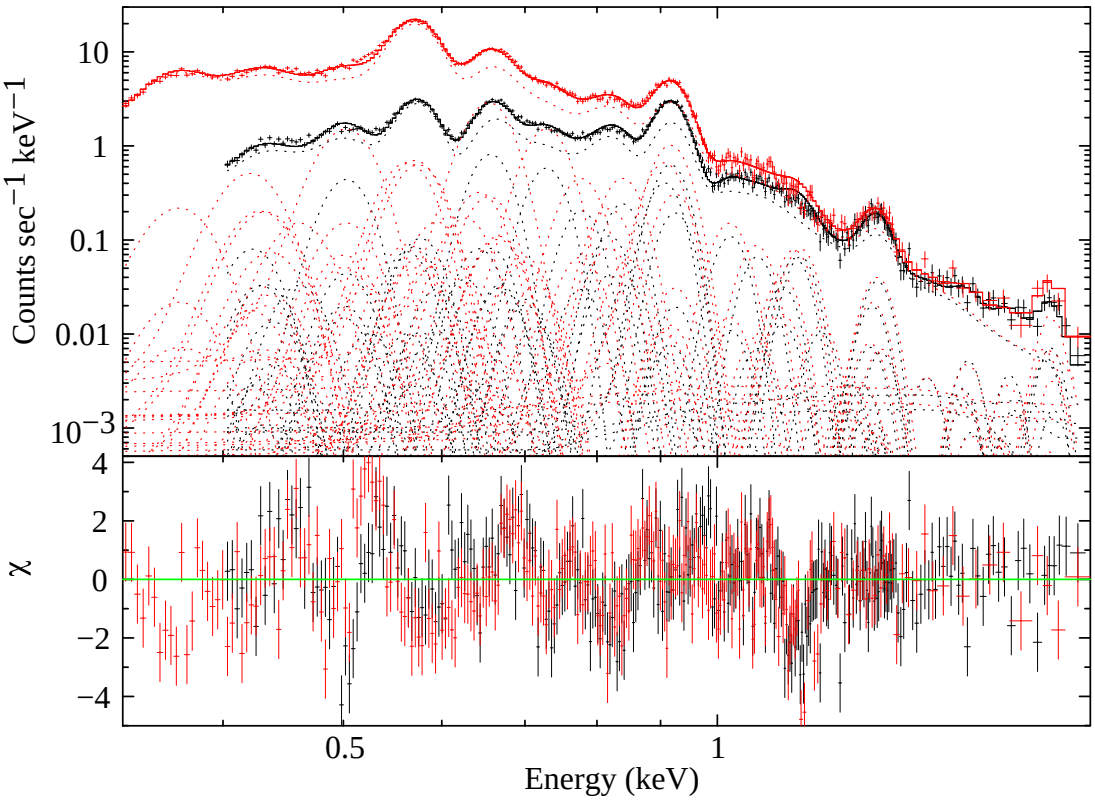

Figure 3.8: Same as Figure 3.7, but with the addition of Fe L-shell lines at 0.726 and 0.822 keV. Reduced χ^2 of 1.91

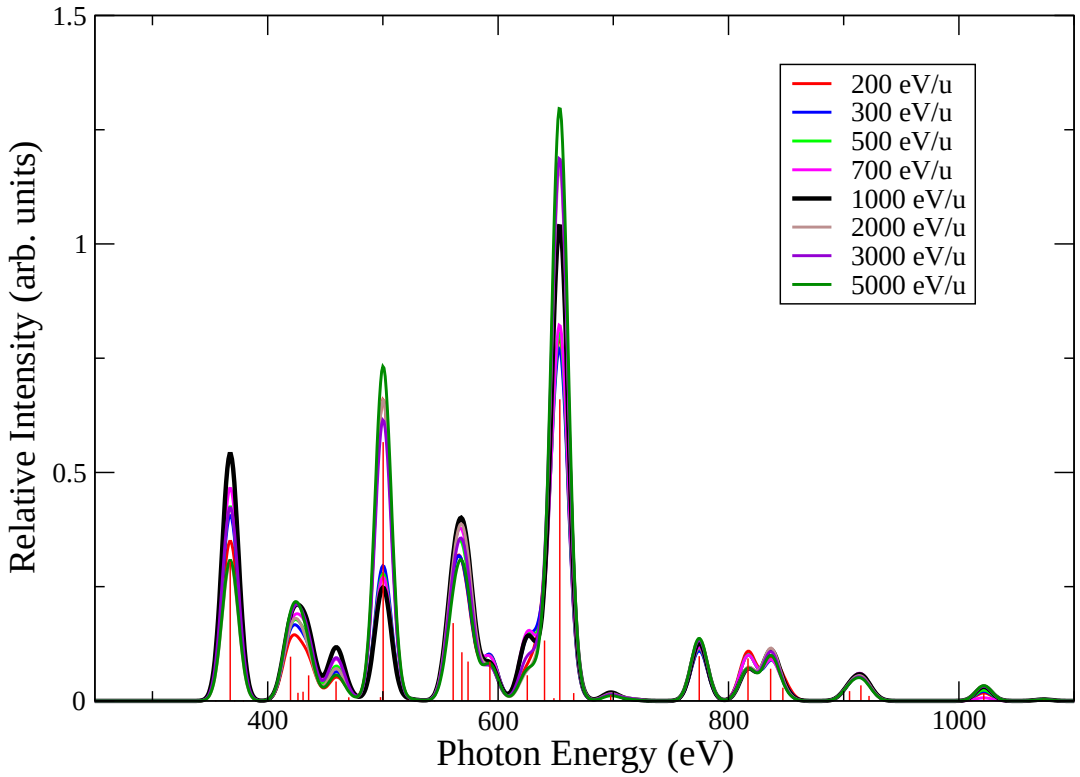

Figure 3.9: CX X-ray emission line ratios for H-like and He-like C-Si ions colliding with H and 10 % fraction of He extracted from *XSPEC* fits, as shown in Figures 3.7 and 3.8 using 10 eV Gaussian FWHM.

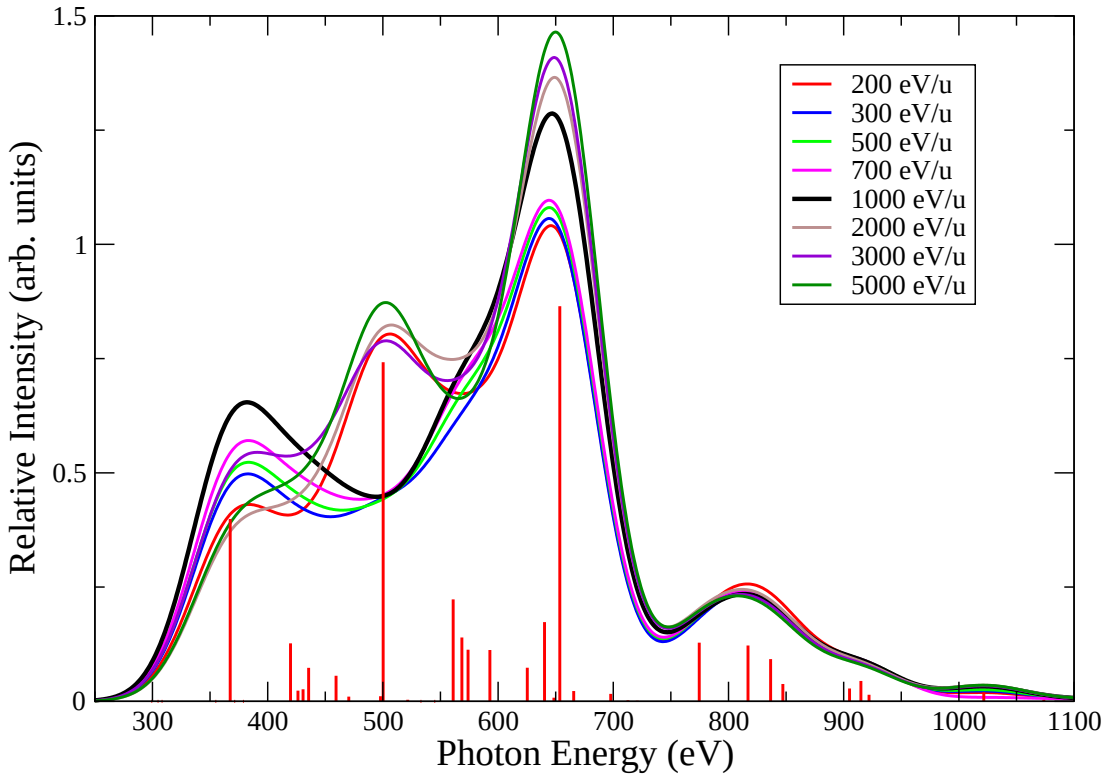

Figure 3.10: Same as Figure 3.9, but using a 50 eV Gaussian FWHM resolution.

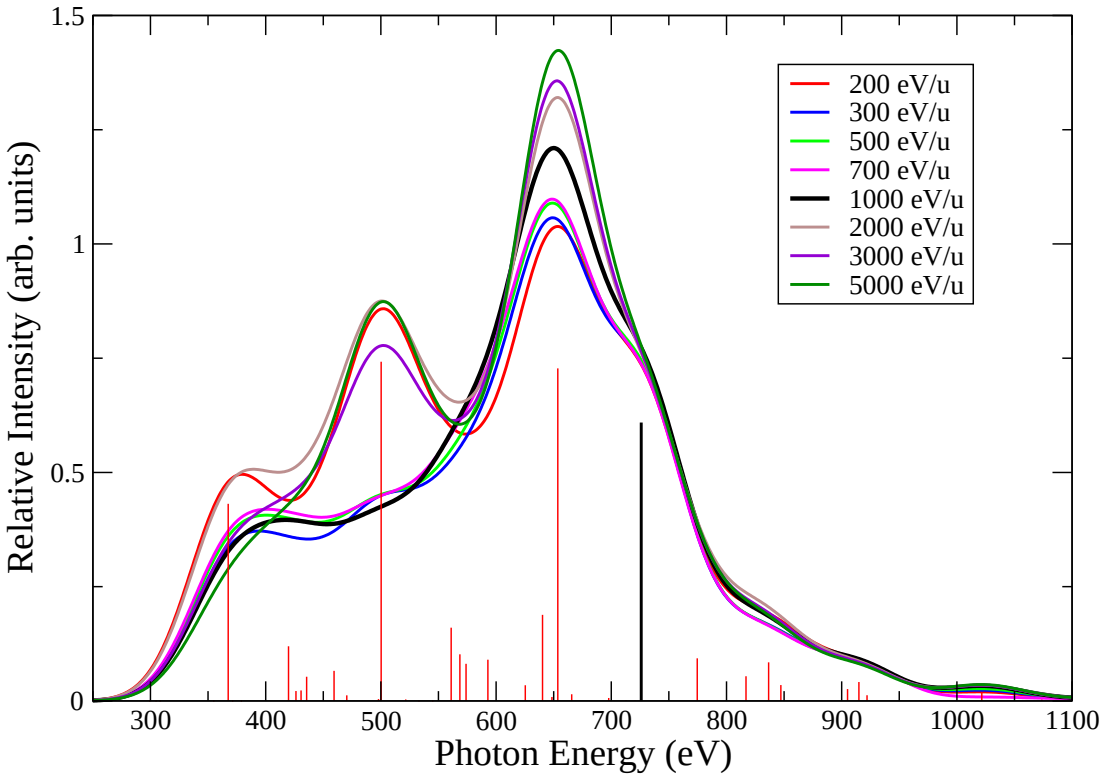

Figure 3.11: Same as Figure 3.10 (using a 50 eV Gaussian FWHM resolution), but including two lines at 0.726 keV and 0.822 keV to mimic Fe L-shell CX emission. The Fe line at 0.726 is shown in black for the collision energy of 200 eV/u.

.

Table 3.3: Abundance ratios (relative to O) for ions in the solar wind.

Ion	Fast Solar Wind	Slow Solar Wind
C^{5+}	0.440	0.210
C^{6+}	0.085	0.318
N^{6+}	0.011	0.058
N^{7+}	0	0.006
O^{6+}	0.970	0.730
O^{7+}	0.030	0.200
O^{8+}	0	0.070

Abundance ratios from Schwadron and Cravens (2000). While O^{6+} abundances are provided in this table to indicate the total abundance of O, they are not included in CX models here.

3.3 Other Line Ratio Comparisons

The solar wind charge exchange mechanism provides an excellent laboratory for comparing theoretical CX calculations to observed astrophysical spectra as it is happening right in our own solar neighborhood. In order to have a realistic solar wind charge exchange model, the ion composition of the solar wind and the neutral composition in the target comet or planet's atmosphere must be considered. The velocities of solar wind ions and densities of the ions and neutrals are also important parameters. The solar wind can roughly be described as having two modes, the fast solar wind at $\sim$ 750 km/s is emitted from coronal holes in the sun near the solar minimum, and the slow solar wind at $\sim$ 400 km/s is emitted from low solar latitudes. While these solar wind modes have different velocities, they also have very different compositions as described by Schwadron and Cravens (2000). The slow solar wind has a higher abundance of various ionization stages while the fast solar wind only contains one bare ion, C^{6+}. The solar wind ion composition includes C through Fe ions, but for ions

other than C, N, and O, the H-like and He-like ionization stages make little to no contribution to the solar wind ion flux.

A limited spectrum of solar wind ions colliding with H and a fraction of 10% He is shown in Figure 3.12, in order to predict a solar wind spectrum that only considers the collisions of H-like and He-like C, N, and O. In this case, the abundance ratios of the ions (relative to O), from Schwadron and Cravens (2000), are shown in Table 3.3. In this scenario, the fast solar wind has the most flux at the lowest energies, while the slow solar wind contributes significantly throughout the entire spectrum. In order for this to be a realistic SWCX model, lower ionization stages including those of heavier elements (e.g., Si, Mg, Ne, etc.) present in the solar wind must be considered and will influence the spectrum below 500 eV. Calculations for these species are to be considered in the future.

The fraction of neutral H compared to neutral He was then varied in order to determine the effect that the neutral He contribution has to the total CX spectrum, as shown in Figure 3.13. In this case, as the fraction of He varied from 0% He (100 % H) to 75% He (25% H), the total intensities of the lines changed, through all energies shown, but particularly at 500 eV. This indicates that it is can be very important to consider the contribution from various neutral targets when considering charge exchange collisions.

3.4 M82

Because the astrophysical environments of present interest contain both neutral H and He, line ratios for the collisions of Ne^{10+}+H (Figure 3.14), He (Figure 3.15), and for the assumed fraction of 90% H and 10% He (Figure 3.15 for the MCLZ calculations) are shown.

For Ne^{10+} CX with H, the MCLZ statistical ℓ-distribution and AOCC line ratios are almost equal at 1 keV/u, and are relatively consistent between 1 and 10 keV/u. The CTMC method is very similar to the AOCC results for the range of 10-50 keV/u considered. The

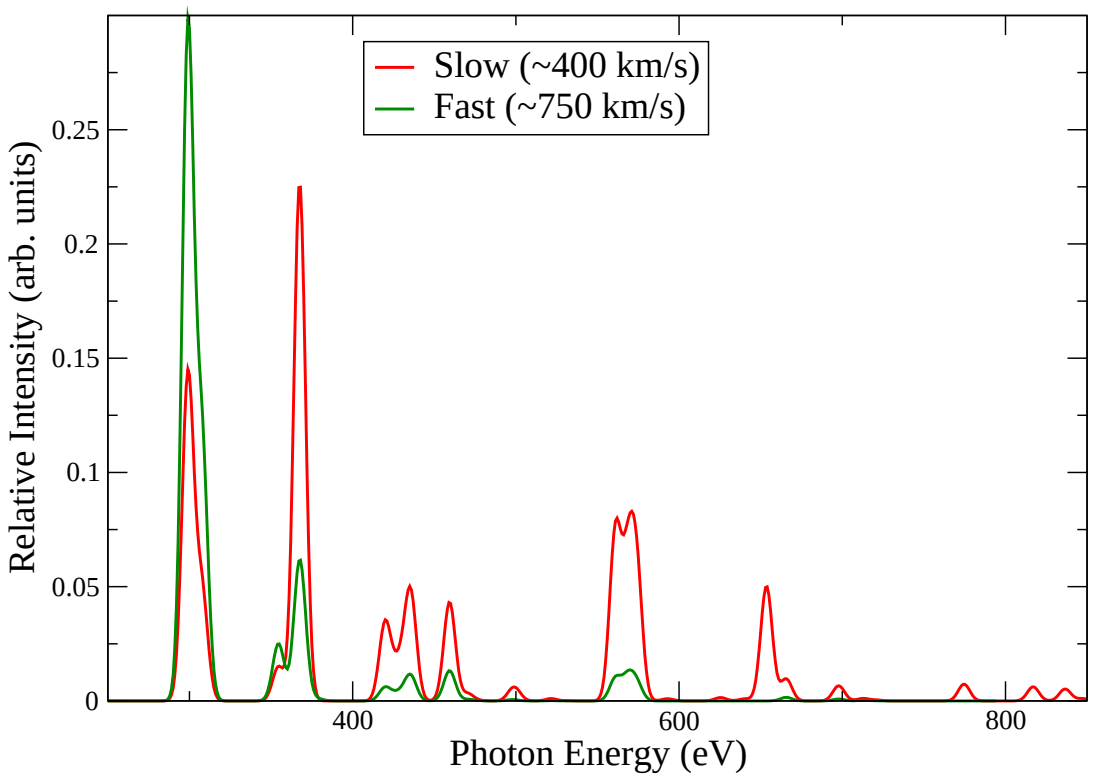

Figure 3.12: Theoretical X-ray emission lines for H-like and He-like C, N, and O ions colliding with H and a fraction of 10% He for the Fast solar wind ($\sim$ 750 km/s) and slow solar wind ($\sim$ 400 km/s). A Gaussian FWHM of 10 eV is used.

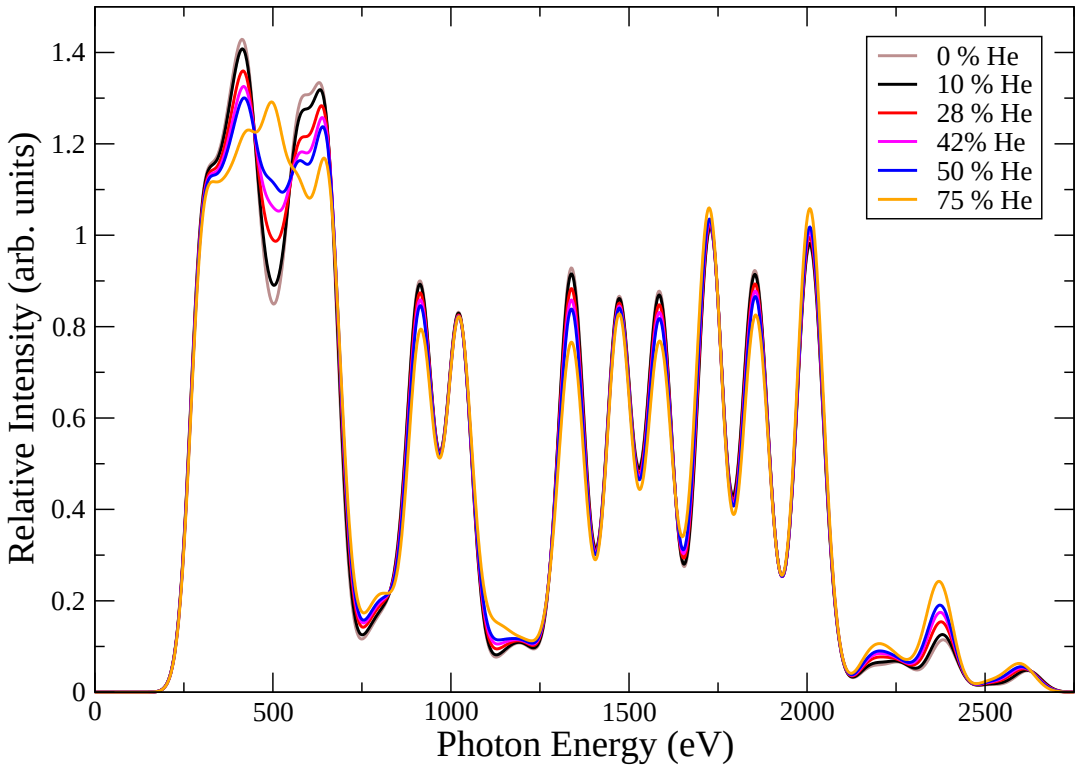

Figure 3.13: Theoretical X-ray emission lines for H-like and He-like C-Si ions colliding at 1 keV/u with H and varying the fraction of He from 0 % He (100 %H) to 75 % He (25 % H). All line-ratio spectra are normalized to a value of 1, and the black line shown with a fraction of 10% He can be compared to the black line shown in Figure 3.6 with the same collision energy. A Gaussian FWHM of 10 eV is used.

MCLZ low energy ℓ-distribution, however, gives a line ratio over an order of magnitude larger than all other methods for the entire energy range. The low energy ℓ-distribution is expected to be more relevant at lower energies than the AOCC or CTMC methods, as suggested in Figure 2.21. However, extending the CTMC method to lower energies, it appears to approach the MCLZ low energy ℓ-distribution for E $\lesssim$ 0.1 keV/u. It can then be postulated that the transition from statistical to low-energy ℓ-distributions occurs between $\sim$0.1 and 1 keV/u making the MCLZ low energy ℓ-distribution relevant at energies less than $\sim$0.5 keV/u.

For Ne^{10+} CX with helium, MCLZ cross sections have been computed in the present work down to low energy ($\sim$100 eV/u) and CTMC results at one impact energy (4.5 keV/u, Ali et al., 2010) are available from previous work, though they could easily be extended to higher and lower energies. These results are shown in Figure 3.15 along with the experimental (Ali et al., 2010) and the AOCC (Liu et al., 2014) results at 4.55 keV/u.

In Figures 3.14-3.15, the Lyβ to Lyα ratios for Ne^{10+} CX with H and He are overlaid with line ratio observations (vertical lines) for M82 from *Suzaku* described by Konami et al. (2011). The observations give the Ne X Lyβ to Lyα ratio for four different regions in M82; the Disk, Wind-1, Wind-2, and Wind-3. In their Figure 8, Konami et al. (2011) showed that the line ratios for the three Wind regions can be reproduced by a collisional ionization equilibrium (CIE) model, but the Disk region cannot. The Lyβ to Lyα ratio from the CIE model is significantly smaller at $\sim$0.1 than the observed Disk line ratio ($\sim$0.25), indicating that the line ratio in the Disk might be primarily due to CX. Assuming that CX has a significant contribution to the spectrum of M82, the collisional energies at which the Lyβ to Lyα line ratios cross the observed line ratio from Konami et al. (2011) gives a constraint on the ion kinetic energy in M82. The Ne IX Kβ line at 1074 eV may partially overlap the observed Ne X Lyα line contaminating the line ratio. The Kβ is expected, however, to account for less than $\sim$5% of the Ne IX emission (see Figure 2.14) and the removal of its contribution would only enhance the Lyβ/Lyα ratio.

Figures 3.14 and 3.15 show that the MCLZ low energy ℓ-distribution line ratios agree with the Disk region observation of Konami et al. (2011), but with reliable CX data similar to that described for the Cygnus Loop in § 3.2.2. The MCLZ low energy ℓ-distribution is over an order of magnitude higher than all other methods for the entire energy range in Figure 3.14, making it fall within the range of the Disk line ratio for M82. As postulated above, the transition from statistical to a low-energy ℓ-distribution occurs between 0.1 and 1 keV/u, because the low energy ℓ-distribution Lyβ to Lyα ratio curve lies within the Disk region uncertainty, we can postulate that the ion kinetic energy in the disk is likely $\lesssim$0.5 keV/u (300 km/s).

In the more unlikely case that all of the atomic H in the Disk region has been ionized leaving only neutral He, Figure 3.15 shows that again the Lyβ/Lyα ratio predicted by the MCLZ cross sections with the low-energy ℓ-distribution gives best agreement. The MCLZ statistical distribution for He predicts line ratios in agreement with the *Suzaku* observation for ion velocities of ∼950-2000 km/s (1-10 keV/u). Likewise, the measurements of Ali et al. (2010) performed at 930 km/s are also consistent with the Disk observation, but these high ion velocities likely cannot be produced in starburst outflows. The CTMC and AOCC He results underestimate the observation by a factor of ∼3 at the energy for which data are available, namely, about 4.5 keV/u, which is considerably larger than the estimated 0.5 keV/u identified above as the likely maximum ion energy that is relevant to CX in the Disk region.

Considering CX from both H and He, but with abundance fractions of 90% and 10%, respectively, again the MCLZ low-energy distribution result agrees best with the observations in the Disk region. For all other methods, He target contributions increase the predicted Lyβ/Lyα ratio, but only to ∼0.1 at 4.55 keV/u (930 km/s).

Using *XMM-Newton* observations with its Reflection Grating Spectrometer (RGS), Zhang et al. (2014) modeled the X-ray spectrum of M82 assuming a two component model con-

sisting of hot single-temperature thermal plasma emission (electron-impact excitation) and CX emission. They found that the Ne X Lyα line intensity can be reproduced if 19% of the emission is due to CX. However, the RGS spectrum covers the entire disk and outflow of M82 (i.e., Disk, Wind-1, Wind-2, and Wind-3 regions of Konami et al., 2011). This is consistent with the suggestion of Konami et al. that the Wind components can be modeled with thermal emission, while the Disk is dominated by CX emission, the latter confirmed here. Further, the CX contribution in Zhang et al. (2014) was obtained with the *ACX* model that adopted the so-called separable ℓ-distribution. The low-energy distribution peaks at $\ell = 1$, while the separable distribution peaks at $\ell = 2$ for Ne^{10+} that results in the *ACX* Lyβ/Lyα ratio of 0.176, shown in Figure 3.14. This line ratio is somewhat smaller than the observed Disk ratio of $\sim$0.28 with *Suzaku*, but consistent with total line ratio of 0.182 Zhang et al. (2014) measured with the RGS. However, one must remember the *XMM-Newton*/RGS measurement includes all regions of the Disk and outflow.

To reproduce the observed Disk Lyβ/Lyα ratio assuming only CX emission, our modeling suggests that the relative ion velocity is $\lesssim$300 km/s, independent of whether a 10% He component is included. While superwind models of the M82 outflow typically adopt velocities greater than 1000 km/s, Zhang et al. (2014) suggest that a reasonable approximation is closer to $\sim$500 km/s. Finally, a further test of the contribution of CX to the X-ray emission could be made by modeling the Lyδ and Lyϵ emission at 1308 and 1325 eV, respectively. Figure 2.19 suggests that both line intensities (for H) are larger than or comparable to that of Lyβ. The Lyϵ to Lyδ ratio could be used to constrain the neutral He to H fraction given the negligible Lyϵ emission for Ne^{10+} + He collisions. In fact, there is some hint of this feature in the CX modeling of Zhang et al. (2014), though blending of the Mg XI Kα forbidden line may contaminate the Ne lines. Higher resolution spectra will better resolve the emission lines and allow for better constraints on the contribution of Ne X CX. A more thorough model, using for example, *XSPEC* (Arnaud, 1996), should be performed including H and He-like C, N, O,

Ne, Mg, and Si and Fe XVII ions colliding with H and He targets, similar to the approach of Zhang et al. (2014), but with reliable CX data. Such a comprehensive approach would help in determining the contribution of various mechanisms including, collisional excitation, radiative recombination, CX, or other processes such as active galactic nuclei (AGN) activity.

3.5 Summary

As shown here via our comparison of results of various conventional theoretical approaches, the MCLZ low-energy ℓ-distribution is likely the better method for producing Ne^{10+} CX line ratios with H and He below 5 keV/u. The statistical distribution may be used above 1 keV/u, but the AOCC method is preferred. As the AOCC and CTMC methods have agreement between 10 and 50 keV/u, either method would work, but as the Lyϵ lines (due to H) are similar for the MCLZ statistical and AOCC methods for this energy, the AOCC approach is likely more accurate. The current charge exchange modeling of the Ne X X-ray emission for the Disk of the starburst galaxy M82 suggests that CX may account for the observed Lyβ/Lyα ratio, a ratio that is not consistent with thermal emission due to electron-impact excitation. Further, the emission may include contributions from CX with neutral H and He suggesting a relative ion velocity of $\lesssim$ 300 km/s. While cross sections obtained with the multichannel Landau-Zener method using the so-called low-energy ℓ-distribution model predicts X-ray line ratios consistent with the observations, calculations using the theoretical method known as the molecular-orbital close-coupling approach, recognized to be among the most complete treatments of ion-atom collisions at low-impact energies, but with significantly greater computational effort and complexity, should be made to confirm these results.

Realistic CX X-ray emission models have been incorporated in an attempt to test the suggestion of Katsuda et al. (2011) that the anomalous X-ray emission near 0.7 keV in the

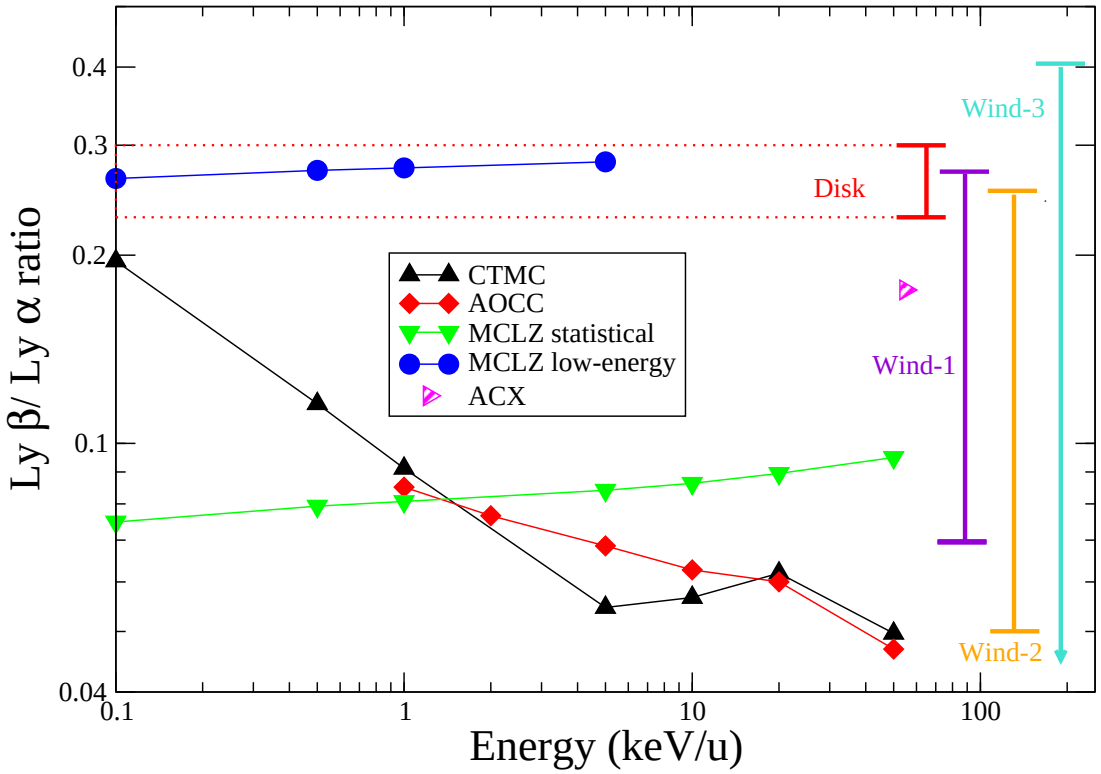

Figure 3.14: Line ratios (Lyβ/Lyα) for the three methods shown in Figures 2.18-2.19 as a function of collisional energy for charge exchange of Ne^{10+} with H. The vertical lines represent the Disk, Wind-1, Wind-2, and Wind-3 regions of M82 as described by Konami et al. (2011). The results from the *ACX* model (Zhang et al., 2014) are also shown. Note that the results from Konami et al. (2011) and Zhang et al. (2014) have no ion kinetic energy dependence and their placement on the right side of the plot is arbitrary.

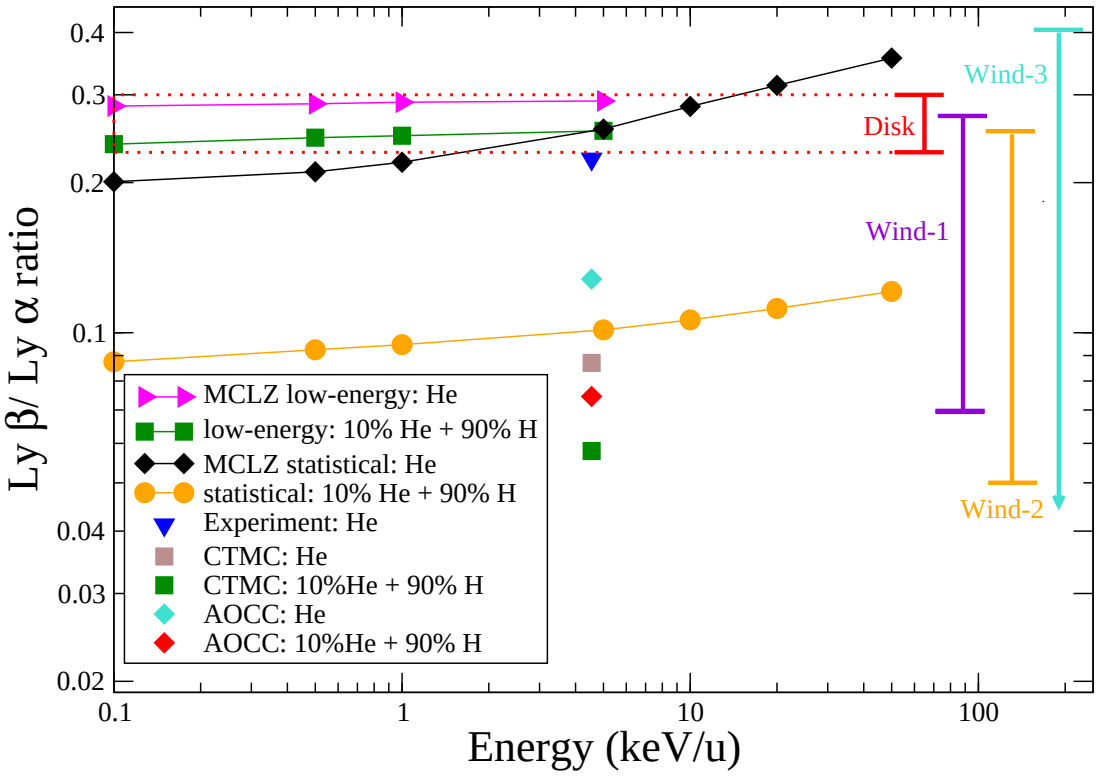

Figure 3.15: Same as Figure 3.14 but for the collision of Ne^{10+} with He. Also shown is the addition Ne^{10+} with 90% H and 10% He, which is the assumed ratio of the He to H charge exchange contributions. CTMC, AOCC, and experimental Ne^{10+} + He data at 4.55 keV/u (see Figure 2.21) are also compared.

Cygnus Loop supernova remnant is due to CX. First, the model included H- and He-like C, N, and O ions colliding with H at 1 keV/u. The model was then improved, including C, N, O, Ne, Mg, Al, and Si ions colliding with H and a fraction of 10 % He. While the initial model provided a better fit than treating the X-ray emission as pure supernova shock emission, including more ionization species did not provide a significant improvement to the previous fit. This model was then performed for 7 other energies, from 200 eV/u to 5000 eV/u, with the best fits occurring at energies above 1 keV/u. With the improved fit compared to the pure supernova shock model, it is likely that CX contributes to the X-ray spectrum of the Cygnus Loop, but CX cannot account for anomalous X-ray emission at 0.7 keV. This X-ray emission may be due to Fe XVII CX and/or emission from a species and/or mechanism not included in the current models.

In conclusion, using accurate CX X-ray emission models for C-Si ions, we confirm that charge exchange may contribute to the X-ray emission observed from a supernova remnant, the Cygnus Loop. However, detailed models to accurately simulate the spectrum to extract physical conditions of the local environment require additional CX studies, particularly for other elements and charge states.

Chapter 4

Summary and Outlook

With the advent of high-resolution X-ray detectors, anomalous X-ray features have been observed in a variety of environments. When the spectra cannot be explained by thermal electron impact or shock models, CX is often invoked, typically without realistic CX data. In this dissertation, CX cross-sections are calculated using the following four methods: QMOCC, AOCC, CTMC, and MCLZ. For collisions with bare ions such as Ne^{10+}, MCLZ calculations are only able to produce n-resolved cross-sections, and an ℓ-distribution must be applied. QMOCC cross sections were used, when available, for the collisions of C^{5+} + H (Nolte et al., 2012), N^{6+} + H (Wu et al., 2011), and O^{7+} + H (Nolte, 2016). AOCC cross-sections were then used for Ne^{10+} + H for energies above 1 keV/u, while MCLZ cross-sections were used for energies below 1 keV/u (Cumbee et al., 2016a). For C^{6+} + He, AOCC cross sections were adopted (Fritsch and Lin, 1991). For C^{6+} + H and O^{8+} + H, recommended cross-sections from Janev et al. (1993) were used, and for N^{7+} +H (Harel et al., 1998), MOCC cross-sections were used. In all other cases, and when energies were missing for other methods, MCLZ cross sections were adopted. For bare-ion MCLZ calculations, the low-energy ℓ-distribution is applied below 1 keV/u, while the statistical distribution is adopted at and above 1 keV/u. All of these cross-sections can be found in the *Kronos*

Database (Mullen et al., 2016b).

It is important to benchmark theoretical calculations to laboratory measurements, when possible, to test the reliability of the theoretical data for various collision energies. In this dissertation, theoretical spectra were compared for the four methods discussed, to experimental spectra for C, Ne, and Fe ions. For C^{6+} collisions with He and H_2, laboratory measurements were compared to spectra produced with theoretical MCLZ statistical ℓ-distribution calculations. While the theoretical spectrum for the collision with H_2 provided a reasonable fit to the experiment, the theoretical spectrum underestimated the Lyβ line for the collision with He. Theoretical spectra were produced for Ne^{10+} and Ne^{9+} collisions with H and He using the AOCC, CTMC, and MCLZ methods. The cross-sections were compared for the dominant capture channel $n = 6$ before comparisons were made to measurements for Ne^{10+} with He. In this case, the MCLZ calculations, both the statistical and low energy ℓ-distributions provided the best fit. For Fe^{25+} and Fe^{26+} collisions with N_2, comparisons were also made to laboratory measurements. While the MCLZ calculations provided a reasonable fit for the Fe^{25+} collision, for the Fe^{26+} collision, the MCLZ low-energy ℓ distribution was not able to adequately fit the spectrum, so a modified distribution, the MCLZSL1 distribution, was applied, that which resulted in a reasonable fit.

X-ray hardness ratios were then shown for CX collisions with H-like and He-like C, N, O, Ne, Mg, Al, and Si collisions with H in order to highlight the velocity dependence for the ion-neutral collisions calculated here. In general, all hardness ratios varied depending on the collision energy, but QMOCC and recommended hardness ratios show a more intense variation than those calculated with the MCLZ method. The ratio of the Lyβ/α and Kβ/α resonant lines can also be quite distinctive for the collisional process considered. The Kβ/α ratios were shown for Fe^{25+} CX with CO, H_2O, He, H_2, and N_2 to show that the neutral target can have a significant impact on the relative intensity of the Kβ line. Lyβ/α line ratios were then shown for Ne^{10+} for the AOCC, CTMC, and MCLZ methods in order to

compare to ratios observed in the starburst galaxy, M82. It was found that CX may account for the observed Lyβ/Lyα ratio of the Disk region of M82, which has a ratio that is not consistent with thermal emission due to electron-impact excitation. Further, the emission may include contributions from CX with neutral H and He suggesting a relative ion velocity of $\lesssim 300$ km/s. While cross sections obtained with the MCLZ method using the low-energy ℓ-distribution predicts X-ray line ratios consistent with the observations, calculations using the QMOCC method should be made to confirm these results.

A CX X-ray emission model was then applied to *Suzaku* observations of the Cygnus Loop, a supernova remnant in which Katsuda et al. (2011) observed anomalous X-ray emission. This *XSPEC* model included the appropriate background model and supernova shock model (VpShock), but was modified by applying CX line ratios for H-like and He-like C, N, and O collisions with H. Realistic CX X-ray emission lines were incoprorated in an attempt to test the suggestion of Katsuda et al. (2011) that the anomalous X-ray emission near 0.7 keV in the Cygnus Loop is due to CX. While the model was not able to provide a perfect fit to the spectrum, it was shown that charge exchange likely contributes to the X-ray spectrum. Katsuda et al. (2011) suggested that high order O VII emission lines due to O^{7+} + H CX contribute to the 0.7 keV spectral features, however the O VII line intensities constrained by CX emission models were insufficient to fully account for the 0.7 keV X-ray flux.

Finally, updated *XSPEC* charge exchange models of the Cygnus Loop were performed including more ions, targets, and collision energies. H- and He-like C, N, O, Ne, Mg, Al, and Si collisions with H and a 10% fraction of He were considered for collision energies from 200 eV/u ($\sim$ 200 km/s) to 5 keV/u ($\sim$ 1000 km/s). The best available cross-sections were chosen for each collision energy. While it is important to consider all ions and ionization stages that might be present in an astrophysical environment in a CX model, including more CX collisions of Ne, Mg, Al, and Si with a He target did not result in a significantly better fit to the Cygnus Loop spectrum. Considering collisions of various velocities did however

provide more insight into the Cygnus Loop spectrum. Collision energies below 1 keV/u provided a worse fit compared to energies above 1 keV/u, while the collision energies of 1 keV/u and 2 keV/u provided the best fits.

The X-ray observatory *Athena*, scheduled to launch in 2028, will have onboard an X-ray Microcalorimeter Spectrometer that will provide high resolution X-ray spectra which will better resolve X-ray emission lines, specifically the Kα transitions of helium-like ions which are highly diagnostic of CX. With higher resolution spectra, it is important to have reliable CX models for all relevant ion and neutral interactions and kinetic energies. In general, more CX collisions with other ionization stages and neutral targets need to be studied to produce a realistic CX model. In the future, I will use the most reliable CX cross sections, perform additional cross section calculations, and prepare models to enhance current $n \rightarrow n' = 1$ K-shell CX emission models and extend such models to the $n \rightarrow n' = 2$ L-shell. Until high-resolution microcalorimeter data are available (such as that from *Athena*), the CX model will be applied to archival data of supernova remnants and nearby star forming galaxies. When the microcalorimeter data become available, it will be a true test of the reliability of this CX model.

Bibliography

Abramov, V., Baryshnikov, F., and Lisitsa, V. (1978). Charge transfer between hydrogen atoms and the nuclei of multicharged ions with allowance for the degeneracy of the final states. *Sov. Phys.-JETP (Engl. Transl.);(United States)*, 47(3).

Abrines, R. and Percival, I. C. (1966). Classical theory of charge transfer and ionization of hydrogen atoms by protons. *Proceedings of the Physical Society*, 88(4):861.

Ali, R., Beiersdorfer, P., Harris, C. L., and Neill, P. A. (2016). Charge-exchange x-ray spectra: Evidence for significant contributions from radiative decays of doubly excited states. *Phys. Rev. A*, 93:012711.

Ali, R., Neill, P., Beiersdorfer, P., Harris, C., Schultz, D. R., and Stancil, P. C. (2010). Critical Test of Simulations of Charge-exchange-induced X-ray Emission in the Solar System. *The Astrophysical Journal Letters*, 716(2):L95.

Ali, R., Neill, P. A., Beiersdorfer, P., Harris, C. L., Raković, M. J., Wang, J. G., Schultz, D. R., and Stancil, P. C. (2005). On the Significance of the Contribution of Multiple-Electron Capture Processes to Cometary X-Ray Emission. *The Astrophysical Journal Letters*, 629(2):L125.

Arnaud, K. A. (1996). XSPEC: The first ten years. In Jacoby, G. H. and Barnes, J., editors,

Astronomical Data Analysis Software and Systems V, volume 101 of *ASP Conference Series*, page 17.

Becker, R. and MacKellar, A. (1984). Theoretical initial l dependence of ion-Rydberg-atom collision cross sections. *Journal of Physics B: Atomic and Molecular Physics*, 17(19):3923.

Beiersdorfer, P., Boyce, K., Brown, G., Chen, H., Kahn, S., Kelley, R., May, M., Olson, R., Porter, F., Stahle, C., et al. (2003). Laboratory simulation of charge exchange-produced X-ray emission from comets. *Science*, 300(5625):1558–1559.

Beiersdorfer, P., Lisse, C. M., Olson, R. E., Brown, G. V., and Chen, H. (2001). X-Ray Velocimetry of Solar Wind Ion Impact on Comets. *The Astrophysical Journal Letters*, 549(1):L147.

Bodewits, D., Christian, D., Torney, M., Dryer, M., Lisse, C., Dennerl, K., Zurbuchen, T., Wolk, S., Tielens, A., and Hoekstra, R. (2007). Spectral analysis of the Chandra comet survey. *Astronomy & Astrophysics*, 469(3):1183–1195.

Butler, S. and Dalgarno, A. (1980). Charge transfer of multiply charged ions with hydrogen and helium Landau-Zener calculations. *The Astrophysical Journal*, 241:838–843.

Cox, D. P. (1998). The Local Bubble and Beyond Lyman-Spitzer-Colloquium: Proceedings of the IAU Colloquium No. 166 Held in Garching, Germany, 21–25 April 1997. In Breitschwerdt, D., Freyberg, M., and Trümper, J., editors, *Lecture Notes in Physics*, pages 121–131, Berlin, Heidelberg. Springer.

Cravens, T. E. (1997). Comet Hyakutake X-ray source: Charge transfer of solar wind heavy ions. *Geophysical Research Letters*, 24(1):105–108.

Cravens, T. E., Waite, J. H., Gombosi, T. I., Lugaz, N., Gladstone, G. R., Mauk, B. H., and MacDowall, R. J. (2003). Implications of Jovian X-ray emission for magnetosphere-

ionosphere coupling. *Journal of Geophysical Research: Space Physics*, 108(A12):n/a–n/a. 1465.

Crowder, S. G., Barger, K. A., Brandl, D. E., Eckart, M. E., Galeazzi, M., Kelley, R. L., Kilbourne, C. A., McCammon, D., Pfendner, C. G., Porter, F. S., Rocks, L., Szymkowiak, A. E., and Teplin, I. M. (2012). Observed Limits on Charge Exchange Contributions to the Diffuse X-Ray Background. *The Astrophysical Journal*, 758(2):143.

Cumbee, R. S., Henley, D. B., Stancil, P. C., Shelton, R. L., Nolte, J. L., Wu, Y., and Schultz, D. R. (2014). Can Charge Exchange Explain Anomalous Soft X-Ray Emission in the Cygnus Loop? *The Astrophysical Journal Letters*, 787(2):L31.

Cumbee, R. S., Liu, L., Lyons, D., Schultz, D. R., Stancil, P. C., Wang, J. G., and Ali, R. (2016a). Ne X X-ray Emission due to Charge Exchange in M82. *Monthly Notices of the Royal Astronomical Society*.

Cumbee, R. S., Mullen, P., Lyons, D., Shelton, R. L., Fogle, M., Schultz, D. R., and Stancil, P. C. (2016b). Charge Exchange X-ray Emission due to Collisions with H, He, and H_2: line ratios for heliospheric and interstellar applications. CX Line Ratios.

Defay, X., Morgan, K., McCammon, D., Wulf, D., Andrianarijaona, V., Fogle, M., Seely, D., Draganić, I., and Havener, C. C. (2013). X-ray emission measurements following charge exchange between C 6+ and He. *Physical Review A*, 88(5):052702.

Dennerl, K. (2006). X-Rays From Mars. *Space Science Reviews*, 126(1):403–433.

Dennerl, K. (2010). Charge Transfer Reactions. *Space Science Reviews*, 157(1):57–91.

Dennerl, K., Burwitz, V., Englhauser, J., Lisse, C., and Wolk, S. (2002). Discovery of X–rays from Venus with Chandra. *Astronomy & Astrophysics*, 386(1):319–330.

Ewing, I., Christian, D. J., Bodewits, D., Dennerl, K., Lisse, C. M., and Wolk, S. J. (2013). Emission Lines between 1 and 2 keV in Cometary X-Ray Spectra. *The Astrophysical Journal*, 763(1):66.

Fogle, M., Wulf, D., Morgan, K., McCammon, D., Seely, D. G., Draganić, I. N., and Havener, C. C. (2014). X-ray-emission measurements following charge exchange between C^{6+} and H_2. *Phys. Rev. A*, 89:042705.

Fritsch, W. and Lin, C. D. (1991). The semiclassical close-coupling description of atomic collisions: Recent developments and results. *Physics Reports*, 202(1):1–97.

Fujimoto, R., Mitsuda, K., McCammon, D., Takei, Y., Bauer, M., Ishisaki, Y., Porter, F. S., Yamaguchi, H., Hayashida, K., and Yamasaki, N. Y. (2007). Evidence for Solar-Wind Charge-Exchange X-Ray Emission from the Earth's Magnetosheath. *Publications of the Astronomical Society of Japan*, 59(sp1):S133–S140.

Garvey, R. H., Jackman, C. H., and Green, A. E. S. (1975). Independent-particle-model potentials for atoms and ions with $36 < z < 54$ and a modified Thomas-Fermi atomic energy formula. *Phys. Rev. A*, 12:1144–1152.

Ghavamian, P., Raymond, J., Smith, R. C., and Hartigan, P. (2001). Balmer-dominated Spectra of Nonradiative Shocks in the Cygnus Loop, RCW 86, and Tycho Supernova Remnants. *The Astrophysical Journal*, 547(2):995.

Green, A. E. S., Sellin, D. L., and Zachor, A. S. (1969). Analytic Independent-Particle Model for Atoms. *Phys. Rev.*, 184:1–9.

Greenwood, J. B., Williams, I. D., Smith, S. J., and Chutjian, A. (2001). Experimental investigation of the processes determining x-ray emission intensities from charge-exchange collisions. *Phys. Rev. A*, 63:062707.

Gu, L., Kaastra, J., and Raassen, A. (2016). Plasma code for astrophysical charge exchange emission at X-ray wavelengths. *Astronomy & Astrophysics*, 588:A52.

Harel, C., Jouin, H., and Pons, B. (1998). Cross sections for electron capture from atomic hydrogen by fully stripped ions in the 0.05–1.00 a.u. impact velocity range. *Atomic Data and Nuclear Data Tables*, 68(2):279 – 302.

Hasan, A. A., Eissa, F., Ali, R., Schultz, D. R., and Stancil, P. C. (2001). State-selective Charge Transfer Studies Relevant to Solar Wind-Comet Interactions. *The Astrophysical Journal Letters*, 560(2):L201.

Henley, D. B., Shelton, R. L., Cumbee, R. S., and Stancil, P. C. (2015a). XMM-Newton Measurement of the Galactic Halo X-Ray Emission using a Compact Shadowing Cloud. *The Astrophysical Journal*, 799(2):117.

Henley, D. B., Shelton, R. L., Kwak, K., Hill, A. S., and Low, M.-M. M. (2015b). The Origin of the Hot Gas in the Galactic Halo: Testing Galactic Fountain Models' X-Ray Emission. *The Astrophysical Journal*, 800(2):102.

Holmström, M., Barabash, S., and Kallio, E. (2001). X-ray imaging of the solar wind—Mars interaction. *Geophysical Research Letters*, 28(7):1287–1290.

Horanyi, M., Cravens, T. E., and Waite, J. H. (1988). The precipitation of energetic heavy ions into the upper atmosphere of Jupiter. *Journal of Geophysical Research: Space Physics*, 93(A7):7251–7271.

Hui, Y., Schultz, D. R., Kharchenko, V. A., Stancil, P. C., Cravens, T. E., Lisse, C. M., and Dalgarno, A. (2009). The Ion-induced Charge-exchange X-ray Emission of the Jovian Auroras: Magnetospheric or Solar Wind Origin? *The Astrophysical Journal Letters*, 702(2):L158.

Ishisaki, Y., Maeda, Y., Fujimoto, R., Ozaki, M., Ebisawa, K., Takahashi, T., Ueda, Y., Ogasaka, Y., Ptak, A., Mukai, K., Hamaguchi, K., Hirayama, M., Kotani, T., Kubo, H., Shibata, R., Ebara, M., Furuzawa, A., Iizuka, R., Inoue, H., Mori, H., Okada, S., Yokoyama, Y., Matsumoto, H., Nakajima, H., Yamaguchi, H., Anabuki, N., Tawa, N., Nagai, M., Katsuda, S., Hayashida, K., Bamba, A., Miller, E. D., Sato, K., and Yamasaki, N. Y. (2007). Monte Carlo Simulator and Ancillary Response Generator of Suzaku XRT/XIS System for Spatially Extended Source Analysis. *Publications of the Astronomical Society of Japan*, 59(sp1):S113–S132.

Janev, R., Phaneuf, R., Tawara, H., and Shirai, T. (1993). Recommended Cross Sections for State-Selective Electron Capture in Collisions of C6+ and O8+ Ions with Atomic Hydrogen. *Atomic Data and Nuclear Data Tables*, 55(2):201 – 232.

Janev, R. K., Belić, D. S., and Bransden, B. H. (1983). Total and partial cross sections for electron capture in collisions of hydrogen atoms with fully stripped ions. *Phys. Rev. A*, 28:1293–1302.

Kalberla, P. M. W., Burton, W. B., Hartmann, Dap, Arnal, E. M., Bajaja, E., Morras, R., and PÃppel, W. G. L. (2005). The Leiden/Argentine/Bonn (LAB) Survey of Galactic HI. *Astronomy & Astrophysics*, 440(2):775–782.

Katsuda, S., Tsunemi, H., Mori, K., Uchida, H., Kosugi, H., Kimura, M., Nakajima, H., Takakura, S., Petre, R., Hewitt, J. W., and Yamaguchi, H. (2011). Possible Charge-exchange X-ray Emission in the Cygnus Loop Detected with Suzaku. *The Astrophysical Journal*, 730(1):24.

Katsuda, S., Tsunemi, H., Mori, K., Uchida, H., Petre, R., Yamada, S., Akamatsu, H., Konami, S., and Tamagawa, T. (2012). High-resolution X-Ray Spectroscopy of the Galac-

tic Supernova Remnant Puppis A with XMM-Newton/RGS. *The Astrophysical Journal*, 756(1):49.

Kharchenko, V., Bhardwaj, A., Dalgarno, A., Schultz, D. R., and Stancil, P. C. (2008). Modeling spectra of the north and south Jovian X-ray auroras. *Journal of Geophysical Research: Space Physics*, 113(A8):n/a–n/a. A08229.

Kharchenko, V. and Dalgarno, A. (2000). Spectra of cometary X rays induced by solar wind ions. *Journal of Geophysical Research: Space Physics*, 105(A8):18351–18359.

Kimura, M. and Lane, N. F. (1989). The Low-Energy, Heavy-Particle CollisionsâA Close-Coupling Treatment*. In Bates, S. D. and Bederson, B., editors, *Advances In Atomic, Molecular, and Optical Physics*, volume 26 of *Advances In Atomic, Molecular, and Optical Physics*, pages 79 – 160. Academic Press.

Konami, S., Matsushita, K., Go Tsuru, T., Gandhi, P., and Tamagawa, T. (2011). Suzaku Metal Abundance Patterns in the Outflow Region of M 82 and the Importance of Charge Exchange. *Publications of the Astronomical Society of Japan*, 63(sp3):S913–S924.

Kosugi, H., Tsunemi, H., Katsuda, S., Uchida, H., and Kimura, M. (2010). Suzaku Observation of the Southeastern Rim of the Cygnus Loop. *Publications of the Astronomical Society of Japan*, 62(4):1035–1044.

Krasnopolsky, V. A., Greenwood, J. B., and Stancil, P. C. (2004). X-Ray and extreme ultraviolet emissions from comets. *Space Science Reviews*, 113(3):271–374.

Kuang, J. and Lin, C. D. (1996). On the convergence of the two-centre AO close-coupling method in ion - atom collisions. *Journal of Physics B: Atomic, Molecular and Optical Physics*, 29(6):1207.

Kuang, J. and Lin, C. D. (1997). Convergent TCAO close-coupling calculations for electron transfer, excitation and ionization in intermediate keV. *Journal of Physics B: Atomic, Molecular and Optical Physics*, 30(1):101.

Lallement, R. (2004). On the contribution of charge-exchange induced X-ray emission in the ISM and ICM. *Astronomy & Astrophysics*, 422(2):391–400.

Lisse, C., Christian, D., Dennerl, K., Meech, K., Petre, R., Weaver, H., and Wolk, S. (2001). Charge exchange-induced X-ray emission from Comet C/1999 S4 (LINEAR). *Science*, 292(5520):1343–1348.

Lisse, C. M., Dennerl, K., Englhauser, J., Harden, M., Marshall, F. E., Mumma, M. J., Petre, R., Pye, J. P., Ricketts, M. J., Schmitt, J., Trümper, J., and West, R. G. (1996). Discovery of X-ray and Extreme Ultraviolet Emission from Comet C/Hyakutake 1996 B2. *Science*, 274(5285):205–209.

Liu, J., Mao, S., and Wang, Q. D. (2011). Charge-exchange X-ray emission of M82: Ka triplets of OVII, Ne IX and Mg XI. *Monthly Notices of the Royal Astronomical Society: Letters*, 415(1):L64–L68.

Liu, J., Wang, Q. D., and Mao, S. (2012). Charge Exchange X-ray Emission of Nearby Star-forming Galaxies Charge Exchange X-ray Emission of Nearby Star-forming Galaxies. *Mon. Not. R. Astron. Soc.*, 420:3389–3395.

Liu, L., Wang, J. G., and Janev, R. K. (2014). Charge-transfer-induced X-ray spectra in collisions of Ne^{10+} with He and Ne atoms. *Phys. Rev. A*, 89:012710.

Lyons, D., Cumbee, R. S., , and Stancil, P. C. (2016). Charge exchang of highly-charged Ne and Mg ions with H and He. *Astrophysical J. Supplement*.

Markevitch, M., Bautz, M. W., Biller, B., Butt, Y., Edgar, R., Gaetz, T., Garmire, G., Grant, C. E., Green, P., Juda, M., Plucinsky, P. P., Schwartz, D., Smith, R., Vikhlinin, A., Virani, S., Wargelin, B. J., and Wolk, S. (2003). Chandra Spectra of the Soft X-Ray Diffuse Background. *The Astrophysical Journal*, 583(1):70.

McCammon, D., Almy, R., Apodaca, E. e. . a., Tiest, W. B., Cui, W., Deiker, S., Galeazzi, M., Juda, M., Lesser, A., Mihara, T., et al. (2002). A high spectral resolution observation of the soft X-ray diffuse background with thermal detectors. *The Astrophysical Journal*, 576(1):188.

McCammon, D. and Sanders, W. T. (1990). The soft X-ray background and its origins. *Annual Review of Astronomy and Astrophysics*, 28:657–688.

Mullen, P., Cumbee, R., Lyons, D., Gu, L., Kaastra, J., Shelton, R., and P.C.Stancil (2016a). Line Ratios for Solar Wind Charge Exchange with Comets. CX Line Ratios.

Mullen, P. D., Cumbee, R. S., Lyons, D., and Stancil, P. C. (2016b). Charge Exchange-induced X-Ray Emission of Fe xxv and Fe xxvI via a Streamlined Model. *The Astrophysical Journal Supplement Series*, 224(2):31.

Nolte, J. (2011). *Computational Studies of Atomic, Ionic, and Molecular Scattering*. PhD thesis, The University of Georgia.

Nolte, J. L., Stancil, P. C., Liebermann, H. P., Buenker, R. J., Hui, Y., and Schultz, D. R. (2012). Final-state-resolved charge exchange in C 5 + collisions with H. *Journal of Physics B: Atomic, Molecular and Optical Physics*, 45(24):245202.

Nolte, J. Stancil, P. S. e. a. (2016). He-like O Cross-sections. In Preparation.

Olson, R. (2006). *Springer Handbook of Atomic, Molecular, and Optical Physics*, chapter

Classical Trajectory and Monte Carlo Techniques, pages 869–874. Springer New York, New York, NY.

Olson, R. E. and Salop, A. (1976). Electron transfer between multicharged ions and neutral species. *Phys. Rev. A*, 14:579–585.

Olson, R. E. and Salop, A. (1977). Charge-transfer and impact-ionization cross sections for fully and partially stripped positive ions colliding with atomic hydrogen. *Phys. Rev. A*, 16:531–541.

Reeves, C. (1963). Use of Gaussian functions in the calculation of wavefunctions for small molecules. I. Preliminary investigations. *The Journal of Chemical Physics*, 39(1):1–10.

Rigazio, M., Kharchenko, V., and Dalgarno, A. (2002). X-ray emission spectra induced by hydrogenic ions in charge transfer collisions. *Phys. Rev. A*, 66:064701.

Robertson, I., Cravens, T., Snowden, S., and Linde, T. (2001). Temporal and Spatial Variations of Heliospheric x-ray Emissions Associated with Charge Transfer of the Solar Wind with Interstellar Neutrals. *Space Science Reviews*, 97(1):401–405.

Schultz, D. and Krstic, P. (1995). Inelastic processes in 0.1-1000 keV/u collisions of Ne $\rightarrow +$ $(q = 7 - 10)$ ions with atomic hydrogen. *Nuclear Fusion*, page 173.

Schwadron, N. A. and Cravens, T. E. (2000). Implications of Solar Wind Composition for Cometary X-Rays. *The Astrophysical Journal*, 544(1):558.

Smith, R., Foster, A., and Brickhouse, N. (2012). Approximating the X-ray spectrum emitted from astrophysical charge exchange. *Astronomische Nachrichten*, 333(4):301–304.

Smith, R. K., Foster, A. R., Edgar, R. J., and Brickhouse, N. S. (2014). Resolving the Origin of the Diffuse Soft X-Ray Background. *The Astrophysical Journal*, 787(1):77.

Snios, B., Kharchenko, V., Lisse, C. M., Wolk, S. J., Dennerl, K., and Combi, M. R. (2016). Chandra Observations of Comets C/2012 S1 (ISON) and C/2011 L4 (PanSTARRS). *The Astrophysical Journal*, 818(2):199.

Snowden, S. L., Collier, M. R., and Kuntz, K. D. (2004). XMM-Newton Observation of Solar Wind Charge Exchange Emission. *The Astrophysical Journal*, 610(2):1182.

Snowden, S. L., Egger, R., Finkbeiner, D. P., Freyberg, M. J., and Plucinsky, P. P. (1998). Progress on Establishing the Spatial Distribution of Material Responsible for the 1/4 keV Soft X-Ray Diffuse Background Local and Halo Components. *The Astrophysical Journal*, 493(2):715.

Taulbjerg, K. (1986). Reaction windows for electron capture by highly charged ions. *Journal of Physics B: Atomic and Molecular Physics*, 19(10):L367.

Tawa, N., Hayashida, K., Nagai, M., Nakamoto, H., Tsunemi, H., Yamaguchi, H., Ishisaki, Y., Miller, E. D., Mizuno, T., Dotani, T., Ozaki, M., and Katayama, H. (2008). Reproducibility of Non-X-Ray Background for the X-Ray Imaging Spectrometer aboard Suzaku. *Publications of the Astronomical Society of Japan*, 60(sp1):S11–S24.

Von Neumann, J. and Wigner, E. (1929). No crossing rule. *Z. Phys*, 30:467–470.

Wargelin, B. J., Beiersdorfer, P., Neill, P. A., Olson, R. E., and Scofield, J. H. (2005). Charge-Exchange Spectra of Hydrogenic and He-like Iron. *The Astrophysical Journal*, 634(1):687.

Wargelin, B. J., Markevitch, M., Juda, M., Kharchenko, V., Edgar, R., and Dalgarno, A. (2004). Chandra Observations of the "Dark" Moon and Geocoronal Solar Wind Charge Transfer. *The Astrophysical Journal*, 607(1):596.

Wu, Y., Stancil, P. C., Liebermann, H. P., Funke, P., Rai, S. N., Buenker, R. J., Schultz, D. R., Hui, Y., Draganic, I. N., and Havener, C. C. (2011). Theoretical investigation of charge transfer between N^{6+} and atomic hydrogen. *Phys. Rev. A*, 84:022711.

Yoshino, T., Mitsuda, K., Yamasaki, N. Y., Takei, Y., Hagihara, T., Masui, K., Bauer, M., McCammon, D., Fujimoto, R., Daniel Wang, Q., and Yao, Y. (2009). Energy Spectra of the Soft X-Ray Diffuse Emission in Fourteen Fields Observed with Suzaku. *Publications of the Astronomical Society of Japan*, 61(4):805–823.

Zhang, S., Wang, Q. D., Ji, L., Smith, R. K., Foster, A. R., and Zhou, X. (2014). Spectral Modeling of the Charge-exchange X-Ray Emission from M82. *The Astrophysical Journal*, 794(1):61.

Zygelman, B., Cooper, D. L., Ford, M. J., Dalgarno, A., Gerratt, J., and Raimondi, M. (1992). Charge transfer of N^{4+} with atomic hydrogen. *Phys. Rev. A*, 46:3846–3854.

Appendix A

Table A.1: Model Line Normalizations

Line	Energy	CX-Inspired (Fig 3.4)	CX (Fig 3.3)	CX with Fe (Fig 3.5)
	(keV)	(L.U.)	(L.U.)	(L.U.)
(1)	(2)	(3)	(4)	(5)
C^{5+} +H Kα	0.3079	$2.8\times10^{-13}\ ^{+3000.4}_{-0.0}$	$6.9\times10^{-14}\ ^{+52.6}_{-0.0}$	$7.0\times10^{-14}\ ^{+68.1}_{-0.0}$
C^{5+} +H Kβ	0.3545	$1.0\times10^{-13}\ ^{+130.2}_{-0.0}$	2.5×10^{-14}	2.5×10^{-14}
C^{5+} +H Kγ	0.3709	$66.2\ ^{+25.3}_{-66.2}$	4.3×10^{-15}	4.3×10^{-15}
C^{6+} +H Lyα	0.3673	$1.0\times10^{-13}\ ^{+120.1}_{-0.0}$	$73.27\ ^{+98.41}_{-70.05}$	$128.7\ ^{+130.4}_{-80.6}$
C^{6+} +H Lyβ	0.4353	$193.9\ ^{+2564.2}_{-0.0}$	10.83	19.02
C^{6+} +H Lyγ	0.4591	$165.2\ ^{+55.8}_{-91.7}$	16.75	29.41
C^{6+} +H Lyδ	0.4701	$45.60\ ^{+102.07}_{-39.67}$	1.026	1.801
N^{6+} +H Kα f	0.4197	$39.54\ ^{+158.24}_{-11.7}$	$265.1\ ^{+42.0}_{-20.2}$	$246.7\ ^{+27.6}_{-44.2}$
N^{6+} +H Kα i	0.4261	$49.89\ ^{+2702.12}_{-4.09}$	143.2	133.3
N^{6+} +H Kα r	0.4307	$115.3\ ^{+2669.3}_{-2.3}$	111.2	103.5
N^{6+} +H Kβ	0.4979	$7.3\times10^{-12}\ ^{+31.24}_{-0.0}$	20.32	18.91
N^{6+} +H Kγ	0.5215	$217.8\ ^{+35.51}_{-65.17}$	10.98	10.22
O^{7+} +H Kα f	0.5609	$471.8\ ^{+70.3}_{-119.5}$	$338.5\ ^{+18.2}_{-23.7}$	$282.0\ ^{+12.8}_{-23.5}$
O^{7+} +H Kα i	0.5684	$30.4\ ^{+128.7}_{-30.4}$	222.9	185.7
O^{7+} +H Kα r	0.574	$2.7\times10^{-14}\ ^{+109.1}_{-0.0}$	301.1	250.8
O^{7+} +H Kβ	0.6656	$200.3\ ^{+78.6}_{-41.4}$	60.69	50.55
O^{7+} +H Kγ	0.6978	$18.61\ ^{+52.8}_{-1.57}$	21.83	18.18
O^{7+} +H Kδ	0.7127	$46.18\ ^{+33.11}_{-3.56}$	7.659	6.380
O^{7+} +H Kϵ	0.7208	$181.5\ ^{+14.5}_{-29.6}$	3.649	3.040
O^{8+} +H Lyα	0.653	$469.7\ ^{+63.5}_{-12.9}$	$614.2\ ^{+13.9}_{-21.9}$	$553.7\ ^{+22.9}_{-29.5}$
O^{8+} +H Lyβ	0.7739	$101.8\ ^{+15.0}_{-8.8}$	74.47	67.13
O^{8+} +H Lyγ	0.8163	$18.0\ ^{+7.3}_{-0.7}$	33.99	30.64
O^{8+} +H Lyδ	0.8358	$51.25\ ^{+31.16}_{-15.53}$	68.38	61.64
O^{8+} +H Lyϵ	0.8465	$34.1\ ^{+191.1}_{-34.1}$	11.30	10.19
N^{7+} +H Lyα	0.4999	$214.4\ ^{+17.8}_{-62.2}$	$394.9\ ^{+23.2}_{-26.7}$	$420.6\ ^{+31.8}_{-21.1}$
N^{7+} +H Lyβ	0.5926	$131.2\ ^{+41.6}_{-30.0}$	40.63	43.28
N^{7+} +H Lyγ	0.625	$101.5\ ^{+17.1}_{-25.5}$	24.10	25.68
N^{7+} +H Lyδ	0.6399	$97.5\ ^{+19.5}_{-23.5}$	77.23	82.27
N^{7+} +H Lyϵ	0.6481	$75.0\ ^{+63.1}_{-5.2}$	3.8×10^{-5}	1.0×10^{-3}
Ne IX Kα	0.91	$257.8\ ^{+12.3}_{-11.5}$	$247.2\ ^{+6.5}_{-6.8}$	$251.5\ ^{+6.9}_{-6.5}$

Continued on Next Page...

Table A.1 – Continued

Line	Energy (keV)	CX-Inspired (Fig 3.4) (L.U.)	CX (Fig 3.3) (L.U.)	CX with Fe (Fig 3.5) (L.U.)
(1)	(2)	(3)	(4)	(5)
Ne X Lyα	1.022	$14.78\ ^{+1.98}_{-2.68}$	$15.66\ ^{+2.07}_{-2.43}$	$15.27\ ^{+2.21}_{-2.26}$
Fe L($3d \rightarrow 2p$)	0.726	...	...	$234.8\ ^{+12.6}_{-10.6}$
Fe L($3s \rightarrow 2p$)	0.822	...	...	$2.2\times10^{-15}\ ^{+1.88}_{-0.00}$
Ne Kβ	1.074	$11.47\ ^{+2.45}_{-2.33}$	$11.39\ ^{+1.94}_{-2.04}$	$11.39\ ^{+1.5}_{-2.7}$
Ne Kγ	1.127	$11.00\ ^{+1.72}_{-1.71}$	$11.32\ ^{+1.62}_{-1.56}$	$11.46\ ^{+1.11}_{-2.26}$
Ne Lyβ	1.21	$3.346\ ^{+0.915}_{-1.079}$	$3.750\ ^{+0.856}_{-1.153}$	$3.658\ ^{+0.994}_{-0.995}$
Mg Kα	1.343	$7.321\ ^{+1.225}_{-0.769}$	$6.849\ ^{+1.118}_{-0.843}$	$7.674\ ^{+1.016}_{-0.928}$
Mg Kβ	1.571	$0.723\ ^{+0.553}_{-0.496}$	$0.807\ ^{+0.482}_{-0.487}$	$0.985\ ^{+0.492}_{-0.479}$
Si Kα	1.833	$1.138\ ^{+0.471}_{-0.366}$	$1.182\ ^{+0.244}_{-0.494}$	$1.180\ ^{+0.353}_{-0.341}$
Reduced χ^2	...	1.36 with 533 d.o.f.	3.95 with 555 d.o.f.	1.83 with 553 d.o.f.

Line normalizations for Figures 3.4–3.5. L.U. (line unit) = photons $cm^{-2}s^{-1}sr^{-1}$. The line energies are fixed, and the lines have zero intrinsic width. In columns 4 and 5, the Kβ and higher lines for C, N, and O are tied to their respective Kα resonant lines (see §3.2.2 for details).

Table A.2: Charge Exchange X-ray Emission with H Targets

Line	Photon Energy (eV)	200 eV/u (195.7 km/s)	300 eV/u (239.7 km/s)	500 eV/u (309.4 km/s)	700 eV/u (366.1 km/s)	1000 eV/u (437.5 km/s)	2000 eV/u (618.8 km/s)	3000 eV/u (757.8 km/s)	5000 eV/u (978.4 km/s)
C V K α f	298.96	5.7749	4.9702	3.8222	3.4371	3.5342	3.0855	2.9421	3.3264
C V K α i	304.41	0.5253	0.4653	0.3662	0.3042	0.2980	0.2720	0.2859	0.3228
C V K α r	307.90	1.0000	1.0000	1.0000	1.0000	1.0000	1.0000	1.0000	1.0000
C V K β	354.52	0.4950	0.4554	0.3948	0.3412	0.3282	0.2577	0.2279	0.2553
C V K γ	370.92	0.0704	0.0537	0.0377	0.0481	0.0574	0.0445	0.0299	0.0378
C V K δ	378.53	0.0000	0.0000	0.0000	0.0000	0.0000	0.0000	0.0099	0.0047
C VI Ly α	367.49	1.0000	1.0000	1.0000	1.0000	1.0000	1.0000	1.0000	1.0000
C VI Ly β	435.55	0.1229	0.1262	0.1359	0.1425	0.1478	0.1503	0.1467	0.1377
C VI Ly γ	459.37	0.1525	0.1636	0.1886	0.2083	0.2286	0.2485	0.2367	0.1947
C VI Ly δ	470.39	0.0283	0.0217	0.0172	0.0154	0.0140	0.0125	0.0119	0.0113
C VI Ly ϵ	476.38	0.0006	0.0007	0.0008	0.0010	0.0012	0.0019	0.0023	0.0031
N VI K α f	419.80	5.2080	4.7471	3.9598	3.5720	3.1960	3.0085	2.6322	2.4636
N VI K α i	426.32	0.9454	0.9603	1.0005	1.0103	0.9958	1.0697	0.9750	0.9599
N VI K α r	430.70	1.0000	1.0000	1.0000	1.0000	1.0000	1.0000	1.0000	1.0000
N VI K β	497.97	0.1765	0.1822	0.1982	0.1962	0.1719	0.1480	0.1320	0.1138
N VI K γ	521.58	0.1384	0.1362	0.1258	0.1116	0.0931	0.0755	0.0649	0.0595
N VI K δ	532.65	0.0012	0.0033	0.0062	0.0068	0.0101	0.0148	0.0147	0.0156
N VI K ϵ	0.0000	0.0000	0.0000	0.0000	0.0000	0.0000	0.0000	0.0036	0.0021

Continued on Next Page...

Line	Photon Energy (eV)	200 eV/u (195.7 km/s)	300 eV/u (239.7 km/s)	500 eV/u (309.4 km/s)	700 eV/u (366.1 km/s)	1000 eV/u (437.5 km/s)	2000 eV/u (618.8 km/s)	3000 eV/u (757.8 km/s)	5000 eV/u (978.4 km/s)
N VII Ly α	500.28	1.0000	1.0000	1.0000	1.0000	1.0000	1.0000	1.0000	1.0000
N VII Ly β	592.93	0.1214	0.3299	0.3364	0.3405	0.3453	0.0959	0.101	0.08631
N VII Ly γ	625.35	0.0463	0.4293	0.5137	0.5635	0.6163	0.0897	0.1535	0.0905
N VII Ly δ	640.36	0.2538	0.5181	0.4324	0.3814	0.3265	0.1582	0.1852	0.1061
N VII Ly ϵ	648.52	0.0115	0.0000	0.0000	0.0000	0.0000	0.0053	0.0044	0.0039
O VII K α f	560.99	1.9706	1.7984	1.4971	1.2824	1.0928	1.1238	1.3057	1.3870
O VII K α i	568.59	1.2546	1.1645	1.0649	0.9901	0.9547	1.1497	1.3646	1.6384
O VII K α r	573.95	1.0000	1.0000	1.0000	1.0000	1.0000	1.0000	1.0000	1.0000
O VII K β	665.62	0.1784	0.1733	0.1519	0.1390	0.1278	0.1133	0.1178	0.1100
O VII K γ	697.80	0.0794	0.0784	0.0662	0.0573	0.0461	0.0545	0.0762	0.0885
O VII K δ	712.72	0.0209	0.0191	0.0231	0.0217	0.0161	0.0295	0.0366	0.0339
O VII K ϵ	720.84	0.0116	0.0079	0.0083	0.0079	0.0077	0.0101	0.0103	0.0052
O VIII Ly α	653.56	1.0000	1.0000	1.0000	1.0000	1.0000	1.0000	1.0000	1.0000
O VIII Ly β	774.59	0.1281	0.1271	0.1251	0.1235	0.1212	0.1147	0.1089	0.0997
O VIII Ly γ	816.95	0.0742	0.0668	0.0605	0.0577	0.0553	0.0510	0.0480	0.0437
O VIII Ly δ	836.55	0.1160	0.1155	0.1140	0.1129	0.1113	0.1040	0.0957	0.0802
O VIII Ly ϵ	847.20	0.0478	0.0357	0.0260	0.0217	0.0184	0.0139	0.0120	0.0102
Ne IX K α f	905.08	2.0764	2.0252	1.9992	2.0105	2.0487	2.1945	2.3036	2.4454
Ne IX K α i	914.93	3.3194	3.3053	3.2960	3.2986	3.3061	3.3400	3.3644	3.3946
Ne IX K α r	922.02	1.0000	1.0000	1.0000	1.0000	1.0000	1.0000	1.0000	1.0000

Continued on Next Page...

Line	Photon Energy (eV)	200 eV/u (195.7 km/s)	300 eV/u (239.7 km/s)	500 eV/u (309.4 km/s)	700 eV/u (366.1 km/s)	1000 eV/u (437.5 km/s)	2000 eV/u (618.8 km/s)	3000 eV/u (757.8 km/s)	5000 eV/u (978.4 km/s)
Ne IX K β	1073.77	0.2227	0.2238	0.2284	0.2329	0.2395	0.2556	0.2655	0.2774
Ne IX K γ	1127.10	0.1004	0.0994	0.1005	0.1024	0.1057	0.1147	0.1214	0.1320
Ne IX K δ	1151.82	0.0663	0.0726	0.0920	0.1115	0.1421	0.2237	0.2764	0.3396
Ne IX K ϵ	1164.99	0.3739	0.3469	0.3136	0.2942	0.2721	0.2295	0.2062	0.1785
Ne IX K ζ	1173.54	0.0002	0.0001	0.0001	0.0001	0.0001	0.0001	0.0001	0.0001
Ne X Ly α	1021.65	1.0000	1.0000	1.0000	1.0000	1.0000	1.0000	1.0000	1.0000
Ne X Ly β	1210.84	0.1629	0.1367	0.1157	0.2774	0.0912	0.0766	0.0803	0.0685
Ne X Ly γ	1277.06	0.0601	0.0480	0.0385	0.1305	0.0287	0.0207	0.0224	0.0185
Ne X Ly δ	1307.71	0.0849	0.0754	0.0629	0.1887	0.0433	0.0192	0.0279	0.0246
Ne X Ly ϵ	1324.36	0.1874	0.1312	0.0937	0.5184	0.0678	0.0501	0.0494	0.0320
Ne X Ly ζ	1334.40	0.0015	0.0020	0.0036	0.0333	0.0021	0.0056	0.0056	0.0047
Mg XI K α f	1331.12	3.1226	3.1703	3.1896	3.1825	3.1648	3.1253	3.1081	3.0945
Mg XI K α i	1343.34	6.5979	6.6308	6.5120	6.3726	6.1751	5.7830	5.5955	5.4096
Mg XI K α r	1352.25	1.0000	1.0000	1.0000	1.0000	1.0000	1.0000	1.0000	1.0000
Mg XI K β	1579.32	0.3427	0.3456	0.3483	0.3489	0.3488	0.3461	0.3436	0.3406
Mg XI K γ	1659.07	0.1687	0.1714	0.1737	0.1743	0.1742	0.1721	0.1708	0.1706
Mg XI K δ	1696.03	0.1020	0.1047	0.1090	0.1131	0.1207	0.1499	0.1757	0.2152
Mg XI K ϵ	1716.12	0.3684	0.4571	0.5519	0.5945	0.6290	0.6548	0.6497	0.6293
Mg XI K ζ	1728.24	0.5903	0.5414	0.4699	0.4251	0.3740	0.2846	0.2427	0.1998
Mg XI K η	1736.11	0.0056	0.0051	0.0041	0.0036	0.0030	0.0022	0.0018	0.0015

Continued on Next Page. . .

Line	Photon Energy (eV)	200 eV/u (195.7 km/s)	300 eV/u (239.7 km/s)	500 eV/u (309.4 km/s)	700 eV/u (366.1 km/s)	1000 eV/u (437.5 km/s)	2000 eV/u (618.8 km/s)	3000 eV/u (757.8 km/s)	5000 eV/u (978.4 km/s)
Mg XII Ly α	1472.00	1.0000	1.0000	1.0000	1.0000	1.0000	1.0000	1.0000	1.0000
Mg XII Ly β	1744.59	0.2484	0.2498	0.2517	0.2528	0.0685	0.0701	0.0711	0.0725
Mg XII Ly γ	1839.99	0.1093	0.1104	0.1117	0.1125	0.0197	0.0204	0.0209	0.0216
Mg XII Ly δ	1884.15	0.0627	0.0636	0.0653	0.0670	0.0100	0.0120	0.0137	0.0165
Mg XII Ly ϵ	1908.14	0.1087	0.1331	0.1666	0.1874	0.0265	0.0317	0.0341	0.0365
Mg XII Ly ζ	1922.61	0.4108	0.4032	0.3854	0.3721	0.0367	0.0329	0.0307	0.0279
Mg XII Ly η	1931.99	0.0724	0.0597	0.0484	0.0429	0.0032	0.0025	0.0022	0.0018
Al XII K α f	1574.99	2.7350	2.7586	2.8015	2.8366	2.8750	2.9383	2.9598	2.9759
Al XII K α i	1588.47	5.9603	5.8129	5.7155	5.6808	5.6399	5.5300	5.4367	5.3045
Al XII K α r	1598.30	1.0000	1.0000	1.0000	1.0000	1.0000	1.0000	1.0000	1.0000
Al XII K β	1868.72	0.3400	0.3390	0.3388	0.3392	0.3397	0.3407	0.3406	0.3398
Al XII K γ	1963.68	0.1662	0.1653	0.1651	0.1654	0.1659	0.1667	0.1669	0.1670
Al XII K δ	2007.68	0.0991	0.0984	0.0985	0.0991	0.1005	0.1089	0.1188	0.1380
Al XII K ϵ	2031.60	0.1096	0.1390	0.1900	0.2265	0.2715	0.3574	0.3964	0.4309
Al XII K ζ	2046.02	0.7397	0.7071	0.6647	0.6381	0.6043	0.5298	0.4842	0.4278
Al XII K η	2055.39	0.1147	0.0957	0.0780	0.0701	0.0611	0.0460	0.0395	0.0323
Al XIII Ly α	1728.10	1.0000	1.0000	1.0000	1.0000	1.0000	1.0000	1.0000	1.0000
Al XIII Ly β	2048.12	0.2384	0.2399	0.2419	0.2431	0.0630	0.0646	0.0656	0.0669
Al XIII Ly γ	2160.13	0.1024	0.1035	0.1049	0.1057	0.0176	0.0183	0.0187	0.0193
Al XIII Ly δ	2211.97	0.0578	0.0586	0.0596	0.0603	0.0083	0.0091	0.0099	0.0113
Al XIII Ly ϵ	2240.13	0.0470	0.0556	0.0714	0.0835	0.0124	0.0169	0.0195	0.0226
Al XIII Ly ζ	2257.11	0.2528	0.2798	0.3034	0.3122	0.0332	0.0332	0.0327	0.0316

Continued on Next Page...

Line	Photon Energy (eV)	200 eV/u (195.7 km/s)	300 eV/u (239.7 km/s)	500 eV/u (309.4 km/s)	700 eV/u (366.1 km/s)	1000 eV/u (437.5 km/s)	2000 eV/u (618.8 km/s)	3000 eV/u (757.8 km/s)	5000 eV/u (978.4 km/s)
Al XIII Ly η	2268.13	0.2508	0.2215	0.1899	0.1733	0.0137	0.0111	0.0098	0.0084
Al XIII Ly θ	2275.69	0.0087	0.0075	0.0059	0.0052	0.0003	0.0003	0.0002	0.0002
Si XIII K α f	1839.43	1.3883	1.4528	1.5505	1.6168	1.6980	1.8573	1.9395	2.0287
Si XIII K α i	1854.23	3.8306	3.9074	4.0372	4.1316	4.2531	4.4951	4.6174	4.7366
Si XIII K α r	1864.99	1.0000	1.0000	1.0000	1.0000	1.0000	1.0000	1.0000	1.0000
Si XIII K β	2182.56	0.2258	0.2345	0.2457	0.2522	0.2591	0.2703	0.2751	0.2801
Si XIII K γ	2294.06	0.0918	0.0968	0.1034	0.1073	0.1115	0.1187	0.1220	0.1259
Si XIII K δ	2345.72	0.0494	0.0525	0.0566	0.0592	0.0621	0.0684	0.0734	0.0832
Si XIII K ϵ	2373.80	0.0327	0.0380	0.0503	0.0619	0.0803	0.1316	0.1665	0.2103
Si XIII K ζ	2390.73	0.0853	0.1191	0.1684	0.1994	0.2344	0.2927	0.3156	0.3319
Si XIII K η	2401.71	0.2272	0.2151	0.1992	0.1895	0.1779	0.1542	0.1407	0.1239
Si XIII K θ	2409.26	0.0084	0.0073	0.0064	0.0062	0.0052	0.0042	0.0037	0.0032

Continued on Next Page. . .

Line	Photon Energy (eV)	200 eV/u (195.7 km/s)	300 eV/u (239.7 km/s)	500 eV/u (309.4 km/s)	700 eV/u (366.1 km/s)	1000 eV/u (437.5 km/s)	2000 eV/u (618.8 km/s)	3000 eV/u (757.8 km/s)	5000 eV/u (978.4 km/s)
Si XIV Ly α	2004.88	1.0000	1.0000	1.0000	1.0000	1.0000	1.0000	1.0000	1.0000
Si XIV Ly β	2376.15	0.2310	0.2323	0.2340	0.2350	0.0583	0.0598	0.0608	0.0620
Si XIV Ly γ	2506.10	0.0975	0.0984	0.0995	0.1002	0.0159	0.0165	0.0169	0.0174
Si XIV Ly δ	2566.25	0.0544	0.0550	0.0558	0.0563	0.0074	0.0078	0.0082	0.0089
Si XIV Ly ϵ	2598.92	0.0360	0.0377	0.0418	0.0460	0.0063	0.0088	0.0107	0.0133
Si XIV Ly ζ	2618.62	0.1186	0.1440	0.1746	0.1910	0.0219	0.0246	0.0257	0.0264
Si XIV Ly η	2631.40	0.3124	0.3003	0.2811	0.2685	0.0226	0.0199	0.0183	0.0164
Si XIV Ly θ	2640.17	0.0657	0.0556	0.0459	0.0414	0.0028	0.0022	0.0019	0.0016
Si XIV Ly ι	2646.44	0.0007	0.0006	0.0005	0.0004	0.0000	0.0000	0.0000	0.0000

Relative Line intensities are shown for all ions considered in this dissertation colliding with H. For this table, QMOCC cross sections are used when available for C^{5+} + H (Nolte et al., 2012), N^{6+} + H (Wu et al., 2011), and O^{7+} + H (Jeff Nolte, Private communication). AOCC cross-sections are then used for Ne^{10+} + H for energies above 1 keV/u, while CTMC cross-sections are used for energies below 1 keV/u (Cumbee et al., 2016a). For C^{6+} + H and O^{8+} + H, recommended cross-sections from Janev et al. (1993) are used, and for N^{7+} +H (Harel et al., 1998), MOCC cross-sections are used. In all other cases, and when energies are missing for the more accurate methods, below 1 keV/u, MCLZ low-energy ℓ-distribution cross sections are used, and for energies at and above 1 keV/u, MCLZ statistical ℓ-distribution cross-sections are used.

Table A.3: Charge Exchange X-ray Emission with He Targets

Line	Photon Energy (eV)	200 eV/u (195.7 km/s)	300 eV/u (239.7 km/s)	500 eV/u (309.4 km/s)	700 eV/u (366.1 km/s)	1000 eV/u (437.5 km/s)	2000 eV/u (618.8 km/s)	3000 eV/u (757.8 km/s)	5000 eV/u (978.4 km/s)
C V K α f	298.96	2.5890	2.6085	2.6306	2.6434	2.6494	2.6739	2.6723	2.6394
C V K α i	304.41	0.2100	0.2121	0.2145	0.2157	0.2164	0.2187	0.2188	0.2162
C V K α r	307.90	1.0000	1.0000	1.0000	1.0000	1.0000	1.0000	1.0000	1.0000
C V K β	354.52	0.6122	0.6045	0.5967	0.5941	0.5890	0.5841	0.5784	0.5687
C VI Ly α	367.49	1.0000	1.0000	1.0000	1.0000	1.0000	1.0000	1.0000	1.0000
C VI Ly β	435.55	0.8810	0.8802	0.7309	0.8774	0.5699	0.5287	0.5287	0.5447
C VI Ly γ	459.37	0.0000	0.0000	0.0071	0.0000	0.0281	0.0254	0.0254	0.0217
N VI K α f	419.80	0.4309	0.5246	0.6562	0.7416	0.8452	1.0516	1.1593	1.2725
N VI K α i	426.32	0.2259	0.2484	0.2691	0.2791	0.2900	0.3142	0.3298	0.3487
N VI K α r	430.70	1.0000	1.0000	1.0000	1.0000	1.0000	1.0000	1.0000	1.0000
N VI K β	497.97	3.2129	2.9451	2.6674	2.5134	2.3365	1.9840	1.7894	1.5642
N VII Ly α	500.28	1.0000	1.0000	1.0000	1.0000	1.0000	1.0000	1.0000	1.0000
N VII Ly β	592.93	0.4964	0.5405	0.6022	0.6396	0.2974	0.3410	0.3593	0.3754
N VII Ly γ	625.35	0.7058	0.6251	0.5119	0.4432	0.1015	0.0699	0.0559	0.0424
O VII K α f	560.99	2.0313	2.0317	1.9960	1.9591	1.8585	1.5048	1.2546	0.9920

Continued on Next Page...

Line	Photon Energy (eV)	200 eV/u (195.7 km/s)	300 eV/u (239.7 km/s)	500 eV/u (309.4 km/s)	700 eV/u (366.1 km/s)	1000 eV/u (437.5 km/s)	2000 eV/u (618.8 km/s)	3000 eV/u (757.8 km/s)	5000 eV/u (978.4 km/s)
O VII K α i	568.59	1.0309	1.0299	1.0137	1.0001	0.9619	0.8297	0.7344	0.6300
O VII K α r	573.95	1.0000	1.0000	1.0000	1.0000	1.0000	1.0000	1.0000	1.0000
O VII K β	665.62	0.4328	0.4530	0.5176	0.5938	0.7205	1.0512	1.2110	1.3184
O VII K γ	697.80	0.8981	0.8927	0.8703	0.8513	0.8028	0.6277	0.5037	0.3596
O VIII Ly α	653.56	1.0000	1.0000	1.0000	1.0000	1.0000	1.0000	1.0000	1.0000
O VIII Ly β	774.59	0.3830	0.3887	0.3987	0.4066	0.1532	0.1672	0.1770	0.1905
O VIII Ly γ	816.95	0.9135	0.9031	0.8848	0.8703	0.2037	0.1937	0.1866	0.1765
Ne IX K α f	905.08	0.4381	0.3557	0.3005	0.2871	0.2897	0.3446	0.4002	0.4851
Ne IX K α i	914.93	0.4341	0.3642	0.3269	0.3249	0.3390	0.4068	0.4624	0.5402
Ne IX K α r	922.02	1.0000	1.0000	1.0000	1.0000	1.0000	1.0000	1.0000	1.0000
Ne IX K β	1073.77	0.2721	0.2675	0.2649	0.2647	0.2656	0.2712	0.2777	0.2914
Ne IX K γ	1127.10	0.1220	0.1560	0.2206	0.2691	0.3322	0.4637	0.5316	0.5998
Ne IX K δ	1151.82	0.2569	0.2023	0.1567	0.1362	0.1181	0.0908	0.0790	0.0661
Ne X Ly α	1021.65	1.0000	1.0000	1.0000	1.0000	1.0000	1.0000	1.0000	1.0000
Ne X Ly β	1210.84	0.3152	0.3174	0.3210	0.3237	0.1082	0.1134	0.1174	0.1237
Ne X Ly γ	1277.06	0.2333	0.2613	0.3057	0.3364	0.0830	0.1005	0.1093	0.1185
Ne X Ly δ	1307.71	0.7163	0.6880	0.6427	0.6109	0.0924	0.0796	0.0725	0.0641
Mg XI K α f	1331.12	0.6964	0.6993	0.7326	0.7640	0.8012	0.8634	0.8869	0.9055

Continued on Next Page...

Line	Photon Energy (eV)	200 eV/u (195.7 km/s)	300 eV/u (239.7 km/s)	500 eV/u (309.4 km/s)	700 eV/u (366.1 km/s)	1000 eV/u (437.5 km/s)	2000 eV/u (618.8 km/s)	3000 eV/u (757.8 km/s)	5000 eV/u (978.4 km/s)
Mg XI K α i	1343.34	1.4012	1.4217	1.4690	1.5065	1.5471	1.6097	1.6292	1.640
Mg XI K α r	1352.25	1.0000	1.0000	1.0000	1.0000	1.0000	1.0000	1.0000	1.0000
Mg XI K β	1579.32	0.3136	0.3206	0.3319	0.3385	0.3453	0.3547	0.3579	0.3617
Mg XI K γ	1659.07	0.1431	0.1518	0.1719	0.1904	0.2195	0.3030	0.3619	0.4385
Mg XI K δ	1696.03	1.7296	1.7114	1.6325	1.5700	1.4879	1.3145	1.2168	1.1007
Mg XI K ϵ	1716.12	0.2470	0.1950	0.1451	0.1233	0.1030	0.0718	0.0596	0.0473
Mg XII Ly α	1472.00	1.0000	1.0000	1.0000	1.0000	1.0000	1.0000	1.0000	1.0000
Mg XII Ly β	1744.59	0.2841	0.2871	0.2910	0.2934	0.0918	0.0949	0.0970	0.1002
Mg XII Ly γ	1839.99	0.1367	0.1411	0.1499	0.1575	0.0348	0.0419	0.0467	0.0530
Mg XII Ly δ	1884.15	0.2915	0.3447	0.4068	0.4380	0.0744	0.0802	0.0817	0.0821
Mg XII Ly ϵ	1908.14	0.4604	0.4096	0.3471	0.3129	0.0344	0.0272	0.0238	0.0203
Mg XII Ly ζ	1922.61	0.0006	0.0005	0.0004	0.0004	0.0000	0.0000	0.0000	0.0000
Al XII K α f	1574.99	1.0163	1.0011	0.9688	0.9475	0.9263	0.9035	0.9027	0.9106
Al XII K α i	1588.47	1.3968	1.4096	1.4161	1.4181	1.4242	1.4516	1.4760	1.5116
Al XII K α r	1598.30	1.0000	1.0000	1.0000	1.0000	1.0000	1.0000	1.0000	1.0000
Al XII K β	1868.72	0.3479	0.3436	0.3393	0.3378	0.3373	0.3403	0.3441	0.3505
Al XII K γ	1963.68	0.1693	0.1659	0.1630	0.1630	0.1663	0.1893	0.2153	0.2605
Al XII K δ	2007.68	0.3919	0.5080	0.6570	0.7385	0.8197	0.9242	0.9489	0.9496
Al XII K ϵ	2031.60	0.7803	0.7304	0.6604	0.6156	0.5630	0.4617	0.4086	0.3486
Al XII K ζ	2046.02	0.0011	0.0010	0.0008	0.0008	0.0007	0.0005	0.0004	0.0004

Continued on Next Page. . .

Line	Photon Energy (eV)	200 eV/u (195.7 km/s)	300 eV/u (239.7 km/s)	500 eV/u (309.4 km/s)	700 eV/u (366.1 km/s)	1000 eV/u (437.5 km/s)	2000 eV/u (618.8 km/s)	3000 eV/u (757.8 km/s)	5000 eV/u (978.4 km/s)
Al XIII Ly α	1728.10	1.0000	1.0000	1.0000	1.0000	1.0000	1.0000	1.0000	1.0000
Al XIII Ly β	2048.12	0.2757	0.2774	0.2798	0.2813	0.0848	0.0872	0.0889	0.0915
Al XIII Ly γ	2160.13	0.1291	0.1307	0.1337	0.1364	0.0278	0.0314	0.0343	0.0386
Al XIII Ly δ	2211.97	0.1552	0.1827	0.2225	0.2475	0.0437	0.0517	0.0553	0.0588
Al XIII Ly ϵ	2240.13	0.5488	0.5302	0.4990	0.4776	0.0561	0.0496	0.0459	0.0416
Al XIII Ly ζ	2257.11	0.0335	0.0275	0.0219	0.0193	0.0017	0.0013	0.0011	0.0010
Si XIII K α f	1839.43	0.6531	0.6874	0.7207	0.7358	0.7482	0.7665	0.7772	0.7932
Si XIII K α i	1854.23	1.5694	1.5989	1.6324	1.6494	1.6651	1.6868	1.6976	1.7098
Si XIII K α r	1864.99	1.0000	1.0000	1.0000	1.0000	1.0000	1.0000	1.0000	1.0000
Si XIII K β	2182.56	0.2919	0.2954	0.2999	0.3029	0.3062	0.3140	0.3193	0.3267
Si XIII K γ	2294.06	0.1414	0.1450	0.1487	0.1509	0.1535	0.1626	0.1730	0.1942
Si XIII K δ	2345.72	0.1307	0.1735	0.2481	0.3023	0.3707	0.5063	0.5724	0.6350
Si XIII K ϵ	2373.80	1.2257	1.1383	1.0409	0.9875	0.9279	0.8147	0.7532	0.6792
Si XIII K ζ	2390.73	0.0770	0.0631	0.0507	0.0447	0.0387	0.0297	0.0258	0.0216

Continued on Next Page...

Line	Photon Energy (eV)	200 eV/u (195.7 km/s)	300 eV/u (239.7 km/s)	500 eV/u (309.4 km/s)	700 eV/u (366.1 km/s)	1000 eV/u (437.5 km/s)	2000 eV/u (618.8 km/s)	3000 eV/u (757.8 km/s)	5000 eV/u (978.4 km/s)
Si XIV Ly α	2004.88	1.0000	1.0000	1.0000	1.0000	1.0000	1.0000	1.0000	1.0000
Si XIV Ly β	2376.15	0.2646	0.2669	0.2696	0.2713	0.0792	0.0815	0.0830	0.0851
Si XIV Ly γ	2506.10	0.1210	0.1227	0.1250	0.1267	0.0245	0.0266	0.0285	0.0314
Si XIV Ly δ	2566.25	0.0923	0.1070	0.1310	0.1480	0.0265	0.0335	0.0371	0.0412
Si XIV Ly ϵ	2598.92	0.3992	0.4267	0.4436	0.4461	0.0554	0.0532	0.0515	0.0489
Si XIV Ly ζ	2618.62	0.2147	0.1789	0.1447	0.1284	0.0115	0.0089	0.0078	0.0066
Si XIV Ly η	2631.40	0.0005	0.0004	0.0003	0.0003	0.0000	0.0000	0.0000	0.0000

Same as Table A.2, but for collisions with He. AOCC cross-sections are used for C^{6+} + He (Fritsch and Lin, 1991) for most energies, but this table is primarily composed of MCLZ calculations.